

國立交通大學

材料科學與工程學系

博士論文

鎂-2、5、8(wt.%)錫合金經等通道轉角擠型後
其顯微組織暨室溫與高溫機械性質之研究

A Study on Microstructures as well as Room and High

Temperature Mechanical Properties

of Mg-2, 5, 8(wt.%)Sn Alloys

by Equal Channel Angular Extrusion

研究生：蔡浩然

指導教授：朝春光博士

劉增豐博士

中華民國一〇三年一月

鎂-2、5、8(wt.%)錫合金經等通道轉角擠型後
其顯微組織暨室溫與高溫機械性質之研究

**A Study on Microstructures as well as Room and High Temperature Mechanical Properties
of Mg-2, 5, 8(wt. %)Sn Alloys by Equal Channel Angular Extrusion**

研究生：蔡浩然

Student : Hao-Jan Tsai


指導教授：朝春光 博士

Advisor : Dr. Chuen-Guang Chao

劉增豐 博士

Dr. Tzeng-Feng Liu

國立交通大學
材料科學與工程學系
博士論文



A Thesis
Submitted to Department of Materials Science and Engineering
College of Engineering
National Chiao Tung University
in partial Fulfillment of the Requirements
for the Degree of
Doctor of Philosophy
in
Materials Science and Engineering

January 2014

Hsinchu, Taiwan, Republic of China

中華民國一〇三年一月

鎂-2、5、8(wt.%)錫合金經等通道轉角擠型後

其顯微組織暨室溫與高溫機械性質之研究

研究生：蔡浩然

指導教授：朝春光 博士

劉增豐 博士

國立交通大學

材料科學與工程學系

摘 要

本研究旨在探討 Mg-2、5、8(wt.%)Sn 合金，透過等通道轉角擠型(ECAE)後，其顯微組織與高溫機械性質的變化。實驗結果顯示，隨錫含量的增加，合金中 Mg₂Sn 相的量亦隨之增加，且可在 as-cast Mg-5(wt.%)Sn 及 Mg-8(wt.%)Sn 合金的晶界上發現高連續性的 α -Mg + Mg₂Sn 共晶相。除該共晶相外，極細小的 Mg₂Sn 顆粒亦可在三種合金的基地中同時發現。經 ECAE 四道次擠製後，合金晶粒細化的效果非常明顯，以 Mg-5(wt.%)Sn 合金為例，其平均粒徑可由鑄態之 147 μ m 細化至 28 μ m 且高連續性的 α -Mg + Mg₂Sn 共晶相已被 ECAE 所破斷。

高溫拉伸性質以 Mg-5(wt.%)Sn 合金最佳，該合金經 ECAE 四道次擠製後，其高溫(200 °C)抗拉強度可由鑄態的 67 MPa 提升至 179 MPa，而高溫(200 °C)的伸長量亦可由 10.6 % 提升至 18.9 %。

本研究再進一步將常溫及高溫機械性質最佳之 Mg-5(wt.%)Sn 合金施以等徑通道轉角擠型進行六道次擠製並調查該合金之超塑性成型能力。實驗結果顯示，Mg-5(wt.%)Sn 合金經 ECAE 六道次擠製後，其平均粒徑可由鑄態之 147 μ m 加以細化至 10 μ m。而連續性極高之 α -Mg + Mg₂Sn 的析出相更被完全破斷且均勻分佈在鎂基地中。

而 Mg-5(wt. %)Sn 合金於 350 °C 及應變速率 $1 \times 10^{-3} \text{ s}^{-1}$ 的條件下，可獲得 550 % 的巨大變形量，同樣溫度下再將應變速率提升至 $1 \times 10^{-2} \text{ s}^{-1}$ 時，亦可獲得 238 % 的變形量，此亦說明 Mg-5(wt. %)Sn 合金除具有優良的高溫抗拉強度外亦同時具備超塑性的成型能力。

最後，本研究更針對 Mg-5(wt. %)Sn 合金先後進行固溶熱處理及 ECAE 四道次擠製，實驗結果顯示，Mg-5(wt. %)Sn 合金分別經固溶熱處理及 ECAE 製程後，Mg-5(wt. %)Sn 合金其平均粒徑將由鑄態的 147 μm 細化至 16 μm ，晶粒細化的幅度超過未施以固溶熱處理之 Mg-5(wt. %)Sn 合金，而細小的 Mg_2Sn 顆粒更於 EACE 擠型過程中以動態析出的方式均勻的分佈於基地之中。

再就高溫拉伸性質而言，其高溫(200 °C)的抗拉強度則由 67 MPa 進一步提升至 209 MPa，而高溫(200 °C)的伸長量亦由 10.6 % 提升至 22.1 %。顯示合金預先施以固溶熱處理後再進行 ECAE 製程，確實對 Mg-5(wt. %)Sn 合金之高溫拉伸性質有所助益。



**A Study on Microstructures
as well as Room and High Temperature Mechanical Properties
of Mg-2, 5, 8(wt. %)Sn Alloys by Equal Channel Angular Extrusion**

Student : Hao-Jan Tsai

Advisor : Dr. Chuen-Guang Chao

Dr. Tzeng-Feng Liu

**Department of Materials Science and Engineering
National Chiao Tung University**

ABSTRACT

This study focused on the microstructures and mechanical properties of Mg-2, 5, 8(wt. %)Sn alloys at high temperatures after Equal Channel Angular Extrusion (ECAE). The results showed that the Mg₂Sn phase increased gradually with the addition of tin. The grain boundary of the Mg-2, 5, 8(wt. %)Sn alloys was seen to contain continuous eutectic α -Mg + Mg₂Sn precipitates in the Mg-5(wt. %)Sn and Mg-8(wt. %)Sn as-cast alloys. Besides the grain boundary particles, ultra-fine Mg₂Sn particles were observed within the matrix of Mg-2, 5, 8(wt. %)Sn alloys. After ECAE four passes, the effect of grain refining was very obvious. For example, the average grain size of Mg-5(wt. %)Sn alloy could be refined from 147 μ m to 28 μ m after ECAE four passes. The continuous eutectic α -Mg + Mg₂Sn were broken by ECAE four passes. Optimum tensile properties were attained by adding 5(wt. %)Sn. The UTS of as-cast increased from 67 MPa to 179 MPa at 200 °C, as well as the elongation increased from 10.6 % to 18.9 % at 200 °C after ECAE four passes.

The Mg-5(wt. %)Sn alloy was extruded six passes by using ECAE process. The superplastic ability of Mg-5(wt. %)Sn alloy has been investigated. The result showed that average grain size was refined from 147 μm (as-cast) to 10 μm ($N = 6$); the continuous eutectic $\alpha\text{-Mg} + \text{Mg}_2\text{Sn}$ precipitates were broken and distributed more uniformly in the matrix after ECAE six passes. The Mg-5(wt. %)Sn alloy demonstrated that an elongation of 550 % has been obtained at 350 $^{\circ}\text{C}$ with a strain rate of $1 \times 10^{-3} \text{ s}^{-1}$. Further, an elongation of 238 % has been obtained with a high strain rate of $1 \times 10^{-2} \text{ s}^{-1}$ at the same temperature. Those results mean that the Mg-5(wt. %)Sn alloy not only has the best UTS at high temperatures, but also has ability of superplasticity.

Moreover, this study tried to use in succession Solution Heat Treatment (SHT) and ECAE four passes extrusion on the Mg-5(wt. %)Sn alloy. The results exhibited that the average grain size was significantly refined from 147 μm (as-cast) to 16 μm by SHT + ECAE four passes. The degree of grain refinement was larger than that of none SHT process of Mg-5(wt. %)Sn alloy. Furthermore, the fine Mg_2Sn particles were uniformly distributed in the matrix by dynamic precipitation during ECAE process. The UTS of as-cast increased from 67 MPa to 209 MPa at 200 $^{\circ}\text{C}$, as well as the elongation increased from 10.6 % to 22.1 % at 200 $^{\circ}\text{C}$ after SHT + ECAE four passes. Those results showed that SHT + ECAE process was useful to enhance the high temperatures mechanical properties of Mg-5(wt. %)Sn alloy

誌謝併序

夫為學者『博雜更需慎取、厚積只待薄發』，此句話實為本人十年學、碩、博士之路的最佳詮釋與註解。而夫為人者，於親當孝、師當敬、友當謝後，始可為全人，故本誌謝通篇以七言寫成，凡一百四十四句，由為學、敬師、謝友、孝親、自許依序而誌之，如下：

十載為學髮漸蒼，紅袍加身博士郎，
恰似絕谷栽幽蘭，靜待十年溢殊香；
為學數來十寒暑，宿夜匪懈勤攻讀，
宛若古來貧士子，一朝殿試得聖矚。
求學之路非坦途，堪稱波折崎嶇路，
道險阻卻逆流上，猶勝詩經關雎述；
條條求學志向路，求學迢迢奔波路，
箇中若無險難阻，何能凸顯苦學出？
治學之路雖波阻，一路總遇貴人扶，
雖知言謝難盡表，還寄詩語謝長故。
猶記台科大學樓，先謝趙振綱教授，
殷殷關懷生活事，切切叮囑業勤修；
振學如德厚積累，先曉滿心懷慈悲，
網條似繩衡量準，後教明辨大是非。
此述東華淨無垢，再謝王建義教授，
有幸入門為弟子，初把鎂合金屬究；
建教諄諄以勤歸，金屬每每以輕貴，
義播青苗良善種，門生常侍心相隨。
今憶交通風城舊，更謝朝春光教授，
嚴教勤管樹榜樣，身教言教心寬厚；
春風化雨沐風城，風城因雨生機濃，
光靄衍虹映竹跡，竹跡斑斑寓傳承。
再述交通理工優，也謝劉增豐教授，

受教電子顯微鏡，所穫良多終身受；
增福增利為系所，鐵鋁錳碳開先拓，
豐盈系本為學子，育才無數業界多。
須提師大校中幽，此謝郭金國教授，
六年無私實驗助，銘感五內恩無休；
金揚師範大學光，工業教育培人芳，
國考常顯鑄造成，彩絲原來復求桑。
還記學姊初見時，亦謝陳蓉萱博士，
一年共事生活助，提點實驗鉅細事；
蓉姿初綻竹女塘，辦辦揚開竹湖旁，
萱遺工研材化所，方知台積暗香藏。
更喜摯友是同窗，再謝賢弟王浩仰，
一路相伴解紛憂，我倆子夜觥籌傍；
浩流成勢灌神岡，蓄勢而起遠流長，
仰觀北斗總輪轉，便曉人生是無常。
幸與學弟倆相識，復謝林哲毅博士，
六載戮力共研究，碩博一路為人施；
哲人事事無需言，待人往往以遜謙，
毅字時時身先當，球賽每每覆雲翻。
另敘同心照護情，還謝保代為人豐，
天地無情難知意，風雨有時勢洶洶；
國蓄民儲謀先劃，一紙便能濟人糧，
春暖花淑冬已過，百姓有笑見容芳；
慧曉萬民生計難，救苦尋聲善法傳，
枝滿累累功德果，落地便是種福安。
貴人故人皆有助，人人在我心中住，
或難一一敬謝之，惟願福秧栽您處。

回首求學何為珍？父母之情最是珍，
乾為嚴父蔡國榮，坤為慈母呂淑勤；
國慰家眷育兒長，二十八載戍國疆，
榮拜上校顯金門，名揚蔡氏瓊林鄉；
淑事持家法孟母，侍親以恭足堪書，
勤操家務身親力，更造事業康莊路；
再思父母三重恩，生育養育教育恩，
恩恩不單血親故，恩恩更是父母心；
生育之恩光如陽，陽光普照萬物昌，
賜我身魂暨手足，切記此恩身為康；
養育之恩明若月，月懸九幽無星夜，
引我何處是歸途，切記此恩家為港；
教育之恩瀚似海，海納百川和塵埃，
人間世事皆學問，切記此恩謙為方；
謝天謝地謝高堂，予我三恩彌無量，
何以回報父母恩？孝心為經行為綱；
此生盡孝需即時，莫待行孝無所待，
樹欲靜而風不止，子欲養在未及時。
博士學位紙一張，學歷學力需括囊，
學位僅是畢業證，識人莫以位階量；
甲木待發斂鋒芒，午馬駿蹄千里揚，
馬到成功非一蹴，惟願甲午祈豐糧。

最後以此對聯與學弟妹們共勉之，祝您們早日成就碩博之位：

研萬物之理成一家之言；

究天人之學通古今之變。

蔡浩然 博士

癸巳年臘月除夕 於桃園八德

CONTENT

CHINESE ABSTRACT	I
ABSTRACT	III
ACKNOWLEDGE	V
CONTENT	VIII
TABLE LIST	XI
FIGURE LIST	XII
CHAPTER 1 GENERAL INTRODUCTION	1
CHAPTER 2 LITERATURE REVIEW	4
2.1 Advantages of Mg-Sn alloy system	4
2.2 Development status of Mg-Sn alloy systems	7
2.2.1 High temperatures application	7
2.2.2 Plasticity deformation	18
2.2.2.1 Essential factor of Superplasticity	18
2.2.2.2 Grain refining and dynamic recrystallization	19
2.2.2.3 Superplasticity of Mg-Sn based alloys	25
2.3 Equal Channel Angular Extrusion (ECAE)	28
2.3.1 Effect of die angle	30
2.3.2 Effect of extrusion passes	32
2.3.3 Effect of extrusion routes	34
2.3.4 Effect of extrusion speeds	37
2.3.5 Effect of extrusion temperatures	39

CHAPTER 3 EXPERIMENTAL PROCEDURES 42

3.1 Alloy designing of Mg-2, 5, 8(wt. %)Sn alloys	42
3.2 Casting of Mg-2, 5, 8(wt. %)Sn alloys	42
3.3 ECAE Process of Mg-2, 5, 8(wt. %)Sn alloys	42
3.3.1 ECAE die preparation and extrusion	42
3.3.2 Heating and temperature controlling	43
3.4 Mechanical properties test	43
3.4.1 Hardness test	43
3.4.2 Tensile test at room temperature	44
3.4.3 Tensile test at high temperatures	44
3.4.3.1 Test for tensile strength	44
3.4.3.2 Test for Superplasticity	45
3.5 Characteristic analysis	45
3.5.1 X-Ray Diffraction (XRD) analysis	45
3.5.2 Energy Dispersive Spectroscopy (EDS) analysis	46
3.5.3 Optical Microscope (OM) observation	46
3.5.4 Scanning Electron Microscope (SEM) observation	47
3.5.5 Calculation average grain size distribution	47

CHAPTER 4 MECHANICAL PROPERTIES 48

AT ROOM TEMPERATURE

4.1 Motivation	48
4.2 EDS and XRD analysis	48
4.3 Microstructure observation and grain size distribution	50
4.3.1 In as-cast state	50
4.3.2 After ECAE four passes	55
4.4 Vickers hardness test	65
4.5 Tensile test at room temperature	66
4.6 Fracture surface observation	70
4.7 Summary	72

CHAPTER 5 MECHANICAL PROPERTIES 73

AT HIGH TEMPERATURES

5.1 Motivation	73
5.2 Tensile strength at high temperatures	74
5.2.1 YS and UTS	74
5.2.2 Fracture surface observation	78
5.3 Superplastic behavior evaluation	80
5.3.1 Microstructure observation and grain size distribution	80
5.3.2 Deformation at high temperatures	83
5.3.3 Deformation mechanism	86
5.3.4 Fracture surface observation	89
5.4 Summary	91

CHAPTER 6 SHT + ECAE PROCESS ENHANCING 93

MECHANICAL PROPERTIES AT

HIGH TEMPERATURES

6.1 Motivation	93
6.2 Microstructure observation	93
6.2.1 States with SHT	93
6.2.2 Microstructures after ECAE process state	94
6.2.3 Grain size distribution	98
6.3 Tensile test at room and high temperatures	101
6.4 Fracture surface observation	104
6.5 Summary	108

CHAPTER 7 CONCLUSIONS 109

7.1 Microstructures of Mg-Sn alloys	109
7.2 Tensile properties of Mg-Sn alloys	110
7.3 Fracture surface of Mg-Sn alloys	111

CHAPTER 8 FUTURE WORK 112

REFERENCE 113

PUBLICATION LIST 120

TABLE LIST

Table 2-1 The DAS (d_2) of Mg-Sn alloys.	9
Table 2-2 Time to reach maximum hardness.	13
Table 2-3 Tensile properties of Mg-5% Sn, Mg-5% Sn-2% Di and AE42 alloys at various temperatures.	17
Table 2-4 Comparison tensile tests at with different strain rates.	27
Table 2-5 Equivalent shear strain after ECAE a pass with different stagger angle.	30
Table 2-6 The results of ECAP with different passes and temperatures.	41
Table 3-1 The complete experimental conditions for ECAE and tensile tests.	45
Table 4-1 EDS composition analysis table.	49
Table 4-2 Mg ₂ Sn precipitates EDS composition analysis table.	51
Table 4-3 Mg-X(wt. %)Sn Growth Restriction Factor (GRF) table.	54
Table 4-4 Average grain size of Mg-2, 5, 8(wt. %)Sn alloys.	64
Table 4-5 HV hardness test of Mg-2, 5, 8(wt. %)Sn alloys.	65
Table 4-6 Tensile properties of Mg-2, 5, 8(wt. %)Sn alloys after ECAE process.	67
Table 5-1 Tensile properties of Mg-2, 5, 8(wt. %)Sn alloys after ECAE process.	75
Table 5-2 Average grain size of Mg-5(wt. %)Sn alloy before & after tensile test at different temperatures and strain rates.	84
Table 6-1 Average grain size of Mg-5(wt. %)Sn alloy.	98
Table 6-2 Tensile properties of Mg-5(wt. %)Sn alloy after four ECAE passes.	103

FIGURE LIST

Fig. 2-1 Mg - Sn equilibrium phase diagram of binary alloys.	5
Figs. 2-2 Ultra-fine Mg ₂ Sn particles in the α -Mg matrix: (a) OM low magnification and (b) OM high magnification.	6
Figs. 2-3 OM microstructures of the Mg-Sn alloys: (a) Mg-1%Sn, (b) Mg-3%Sn, (c) Mg-5%Sn, (d) Mg-7%Sn and (e) Mg-10%Sn.	8
Fig. 2-4 Relationship between mechanical properties and tin content in Mg-Sn alloys.	9
Fig. 2-5 Mg-xSn-5Al-1Zn alloys volume percentage of precipitates of Mg ₂ Sn and Mg ₁₇ Al ₁₂ .	10
Figs. 2-6 The microstructure of aging-treated Mg-5(wt. %)Sn alloy: (a) OM and (b) TEM bright-field image.	11
Fig. 2-7 Isothermal aging curves at 200 °C for the binary Mg-1.3 Sn alloy.	12
Fig. 2-8 Age hardening response of Mg-Sn-Mn-Si alloy during ageing at 150 °C, 250 °C and 350 °C.	13
Figs. 2-9 The extruded Mg-2.1Sn-0.1Mn alloys (a) Vickers hardness as a function of aging time, (b) creep strain as a function of time and (c) engineering stress-strain curves.	15
Figs. 2-10 Images of TAS831 alloy: (a) SEM and (b) TEM images with SAD pattern.	16
Figs. 2-11 The dynamic recrystallization brief diagram: (a) cycle DRX, (b) continuous DRX, (c) grain growth controlling DRX and (d) Zener-Hollomon parameter map.	24
Figs. 2-12 (a) OM and (b) TEM micrographs of the extruded TZ81 alloy.	25
Fig. 2-13 Variations in elongations as a function of strain rate in the TZ81 alloys.	27
Figs. 2-14 Brief diagram of ECAE: (a) ECAE die cross-sectional and (b) geometry changing map of simple shear.	29
Figs. 2-15 Brief diagram of geometric relation: (a) $\Psi = 0^\circ$, (b) $\Psi = 180^\circ$ and (c) $0^\circ < \Psi < 180^\circ$.	31
Fig. 2-16 Brief diagram of boundary structures types.	33

Figs. 2-17 Brief diagram of different ECAE routes: (a) rotation degree and (b) shear plane direction.	35
Figs. 2-18 Uneven deformation after ECAE: (a) 0.25 mm/s and (b) 25 mm/s.	37
Fig. 2-19 The specimens after EACE process with different speeds.	38
Figs. 4-1 XRD analysis results: (a) Mg-2(wt. %)Sn, (b) Mg-5(wt. %)Sn and (c) Mg-8(wt. %)Sn.	50
Figs. 4-2 OM images of as-cast state: (a) Mg-2(wt. %)Sn, (b) Mg-5(wt. %)Sn and (c) Mg-8(wt. %)Sn.	52
Figs. 4-3 SEM images of as-cast state: (a) Mg-2(wt. %)Sn, (b) Mg-5(wt. %)Sn and (c) Mg-8(wt. %)Sn.	53
Figs. 4-4 OM images of ECAE four passes: (a) Mg-2(wt. %)Sn, (b) Mg-5(wt. %)Sn and (c) Mg-8(wt. %)Sn.	56
Figs. 4-5 Grain size distribution maps: (a) as-cast Mg-2(wt. %)Sn , (b) as-cast Mg-5(wt. %)Sn, (c) as-cast Mg-8(wt. %)Sn, (d) Mg-2(wt. %)Sn N = 4, (e) Mg-5(wt. %)Sn N = 4 and (f) Mg-8(wt. %)Sn N = 4.	59
Figs. 4-6 (a) OM image of Mg-5(wt. %)Sn N = 1, (b) OM image of Mg-5(wt. %)Sn N = 2, (c) grain size distribution map of Mg-5(wt. %)Sn N = 1 and (d) grain size distribution map of Mg-5(wt. %)Sn N = 2.	62
Figs. 4-7 SEM images: (a) Mg-5(wt. %)Sn N = 4 and (b) Mg-8(wt. %)Sn N = 4.	64
Figs. 4-8 Tensile strength with different ECAE passes: (a) Mg-2(wt. %)Sn, (b) Mg-5(wt. %)Sn and (c) Mg-8(wt. %)Sn.	68
Figs. 4-9 Elongations with different ECAE passes: (a) Mg-2(wt. %)Sn, (b) Mg-5(wt. %)Sn and (c) Mg-8(wt. %)Sn.	69
Figs. 4-10 Fracture surface after tensile test with a fixed strain rate $1 \times 10^{-3} \text{ s}^{-1}$: (a) Mg-2(wt. %)Sn, (b) Mg-5(wt. %)Sn and (c) Mg-8(wt. %)Sn.	71
Figs. 5-1 Tensile strength at high temperatures 100 °C and 200 °C with different ECAE passes: (a) Mg-2(wt. %)Sn, (b) Mg-5(wt. %)Sn and (c) Mg-8(wt. %)Sn.	76

Figs. 5-2 Elongations at high temperatures 100 °C and 200 °C with different ECAE passes: (a) Mg-2(wt. %)Sn, (b) Mg-5(wt. %)Sn and (c) Mg-8(wt. %)Sn.	77
Figs. 5-3 Fracture surface of Mg-5(wt. %)Sn alloy after tensile test with a fixed strain rate $1 \times 10^{-3} \text{ s}^{-1}$: (a) test at 100 °C and (b) test at 200 °C.	79
Figs. 5-4 The microstructure of Mg-5(wt. %)Sn alloy after ECAE six passes: (a) OM image and (b) SEM image.	81
Fig. 5-5 Grain size distribution map of Mg-5(wt. %)Sn alloy after ECAE six passes.	82
Figs. 5-6 Tensile results of Mg-5(wt. %)Sn alloy: (a) elongation obtained at different strain rates and temperatures, (b) test specimens at 250 °C, (c) test specimens at 300 °C and (d) test specimens at 350 °C.	85
Figs. 5-7 (a) the m value of different temperatures and (b) flow stress versus different temperatures curves.	88
Figs. 5-8 SEM images of fracture surface after tensile test with strain rate $1 \times 10^{-2} \text{ s}^{-1}$ at different temperatures (a) 250 °C, (b) 300 °C and (c) 350 °C.	90
Fig. 6-1 OM image of Mg-5(wt. %)Sn alloy after SHT at 480 °C for 22 hours.	94
Figs. 6-2 OM images of Mg-5(wt. %)Sn alloy after SHT + ECAE process: (a) N = 1, (b) N = 2 and (c) N = 4.	96
Figs. 6-3 SEM images of Mg-5(wt. %)Sn alloy after SHT + ECAE process: (a) N = 1, (b) N = 2 and (c) N = 4.	97
Figs. 6-4 Grain size distribution maps (a) N = 1 after SHT, (b) N = 2 after SHT and (c) N = 4 after SHT.	100
Figs. 6-5 Fracture surface after tensile test with a constant strain rate $1 \times 10^{-3} \text{ s}^{-1}$ (a) N = 4 after SHT broken at RT, (b) N = 4 after SHT broken at 100 °C, (c) N = 4 after SHT broken at 200 °C and (d) as-cast broken at 200 °C.	107

CHAPTER 1 GENERAL INTRODUCTION

Magnesium, which was the lightest structural metal, had excellent heat dissipation and vibration resistance. It was used in computers, portable information equipment (3C products) and automotive applications [1]. Most conventional magnesium alloys were based on the Mg-Al alloy system (AZ31, AZ91 and AM60); in the recent years, many scholars have studied different issues about Mg-Al alloy system. First of all, the magnesium alloys were hexagonal close packed (HCP) crystal structure [2, 3]; this structure demonstrated limit plasticity behavior at room temperature; thus, some scholars clearly investigated crystal-plasticity of magnesium alloys [4-6]. Secondly, the twins in the magnesium alloys were observed after deformation or annealing; therefore, several studies directly reported the effect of twins in the magnesium alloys [7-12]. Thirdly, because the texture structure was obviously exhibited after different thermo-mechanical process (extruding, rolling or ECAE), there were many research to focus on the evolution of texture during thermo-mechanical process [13-22]. However, the Mg-Al alloy systems exhibited poor strength at high temperatures [23]. Improving the high temperature properties have become a critical issue for possible cast magnesium alloy applications. Because the main β phase ($Mg_{17}Al_{12}$) was unstable at temperatures above 120 °C [24].

Addition of rare earth (RE) and other elements has been attempted to try to improve the high temperature properties, while the RE elements were much expensive [25-27].

The Mg-Sn alloy systems have recently been the focus of attention because the melting point of the Mg_2Sn phase (770 °C) within the matrix of Mg-Sn alloys was much higher than that of the $Mg_{17}Al_{12}$ phase (462 °C) in Mg-Al alloys [28-39]. This phenomenon could significantly improve high temperature properties of magnesium alloys.

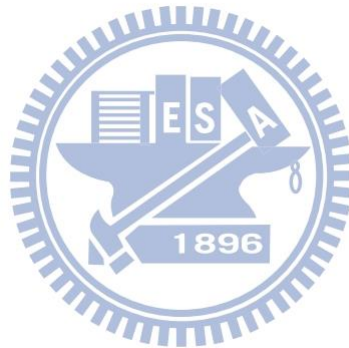
In the present study, the Mg-2, 5, 8(wt. %)Sn alloys were chosen because an earlier study reported that Mg-(1-10)Sn alloys demonstrated good creep resistance at high temperatures [39]. Equal channel angular extrusion (ECAE) [40] was used to improve the room and high temperatures mechanical properties of these alloys. Then this study could discuss the microstructures and mechanical properties from three stages.

In the first stage, this work attempted to enhance the UTS and elongations of these alloys at room temperature; then this work further investigated the relation between microstructures and mechanical properties.

In the second stages, this work intended to investigate the UTS and elongations of these alloys at high temperatures (100 °C and 200 °C); then the potential for

achieving superplastic deformation at high temperatures (250 °C, 300 °C and 350 °C) was evaluated in this stage.

In the third stages, this work could discuss the effect of ECAE on the Solution Heat Treated (SHT) Mg-5(wt. %)Sn alloy; then the relation between microstructures and mechanical properties were studied.



CHAPTER 2 LITERATURE REVIEW

2.1 Advantages of Mg-Sn alloy system

The Mg-Sn alloy system had three main advantages to cause the scholars interesting and studying. [36]

First of all, tin had large solubility in the α -Mg matrix. Fig. 2-1 showed the Mg-Sn binary phase diagram [38]; the tin solubility in the α -Mg was demonstrated from the Mg-Sn binary phase diagram; the amount of tin solubility sharply dropped when the eutectic transformation temperature decreased from 561 °C (14.85 wt. %) to 200 °C (0.45 wt. %). It provided a basis for improving the mechanical properties of Mg-Sn alloy via the Solution Heat Treatment (SHT) and aging treatment.

Secondly, the melting point of the Mg_2Sn phase (770 °C) within the matrix of Mg-Sn alloys was much higher than that of the $Mg_{17}Al_{12}$ phase (462 °C) in Mg-Al alloy systems. This fact could significantly improve the high temperature properties of magnesium alloys. [24]

Thirdly, the Mg_2Sn particles, which existed in the α -Mg matrix, were ultra-fine as shown in Figs. 2-2(a) and (b). It means that these particles could effectively resist the grain boundary sliding at room and high temperatures. [41]

Actually, the Mg-Sn alloy system had more advantages to attract scholars, like inexpensive, easily to obtain and easily to add. [37]

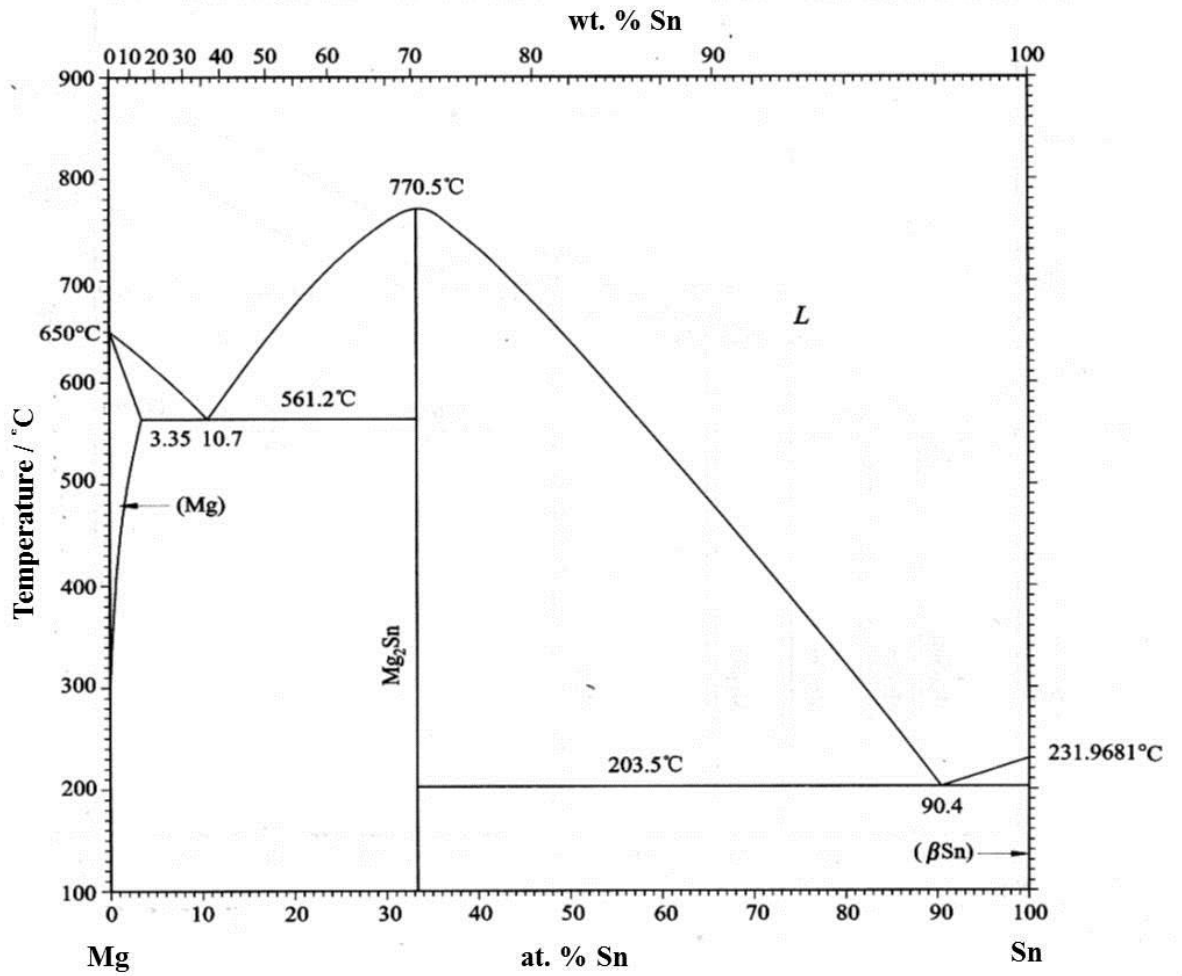
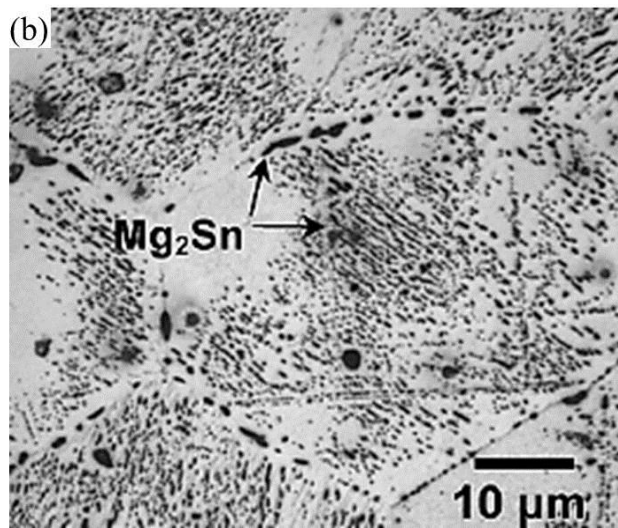
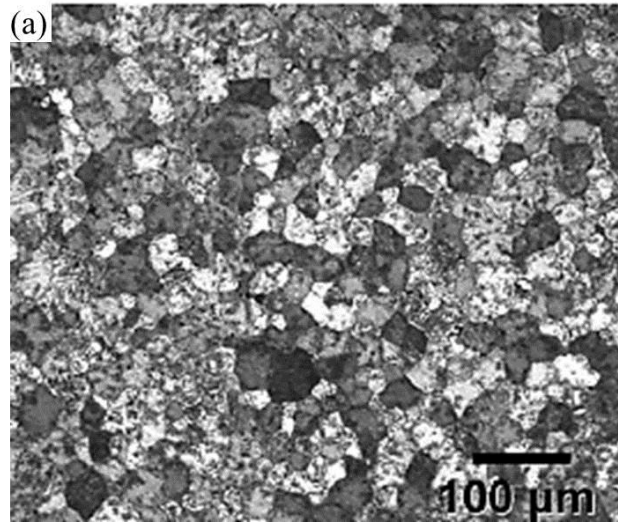


Fig. 2-1 Mg - Sn equilibrium phase diagram of binary alloys [38].



Figs. 2-2 Ultra-fine Mg_2Sn particles in the α -Mg matrix: (a) OM low magnification and (b) OM high magnification [41].

2.2 Development status of Mg-Sn alloy systems

In the recent years, many scholars respectively focused on the different issues of Mg-Sn alloys. High temperature application, plasticity deformation or new Mg-Sn systems development were more common. [42-48]

2.2.1 High temperatures application

Liu et al. have reported the microstructures, tensile properties and creep behavior of as-cast Mg-(1-10 wt. %)Sn alloys [39]; they used the method of Dendrite Arm Spacing (DAS) to calculate the average spacing of second dendrite arm because they considered that the DAS could affect the mechanical properties of as-cast Mg-(1-10 wt. %)Sn alloys.

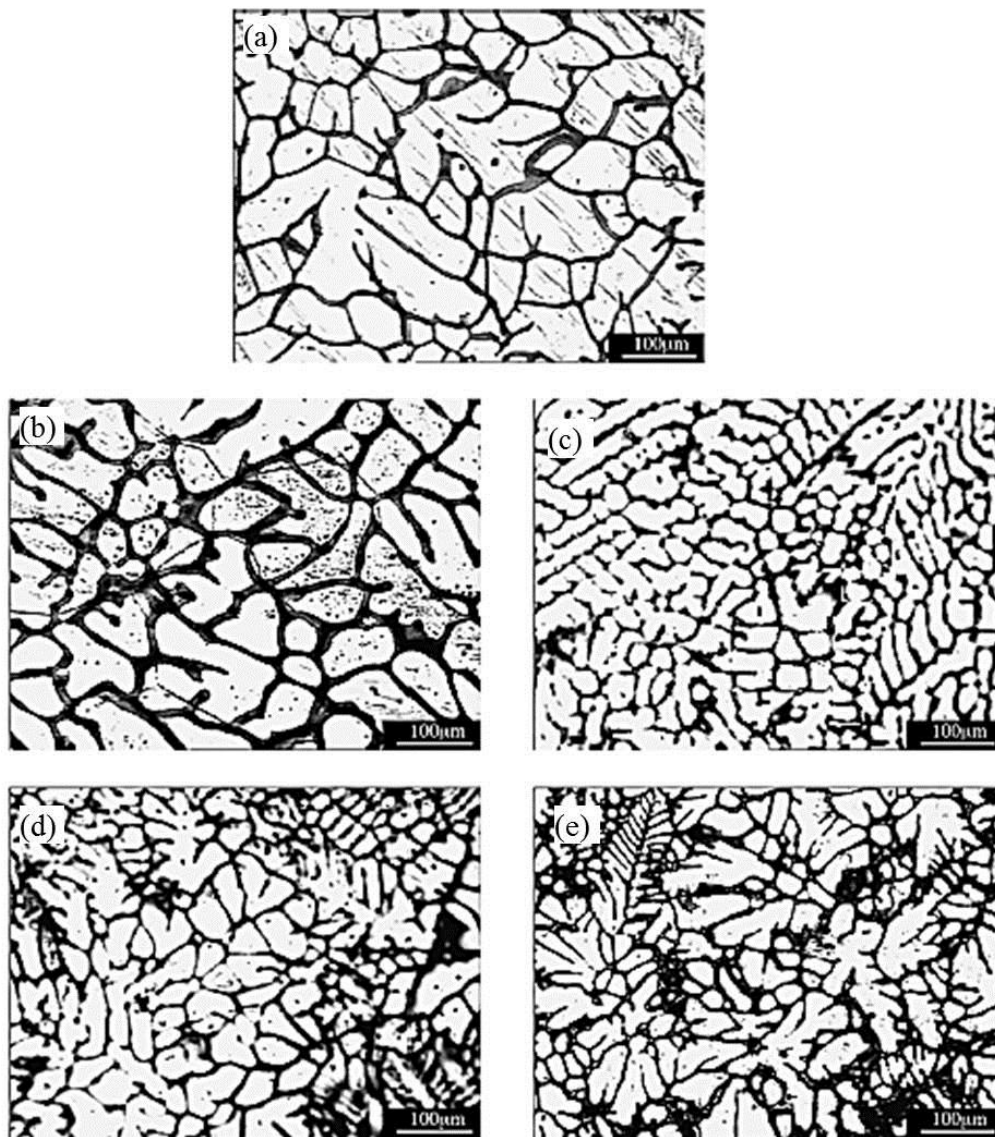
$$d_2 = L_T / PM \quad (2-1)$$

where d_2 was the DAS; M was magnification; L_T was the total length of through measuring line, as well as P was the crossing point between the measuring line and the secondary dendrite.

Figs. 2-3(a)-(e) showed the microstructures of as-cast Mg-(1-10 wt. %)Sn alloys; the eutectic α -Mg + Mg_2Sn layered precipitates increased with increasing tin contents.

Table 2-1 showed the results of DAS; the DAS values similarly increased with increasing tin contents. The authors explained that the tin was partitioned into the liquid ahead of the solidification front; thus, it caused a constitutional super-cooling

zone of liquid ahead of the interface. They also found that the tin induced a refinement effect in Mg–Sn alloys because the constitutional super-cooling caused by the tin enrichment in the liquid ahead of the solid-liquid interface promoted nucleation ,and hindered the fast growth of grain gives rise to dendrites.



Figs. 2-3 OM microstructures of the Mg-Sn alloys: (a) Mg-1%Sn, (b) Mg-3%Sn, (c) Mg-5%Sn, (d) Mg-7%Sn and (e) Mg-10%Sn [39].

Table 2-1 The DAS (d_2) of Mg-Sn alloys [39].

Alloy	The average values of P	$d_2(\mu\text{m})$
Mg-1%Sn	7.2	69.4
Mg-3%Sn	9.6	51.6
Mg-5%Sn	17.3	28.9
Mg-7%Sn	19.1	26.1
Mg-10%Sn	19.6	25.5

Fig. 2-4 exhibited the tensile test at room temperature results of Mg-(1-10 wt. %)Sn alloys; the authors discovered that the Mg-5(wt. %)Sn alloy had the best tensile strength at room temperature.

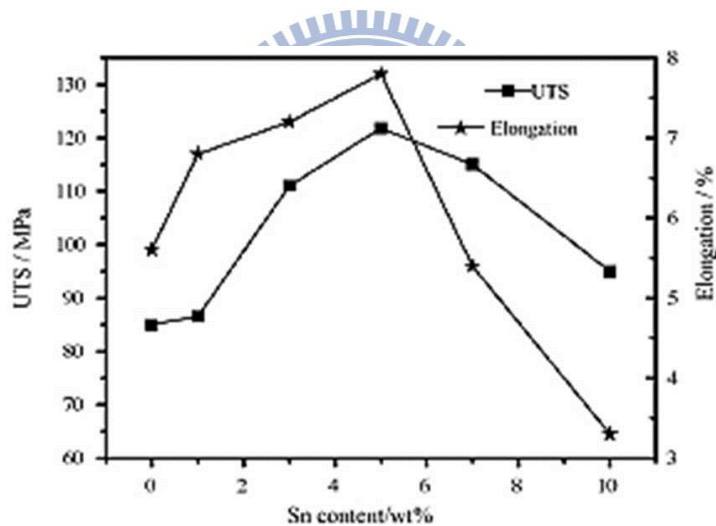


Fig. 2-4 Relationship between mechanical properties and tin content in Mg-Sn alloys [39].

As these results, the authors reported that the average secondary dendrite arm spacing had an effect on the mechanical properties of these alloys [49, 50]; they studied many researches about DAS of aluminium alloys [51- 53]. An empirical relationship existed between DAS and the mechanical properties as follows: [51]

$$Y = A + BX + CX^2 \quad (2-2)$$

where Y was the value of ultimate tensile strength, yield strength or elongation; X was DAS, while A, B (negative value) and C were constants. The enhancement in the tensile strength and the elongation of Mg-Sn alloys transferred from the decreasing of DAS when the tin contents was less than 5 wt. %.

Kim et al. have investigated Mg-xSn-5Al-1Zn alloys, and tin contained 5, 6, 7 and 8 wt. % [54]. They found a similar result with Liu et al. reporting [39]. The tensile strength at room temperature decreased with increasing tin contents as shown in Fig. 2-5.

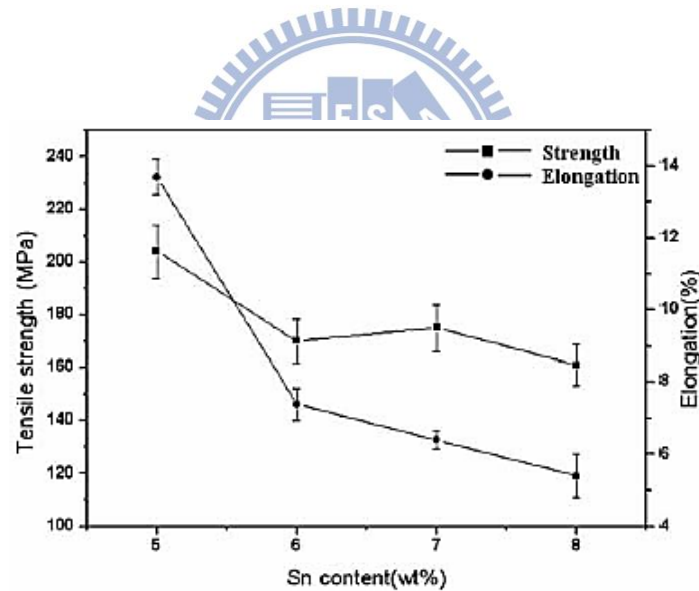
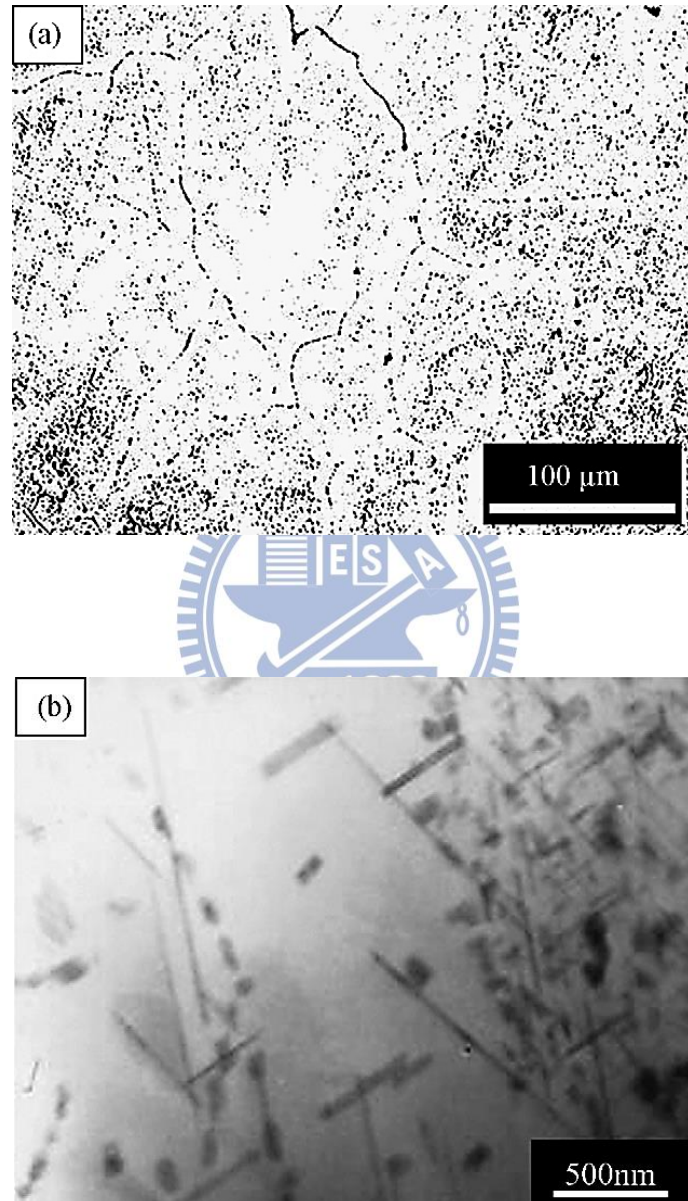


Fig. 2-5 Mg-xSn-5Al-1Zn alloys volume percentage of precipitates of Mg₂Sn and

Mg₁₇Al₁₂ [54].

Wei et al. have further reported the creep behavior of Mg-5(wt. %) Sn alloy by using aging hardening at high temperatures from 150 °C to 200 °C [32]; they successfully improved the compressive creep resistance by uniformly distributing

Mg₂Sn particles as shown in Figs. 2-6(a) and (b); they observed that the discrete Mg₂Sn phase mainly precipitated at grain boundaries, and might restrain the movement of dislocations and grain boundary.



Figs. 2-6 The microstructure of aging-treated Mg-5(wt. %)Sn alloy: (a) OM and (b) TEM bright-field image [32].

Besides Wei et al. research, Mendis et al. have investigated an enhanced age hardening response in Mg–Sn based alloys containing Zn [30]. The authors discovered that the effect of age hardening could be strengthened by adding Zn elements. Fig. 2-7 demonstrated the results of aging heat treatment at 200 °C with different aging times; the result obviously showed that Mg-Sn based alloys, which added Zn, had more high HV hardness. Table 2-2 demonstrated the detail results of HV hardness; it was clear that the aging kinetics of Mg-Sn binary alloys were sluggish at 200 °C; these alloys required in excess over 200 hours to reach peak hardness, and the hardening increment of these alloys was poor (only 10 HV) than that of containing Zn element. These results indicated that the Mg-Sn binary alloys had a potential of enhancing mechanical properties by adding another elements.

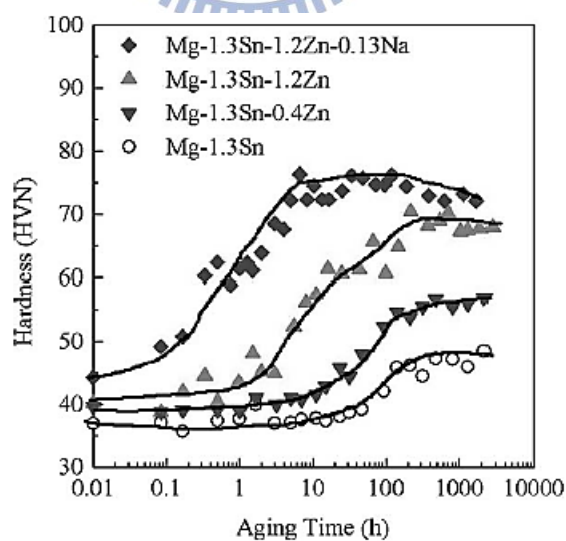


Fig. 2-7 Isothermal aging curves at 200 °C for the binary Mg-1.3 Sn alloy [30].

Table 2-2 Time to reach maximum hardness [30].

Alloy composition (at.%)	Time to reach peak hardness (h)	Maximum hardness (VHN)	Maximum increment in hardness (VHN)
Mg-1.3 Sn	~1000	47	10
Mg-1.3 Sn-0.4 Zn	300	56.8	16.8
Mg-1.3 Sn-1.2 Zn	211	70.1	30
Mg-1.3 Sn-0.12 Na [5]	58	63.2	26.8
Mg-1.3 Sn-1.2 Zn-0.19 Na	6.7	76.4	31.5

Zhang et al. have further studied the crystallography of Mg_2Sn precipitates in Mg-Sn-Mn-Si alloy [55]. The authors investigated the orientation of Mg_2Sn precipitates after aging treatment. They observed that the Mg_2Sn particles had an orientation of $[2-1-10]_{\alpha} // [-110]_{\beta}$. Moreover, the results of aging hardening were shown in Fig. 2-8. The results demonstrated a similar phenomenon with Mendis et al. reporting [30]; The HV hardness could spend much time to reach peak aging (over 200 hours); these results indicated that the adding elements Mn and Si were not helpful to improve the aging hardening of the alloy.

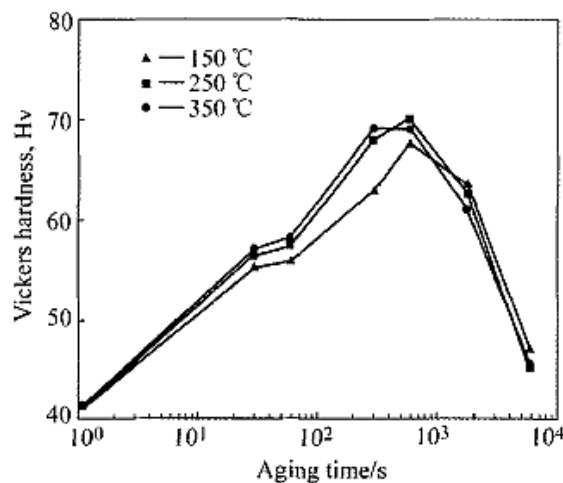
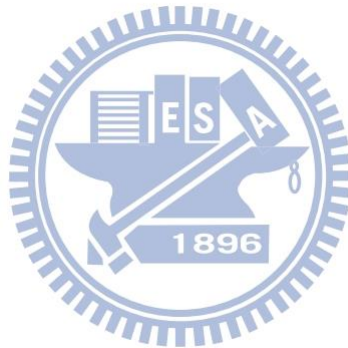


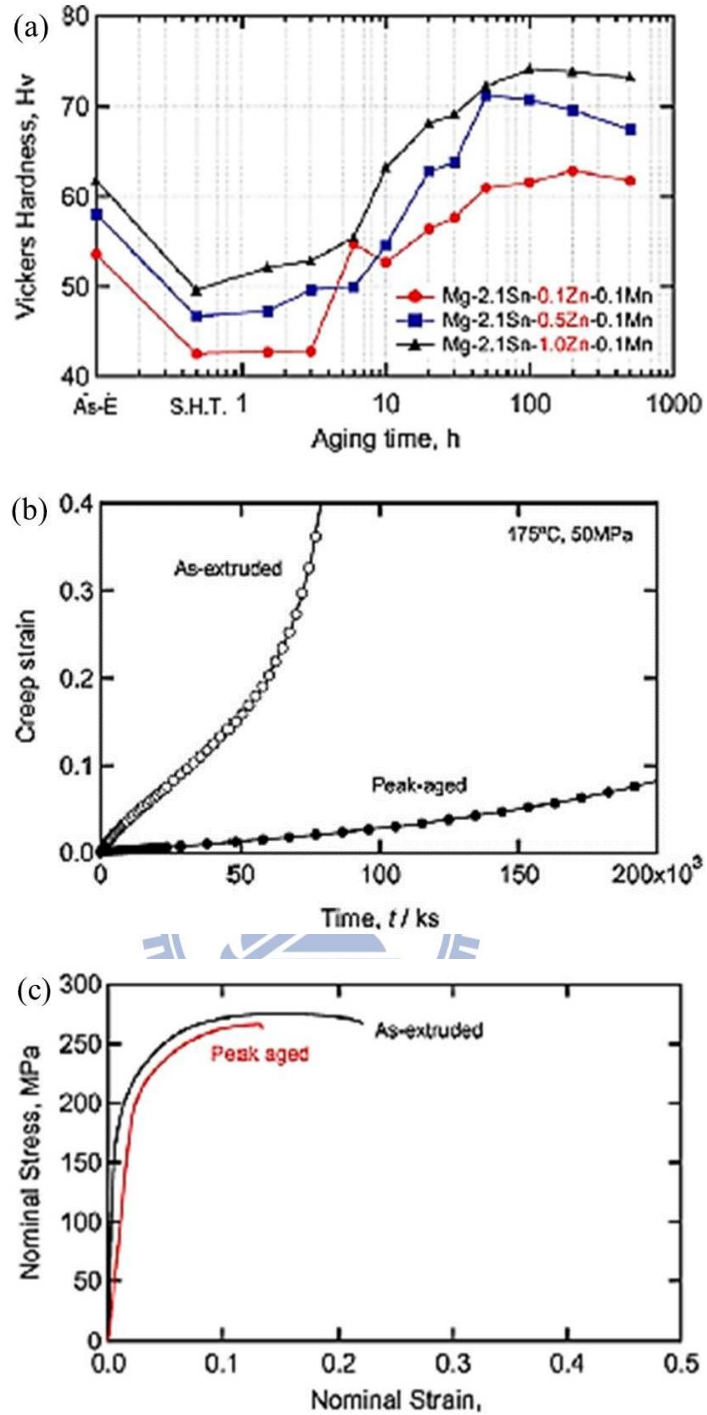
Fig. 2-8 Age hardening response of Mg-Sn-Mn-Si alloy during ageing at

150 °C, 250 °C and 350 °C [55].

However, Sasaki et al. offered a new idea to shorten the time of peak aging [31].

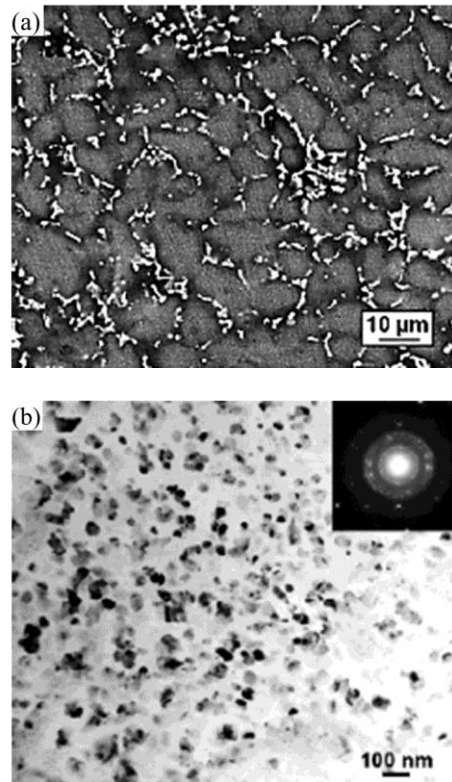
The authors used a wrought Mg-Sn-Zn alloy, which have pre-extruded; then the alloy was treated by SHT + aging treatment. Fig. 2-9(a) demonstrated the results of aging hardening; they discovered that the time to peak aging significantly decreased; further, the creep resistance was obviously promoted by SHT + aging treatment as shown in Fig. 2-9(b). Although the grain growth caused the degradation of the tensile strength as shown in Fig. 2-9(c), the authors believed that the dispersion of fine Mg₂Sn particles within the matrix still played a key role to improve the high temperature mechanical properties.





Figs. 2-9 The extruded Mg-2.1Sn-0.1Mn alloys (a) Vickers hardness as a function of aging time, (b) creep strain as a function of time and (c) engineering stress–strain curves [31].

On the other hand, Kang et al. tried to add Al and Si elements in the Mg-Sn binary alloy (Mg-8Sn-3Al-1Si, TAS831) [29]. The authors focused on a new high temperature precipitates of TAS831 alloy. Figs. 2-10(a) and (b) showed the microstructure of TAS831; they observed that there were three main phases in this alloy (Mg_2Sn particles with small amounts of Mg_2Si and $Mg_{17}Al_{12}$ particles). Especially Mg_2Si particles, these particles were present as globular type; then authors believed that the Mg_2Si particles could further promote the high temperature mechanical properties because the melting point (1102 °C) of Mg_2Si precipitates were much higher than that of Mg_2Sn particles (770 °C).



Figs. 2-10 Images of TAS831 alloy: (a) SEM and (b) TEM images with SAD pattern

[29].

Although the RE was an expensive element, some scholars still attempted to add RE to the Mg-Sn based alloys.

Wei et al., Liu et al. and Pan et al. have respectively investigated the tensile and creep properties of Mg-Sn based alloys by adding La, Di, Sc and Ce elements [48, 56 and 57]. Their reports had similar results as shown in Table 2-3; the creep resistance obviously increased by adding RE elements than that of Mg-Sn binary alloy, but the degree of improvement seemed very close to the commercial AE42 magnesium alloy; the enhancement of tensile strength at room temperature was not very significantly than that of AE42 magnesium alloy. However, the advantages of RE addition have been found at more high temperatures (150 °C and 175 °C); both tensile and creep properties at high temperatures were obviously promoted by RE addition.

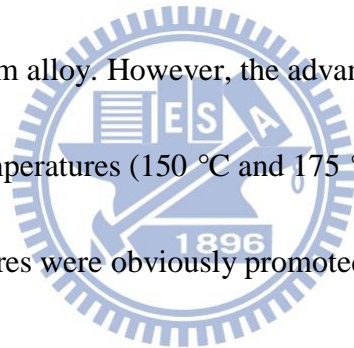


Table 2-3 Tensile properties of Mg-5% Sn, Mg-5% Sn-2% Di and AE42 alloys at various temperatures [56].

Alloys	RT		150°C		175°C		σ_b dropping ratio (%)	
	σ_b (MPa)	δ (%)	σ_b (MPa)	δ (%)	σ_b (MPa)	δ (%)	150°C	175°C
Mg-5% Sn	122	7.8	99	11.5	81	13.6	18.9	33.6
Mg-5% Sn-2% Di	155	8.4	132	17.8	118	19.3	14.8	23.9
AE42	165	10.1	126	21.2	104	23.4	23.6	37.0

Besides high temperature applications and heat treatment of Mg-Sn based alloys, there were a few scholars to contribute in the field of thermo dynamic calculation of Mg-Sn based alloys, like Kozlov et al., Doernberg et al. and Bamberger [43-45, 47]. They respectively focused on the Mg-Sn-Ca, Mg-Sn-Al and Mg-Sn-Zn triple systems; then both they drawn the diagrams of phase equilibrium, while these phase diagrams were very useful for feature research of Mg-Sn fields.

2.2.2 Plasticity deformation

From above 2.2.1, many authors focused on the domain of tensile strength or creep resistance at high temperatures of Mg-Sn based alloys; the researches of plasticity deformation seemed much fewer. Park et al. indicated that controlling the microstructure via heat treatment prior to wrought processing was difficult in Mg-Sn based alloys because these alloys had the thermally stable characteristics of the Mg₂Sn phase [35, 41].

2.2.2.1 Essential factor of superplasticity

Superplasticity was an important index to evaluate the ability of magnesium alloy deformation. In the recent years, scholars focused on the two directions to study the superplasticity.

First of all, high speed deformation, it means that the strain rates of magnesium alloy forming were above $1 \times 10^{-2} \text{ s}^{-1}$.

Secondly, low temperature deformation, it means that the temperatures of magnesium alloy forming were below 100 °C.

However, both high speed deformation and low temperature deformation had a common essential factor; these magnesium alloys must existed a fine grain structure (the average grain size < 20-15 μm), and it could anti grain growth during heat treatment or mechanical properties test at high temperatures.

2.2.2.2 Grain refining and dynamic recrystallization

There were three major methods of grain refining in the magnesium alloys.

First of all, alloying, the grains of magnesium alloy were refined by adding Zr element; then this element produced heterogeneous nucleation with Mg element during melting. The ultra-fine grain structure could directly obtain when alloy cooled after casting in mould.

Secondly, static recrystallization, the grains of magnesium alloys were refined at high temperatures by using annealing treatment, while the fine grains were nucleated at pre-existing grain boundary, twins or dislocations.

Thirdly, dynamic recrystallization (DRX), the grains of magnesium alloys were refined at high temperatures by using thermo-mechanical treatment, like rolling, extruding and ECAE. This part in the present work was a main mechanism of grain refining.

Sakai et al. have detail investigated the DRX in their early report [58]. The authors reported that the procedure of DRX was very similar with static recrystallization, while this procedure needed grain nucleation and grain growth. Because the strain energy was continuously accumulation during thermo-mechanical treatment, the strain energy must be released by DRX. Then the ultra-fine grains were nucleated at pre-existing grain boundary, twins or dislocations, like static recrystallization. The dynamic recrystallization could make density of dislocations numerous decreasing; then magnesium alloy produced soft- phenomenon in local area. According to the grain nucleation and growth, Sakai et al. further reported that there were two kinds of DRX; one was the cycle recrystallization, while another one was continuous recrystallization. When energy of grain nucleation (ϵ_c) was higher than energy of grain growth (ϵ_x), the cycle recrystallization was defined; moreover, the continuous recrystallization means that the grain nucleation and growth was a discontinue process.

In the cycle recrystallization, the DRX started grain nucleation and growth when strain energy satisfied the grain nucleation; then the density of dislocations could obviously decrease during DRX; however, the density of dislocations restarted increasing when grain grew finish; then the working hardening phenomenon could be observed in this stage. Because the cycle recrystallization continuous produced, the

phenomenon of working hardening and softening could be found in the stress-strain curve as shown in Fig. 2-11(a).

By contrast, when energy of grain nucleation (ϵ_c) was lower than energy of grain growth (ϵ_x), the continuous recrystallization could be defined; it means that the DRX started grain nucleation and growth during process of strain energy accumulation when strain energy satisfied the energy of grain nucleation. However, the strain energy has satisfied the energy of grain nucleation in next time before grain growth finishing; this procedure made that the DRX was grain nucleation again. Then this phenomenon could create a stable state between working hardening and softening as shown in stress-strain curve Fig. 2-11(b).

On the other hand, the DRX mechanisms were respectively controlled by grain nucleation and grain growth. The initial grain size was a key factor to decide what mechanism could dominant the process of DRX.

If the initial grain size was coarser, the DRX was easily nucleation at fewer sites; then the strain energy gap between initial grains and DRX grains were decreasing. At the same time, the strain energy of working hardening could simultaneously affect on the initial grains and DRX grains. Therefore, less strain energy gap was so decreasing the driving force of dynamic recrystallization, that the DRX quickly reached a stable

grain size. This phenomenon was the grain growth controlling as shown in Fig.

2-11(c).

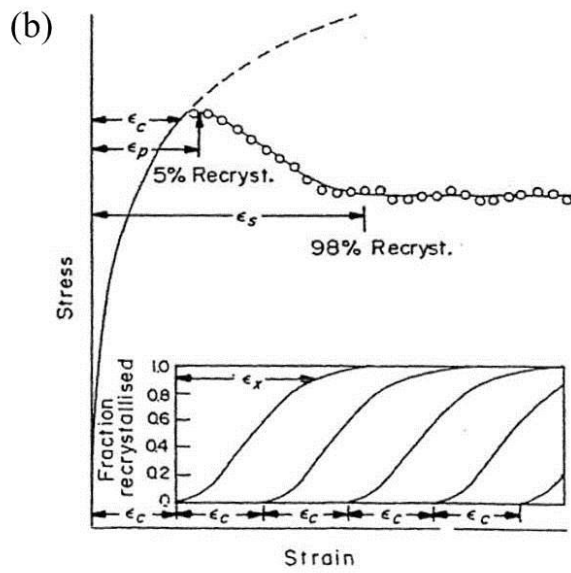
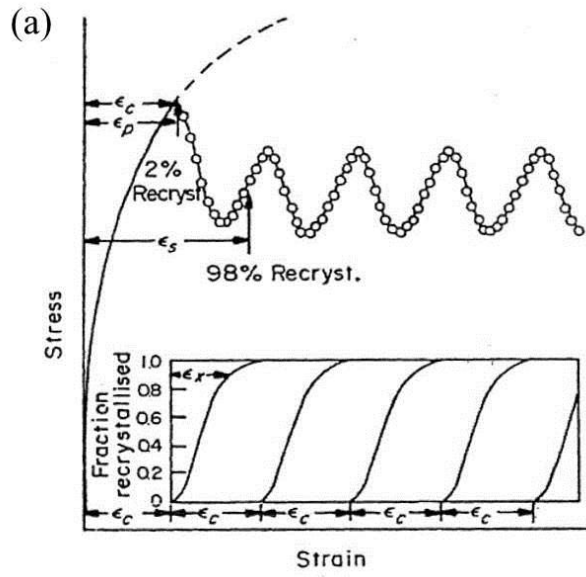
By contrast, if the initial grain size was finer, the DRX was difficult nucleation at more sites; then the DRX could perform to decrease the strain energy, which produced by working hardening. Therefore, the surface energy, which produced by excess grain boundary, could increase, while these surface energy further offered the driving force to help DRX; then making the grains became coarse.

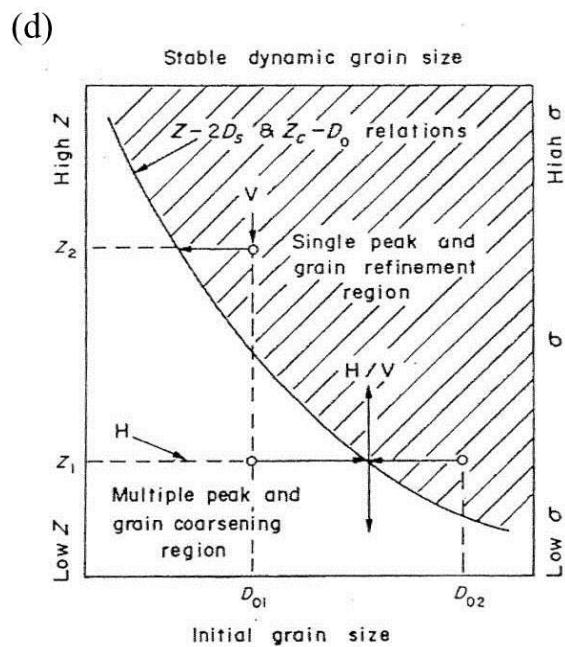
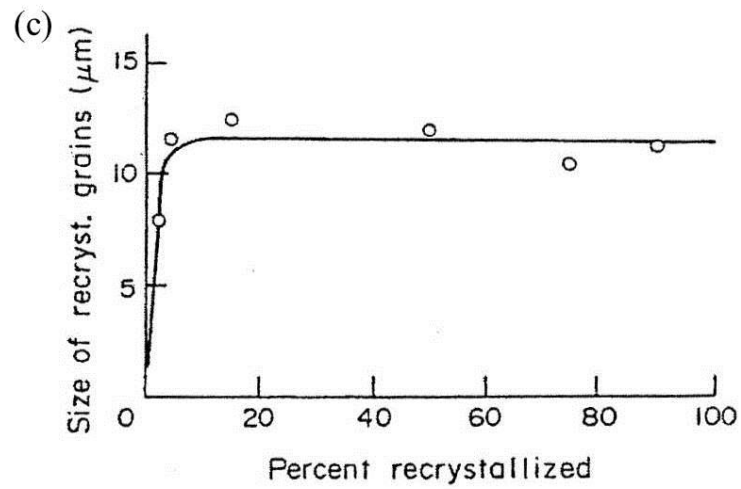
From above all about DRX, the initial grain size played a key role to decide the mechanisms of grain refining or grain coarsening during DRX. However, the deformation temperature was an important factor to decide the DRX performing. Sakai et al. considered that there existed a relationship between the Zener-Hollomon parameter and initial grain size; the Zener-Hollomon parameter showed as following equation (2-3):

$$Z = \dot{\epsilon} \exp(Q / RT) \quad (2-3)$$

where Q was active energy, R gas constant, and T was absolute temperature.

This relationship decided the microstructures, which were grain refining or grain coarsening during deformation process, as shown in Fig. 2-11(d). This figure indicated that if the main method of grain refining was DRX, the Z value could increase with decreasing the size of initial grains.



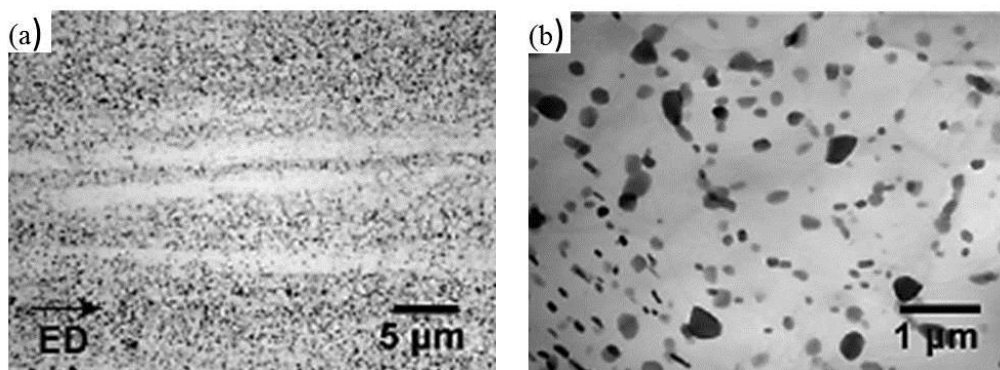


Figs. 2-11 The dynamic recrystallization brief diagram: (a) cycle DRX, (b) continuous DRX, (c) grain growth controlling DRX and (d) Zener-Hollomon parameter map [58].

2.2.2.3 Superplasticity of Mg-Sn based alloys

From above all of section 2.2.2.3, the DRX has been reviewed in detail; this section would focus on the relationship between DRX and superplastic of Mg-Sn based alloys.

Park et al. have investigated that the tensile properties of extruded Mg-8Sn-1Zn (TZ81) alloy subjected to different heat treatments [41]; the authors used SHT (500 °C, 3 hours) + extruding (250 °C, ratio = 50 %) combination process to treat TZ81 alloy. Figs. 2-12(a) and (b) showed that the microstructures of TZ81 alloy; the result exhibited that the SHT + extruding combination process successfully adjusted the microstructure of TZ81 alloy. The average grain size of the alloy was 1.5 μm , which satisfied the stander of superplastic; the authors explained that these fine grains were obtained by DRX during extruding process; then the ultra-fine Mg_2Sn particle effectively resisted the grain growth during extruding at high temperature 250 °C.



Figs. 2-12 (a) OM and (b) TEM micrographs of the extruded TZ81 alloy [41].

They also conducted the deformation evaluating by using tensile test at 250 °C with strain rates $1 \times 10^{-2} \text{ s}^{-1}$ to $1 \times 10^{-4} \text{ s}^{-1}$. The largest tensile elongation attained at a strain rate of $1 \times 10^{-4} \text{ s}^{-1}$ was 670 % in the alloy heat-treated at 500°C as shown in Fig. 2-13. This result give an evidence to prove that the Mg-Sn based alloys had a potential to reach the superplasticity deformation.

Park et al. have further studied extruding Mg-Sn-Al-Zn (TAZ811) alloy by using similar process [35]. Table 2-4 showed the results of tensile test; although the results and trends of TAZ811alloy were very similar with TZ81 alloy, the largest tensile elongation (950 %) has been observed at 200 °C with a fixed strain rate $1 \times 10^{-4} \text{ s}^{-1}$. Moreover, the authors observed an elongation (140 %), which conducted a constant strain rate $1 \times 10^{-1} \text{ s}^{-1}$. This result further proved that the Mg-Sn based alloys had an opportunity to obtain superplastic at high strain rates ($> 1 \times 10^{-1} \text{ s}^{-2}$).

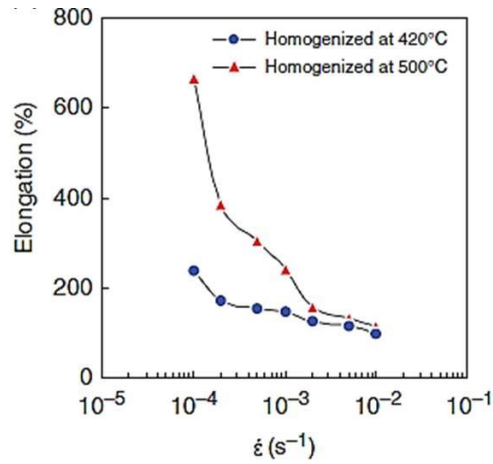


Fig. 2-13 Variations in elongations as a function of strain rate in the TZ81 alloys [41].

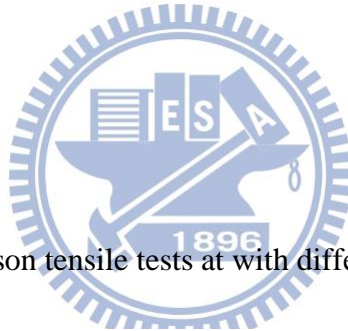
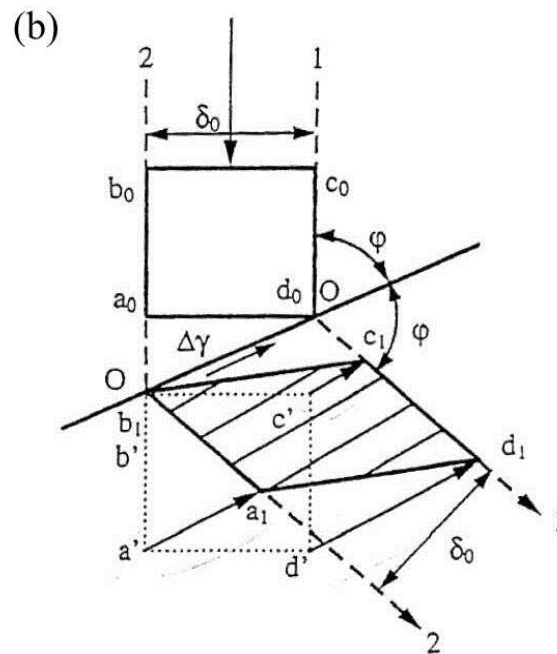
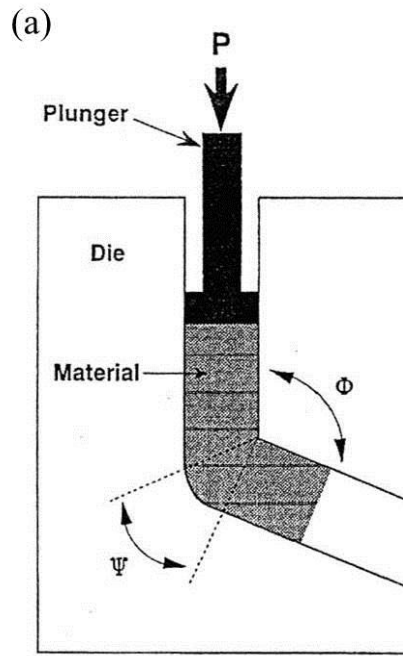


Table 2-4 Comparison tensile tests at with different strain rates [35].

Tensile test		Load-relaxation test		
$\dot{\epsilon}$ (s ⁻¹)	Elongation (%)	$\dot{\epsilon}_{\text{GMD}}$ (s ⁻¹)	$\dot{\epsilon}_{\text{GBS}}$ (s ⁻¹)	$\dot{\epsilon}_{\text{GBS}}/\dot{\epsilon}_{\text{GMD}}$
1 × 10 ⁻⁴	950	6.48 × 10 ⁻⁵	3.52 × 10 ⁻⁵	0.54
2 × 10 ⁻⁴	900	1.44 × 10 ⁻⁴	5.62 × 10 ⁻⁵	0.39
5 × 10 ⁻⁴	540	4.12 × 10 ⁻⁴	8.84 × 10 ⁻⁵	0.21
1 × 10 ⁻³	410	8.89 × 10 ⁻⁴	1.11 × 10 ⁻⁴	0.12
2 × 10 ⁻³	300	1.87 × 10 ⁻³	1.30 × 10 ⁻⁴	0.07
5 × 10 ⁻³	190	4.84 × 10 ⁻³	1.58 × 10 ⁻⁴	0.03
1 × 10 ⁻²	140	9.79 × 10 ⁻³	2.07 × 10 ⁻⁴	0.02

2.3 Equal Channel Angular Extrusion (ECAE)

The Equal Channel Angular Extrusion (ECAE) was invented by scientist Segal [27]. The principle of ECAE was very simple; the pure shear stress was conducted to the sample, while shear strains were produced, and accumulated in the samples by several ECAE passes; then the cross-sectional area of sample was not changing after several ECAE passes. Fig. 2-14(a) demonstrated a schematic diagram of ECAE [59]; the figure showed that the Φ was a stagger angle of route, while the Ψ was an outside arc angle. The sample could subject a shear strain when the sample though the stagger angle (Φ) of the die; then the shear stress was constantly accumulated by pass and pass with different ECAE routes. Fig. 2-14(b) exhibited a geometry changing map of simple shear [60]; the map showed that a large number of plastic deformations were produced by shear plane of the die; then the sample became a parallelogram from a square at the same time because the deformation route had different length ($c \rightarrow c_1 \neq d \rightarrow d_1$). Although the ECAE process was very simple, there were many parameters to affect whole process, like die angle, extruding passes, extruding temperatures, extruding speeds and extruding routes.



Figs. 2-14 Brief diagram of ECAE: (a) ECAE die cross-sectional and (b) geometry

changing map of simple shear [59, 60].

2.3.1 Effect of die angle

Segal et al. have derived the relationship between stagger angle (Φ) and shear strain as shown in equation (2-4) [61]:

$$\gamma = 2 \cot (\Phi/2) \quad (2-4)$$

where γ was shear strain.

Moreover, from the plasticity theory, Segal et al. further derived the relationship between stagger angle (Φ) and equivalent shear strain; the ϵ_{eq} could represent as equation (2-5) [61]:

$$\epsilon_{eq} = (2/\sqrt{3}) \cot (\Phi/2) \quad (2-5)$$

where ϵ_{eq} was an equivalent shear strain.

By equation (2-5), Segal et al. calculated the equivalent shear strain (ϵ_{eq}) after ECAE one pass with different stagger angle (Φ) as shown in Table 2-5. The table showed that the ϵ_{eq} increased with decreasing stagger angle (Φ) after extruding.

Table 2-5 Equivalent shear strain after ECAE a pass with different stagger angle [61].

Tool angle (2Φ)	Punch pressure to flow stress ratio (p/Y)	Incremental strain intensity ($\Delta\epsilon$)	Equivalent reduction ratio (RR)	Equivalent area reduction (AR) %
150°	0.31	0.31	1.37	30
120°	0.68	0.68	1.95	49
90°	1.15	1.15	3.20	69

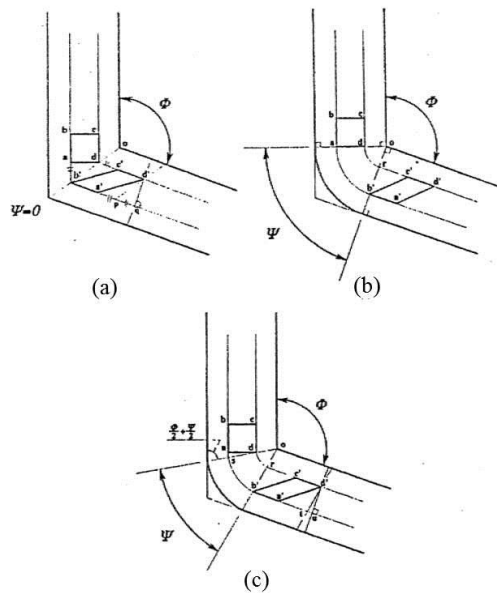
However, Segal et al. specially indicated that the sample could produce a Dead Zone at route bottom when Φ angle was smaller than 90 degree; this phenomenon made that the microstructure of sample demonstrated an uneven deformation after ECAE. Harris et al. have used the finite element analysis to study the similar question; they reported that the sample not easily filled in the stagger angle of route when $\Psi = 0^\circ$ and $\Phi \leq 90^\circ$ [62].

Iwahashi et al. have derived the relationship between ϵ_{eq} and Φ by using geometric relation as shown in Figs. 2-15 (a)-(c) and equation (2-6, 2-7 and 2-8) [63].

(a) If $\Psi = 0^\circ$, $\gamma = 2 \cot (\Phi/2)$ (2-6)

(b) If $\Psi = 180^\circ$, $\gamma = \Phi$ (2-7)

(c) If $0^\circ < \Psi < 180^\circ$, $\gamma = 2 \cot (\Phi/2 + \Psi/2) + \Psi \csc (\Phi/2 + \Psi/2)$ (2-8)



Figs. 2-15 Brief diagram of geometric relation: (a) $\Psi = 0^\circ$, (b) $\Psi = 180^\circ$ and

(c) $0^\circ < \Psi < 180^\circ$ [63].

Nakashima et al. investigated the effect of stagger angle on the microstructure after ECAE process [64]. The authors found that an ECAE process had a vintage extruding stagger angle; they observed that the grain refining consequent of $\Phi = 90^\circ$ was better than that of $\Phi = 135^\circ$. Furthermore, they indicated that the microstructure not only related with amount of total equivalent strain, but also related with amount of plastic deformation, which produced by each ECAE passes.

2.3.2 Effect of extrusion passes

Iwahashi et al. and Tergune et al. studied the effect of extruding passes on the microstructure after ECAE process [65, 66]. The authors used the die ($\Phi = 90^\circ$ and $\Psi = 20^\circ$) to extrude several passes on pure Al by using different ECAE routes. They discovered the banding structure in the sample after ECAE one pass, while these banding structure were composed by elongated sub-grains; the average grain size of these sub-grain was decreased from 1mm to 4 μm by ECAE one pass; then the equiaxial sub-grains were observed after ECAE three passes, while the average grain size decreased from 4 μm to 1 μm . From the above studies, the consequent of grain refining was very obvious by using ECAE with several passes; it means that the total equivalent strains increased with increasing ECAE passes, while the high angle grain boundary significantly increased at the same time. Finally, the average grain size was obviously refined, and gradually tended equiaxial grains.

Chang et al. further proved that this high angle grain boundary evolved from the low angle grain boundary [67]; the authors indicated that these boundary structures could distinguish three types: (a) Polygonized Dislocation Wall (PDW), (b) Grain Boundary (GB) and (c) Partially Transformed Boundary (PTB) as shown in Fig. 2-16. They observed that boundary structure of grains transformed by increasing total equivalent strains; most boundary structures were PDWs when total equivalent strains equaled 2; then the boundary structures evolved from the PDWs to the PTBs when total equivalent strains equaled 4, while there were a few PTBs transformed to the GBs; all the PTBs finally changed to the GBs when equivalent strains reached to 8. From Chang et al. conclusions, increasing the amount of total strain could promote the density of dislocations; thus, it could form the closely dislocation walls to induce subsequent grain refining.

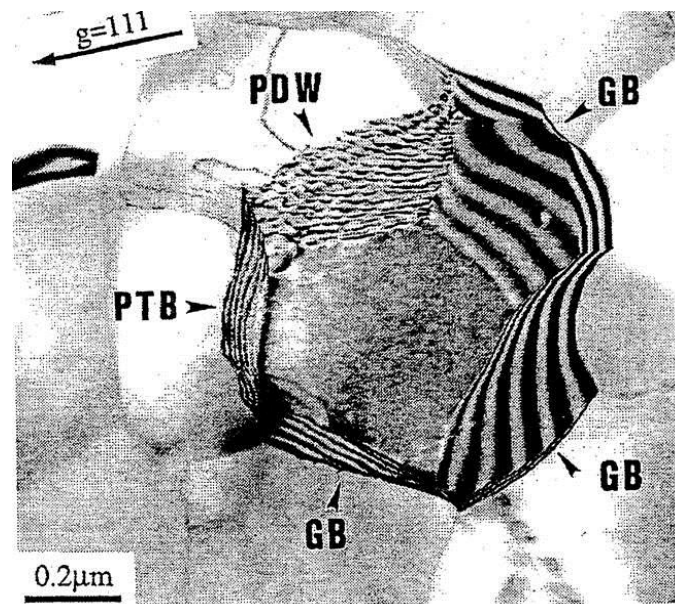


Fig. 2-16 Brief diagram of boundary structures types [67].

2.3.3 Effect of extrusion routes

Segal et al. and Iwahashi et al. have classified the ECAE routes between pass and pass [62, 68]; the authors concluded that there were three main types of ECAE routes, route A, route B and route C, while route B further classified route B_A and route B_C as shown in Fig. 2-17(a) :

(a) Route A: The sample was not rotation after ECAE one pass; then the sample kept the same direction to put in the die. The deformation produced on the different shear plane, while the shear planes could intersect as 90° between pass and pass as shown in Fig. 2-17(b).

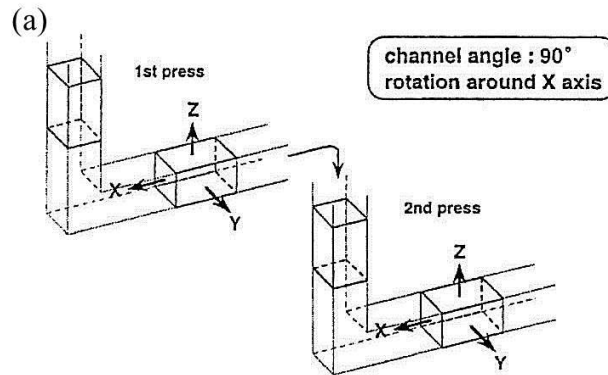
(b) Route B_A: The sample rotated 90° as the clockwise direction after ECAE one pass; then the sample putted in die to extrude in the next time. After ECAE two passes, the sample rotated 90° according to the counterclockwise direction; then the sample putted in die to extrude at the next time as shown in Fig. 2-17(b).

(c) Route B_C: The sample rotated 90° according to the same direction (clockwise or counterclockwise) after ECAE each passes; then the sample putted in die to extrude at the next time as shown in Fig. 2-17(b).

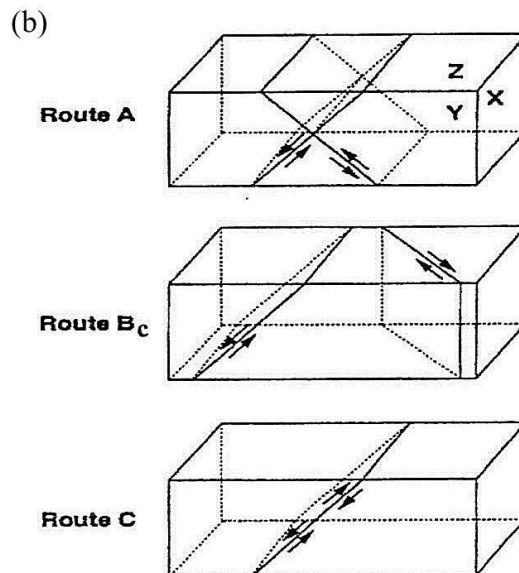
(d) Route C: The sample rotated 180° according to the same direction after ECAE

each passes; then the sample putted in die to extrude at the next time as

shown in Fig. 2-17(b).



	after 1st press	after 2nd press
Route A	0°	0°
Route BA	90° ↷	90° ↶
Route Bc	90° ↷	90° ↷
Route C	180° ↷	180° ↷



Figs. 2-17 Brief diagram of different ECAE routes: (a) rotation degree and (b) shear

plane direction [67, 68].

From the above terms, the deformation could form at different shear planes of the sample when extruding routes changed between each ECAE passes; it means that ECAE route changing made that the microstructure of previous extrusion was affected by next extrusion.

Iwahashi et al. investigated that the microstructure of pure Al transformed by using different ECAE routes [68]. The authors observed that the band structures decreased with increasing ECAE passes by using route A, while the band structures were almost eliminated after ECAE four passes. However, the band structures were not existed in the sample after extruding by using route B_c, while the grains gradually transformed to the equiaxed grains structure after ECAE four passes. The microstructures were very similar between route A and route C; the band structures were major structure, while this structure could gradually eliminate after EACE four passes. As these results, Iwahashi et al. concluded the route B_c easily to obtain the high angle grain boundary; thus, the equiaxed grains structure was observed in route B_C.

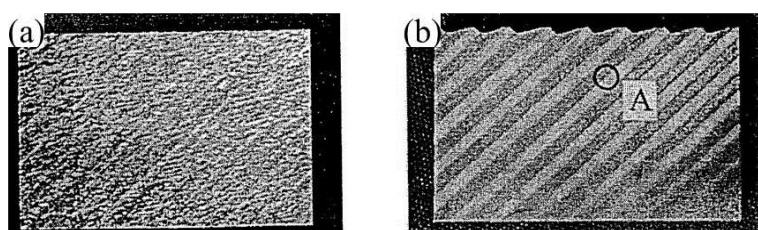
Sun et al. studied a similar report [69]; although the results were very close with Iwahashi et al. reporting [68], the authors stilly found that ability of grain refining had obviously differences between route A, B_c and C. They indicated that the route B_c

could easily obtain an ultra-fine grain structure, while this microstructure simultaneously appeared in the die of stagger angle ($\Phi = 90^\circ$ and $\Phi = 120^\circ$).

2.3.4 Effect of extrusion speeds

Although the average grain size, grain shapes and grain boundary angle were significantly influenced by different ECAE routes, the ECAE speeds also affected the microstructures during whole ECAE process.

Segal et al. have studied the influence of microstructure by different ECAE speeds [70]; the authors observed that the pure Cu produced an uneven deformation after ECAE three passes with extrusion speeds 0.25 mm/s and 25 mm/s as shown in Figs. 2-18 (a) and (b). Additionally, Semiatin et al. have studied a similar result; the authors discovered that the CPTi and 4340 steel could fracture if the ECAE speeds were faster as shown in Fig. 2-19. Berbon et al. used pure Al and Al-1%Mg alloy to extrude with ECAE speeds 7.6 mm/s and 8.5×10^{-3} mm/s at room temperature [71]; the authors indicated that the average grain size seemed no obviously changing after different ECAE speeds, but they further observed that the dynamic recovery phenomenon was induced at lower ECAE speed condition 8.5×10^{-3} mm/s.



Figs. 2-18 Uneven deformation after ECAE: (a) 0.25 mm/s and (b) 25 mm/s [70].

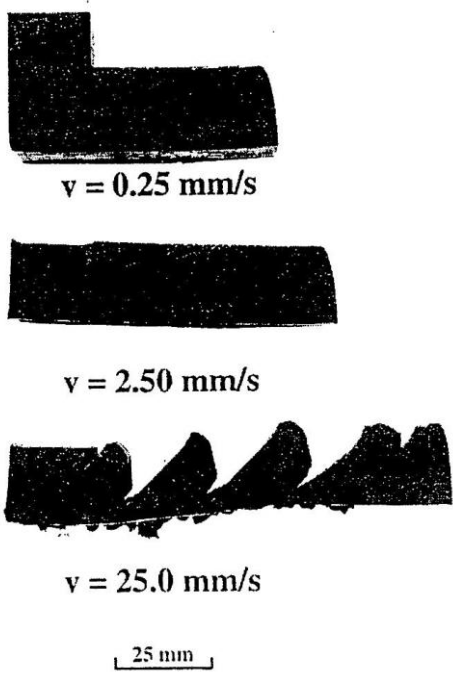
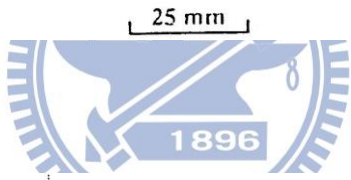
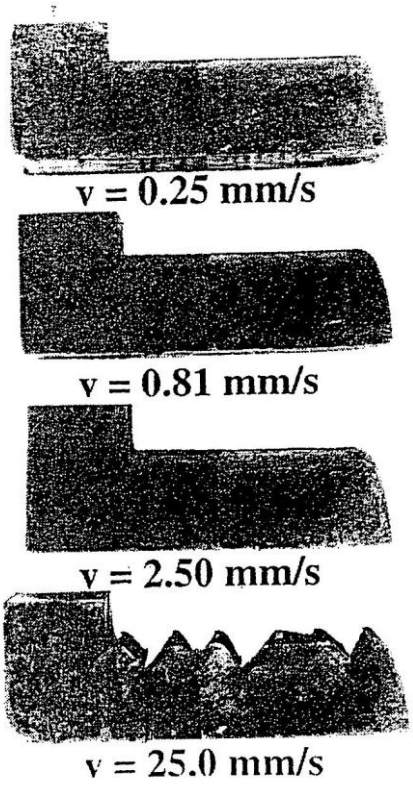


Fig. 2-19 The specimens after EACE process with different speeds [71].

2.3.5 Effect of extrusion temperatures

Yamashita et al. investigated the effect on microstructures of Al-3%Mg-0.2%Sc alloy after ECAE process at room and high temperatures (300 °C) [72]; the results exhibited that the average grain size increased with increasing ECAE temperature, while the grains would become more equiaxed after ECAE twelve passes with route B_C. Chen et al. reported a similar result [73]; the authors observed that a 5052 Al-Mg alloy, which processed ECAE eight passes, had equiaxed grain structure, while the average grain size obviously increased after ECAE at 300 °C. Wang et al. used a 1050 Al alloy to perform ECAE twelve passes at 300 °C [74]; the authors obtain a similar result with Yamashita et al. and Chen et al. According to the above researches, the average grain size, which increased with increasing ECAE temperatures, was a common phenomenon; it means that the thermo energy was very helpful to induce grain coarsening; then coarse grains could affect performance of subsequent mechanical properties at room or high temperatures. In view of this, many authors started to research the ECAE process of multi temperature stages; they attempted to obtain fine grain structure, and avoided grain growth.

Kim et al. studied that the average grain size of AZ31 extruding alloy decreased from 24 μm to 2.2 μm after ECAE six passes, while two passes were 280 °C in the first stage, and last four passes were 220 °C in the second stages [75]. This result

demonstrated that multi stage temperatures controlling were an affect method to obtain fine grain structure during ECAE process.

Matsubara et al. have successfully reduced the average grain size of as-cast AZ91 alloy by using similar method [76]; the average grain size decreased from 50 μm to 0.7 μm . The authors further discovered that the effect of grain refining, which performed two passes at 200 °C (0.7 μm), were smaller than that, which performed four passes at 300 °C (10 μm). Therefore, they indicated that less ECAE passes at lower temperatures were better than more ECAE passes at higher temperatures.

There existed an interesting phenomenon; although the effect of grain refining at lower temperature had better performance, it did not mean that whole ECAE process could 100 % succeed. From above of Matsubara et al. study [76], they broken done the as-cast AZ91 sample after ECAE one pass at 200 °C because the initial grain size 50 μm was too coarsening to extrude by ECAE. Therefore, the authors tried to treat the alloy by using extrusion, while the average size decreased from 50 μm to 12 μm ; then using ECAE continued extruding process. Finally, they successfully obtained the fine grain structure (0.7 μm).

Matsubara et al. further investigated the pure Mg and Mg-0.6 % Zr alloy [77]; the initial grain sizes were respectively 1.4 mm and 70 μm . The authors used pre-extrusion to reduce the initial grain size of samples, while the average grain size

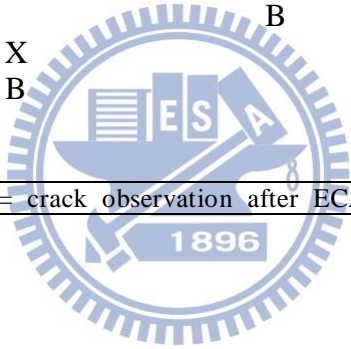
were respectively decreased to 55 μm and 11 μm ; then they used ECAE process to refine the average grain size of the samples; the results were shown in Table 2-6.

From these results [77], Matsubara et al. concluded that the initial grain size was an important factor to influence the ECAE process.

Table 2-6 The results of ECAP with different passes and temperatures [77].

Material	Number of passes	Cast				Cast + Extruded		
		ECAP at T (K)				ECAP at T (K)		
		573	623	673	473	523	573	623
Pure Mg	1	B	X	X		X	X	
	2		B	X		X	X	
	3			B		B	B	
Mg-0.6Zr	1	X			B	A	X	
	2	B				B	X	
	3					X		
	4					X		

X = successfully extruded; A = crack observation after ECAP; B = broken during ECAP



CHAPTER 3 EXPERIMENTAL PROCEDURES

3.1 Alloy designing of Mg-2, 5, 8(wt. %)Sn alloys

In this study, the magnesium alloys, which contained 2, 5, 8 (wt. %) tin elements, were selected. Although the Mg-(1-10)Sn alloys have been investigated by early report [39], the authors just focused on the creep resistance at high temperatures. Therefore, this study would focus on the high temperature tensile properties, and would compare the influence of different tin addition after ECAE process.

3.2 Casting of Mg-2,5, 8(wt. %)Sn alloys

The Mg-Sn alloys with three composition of Mg-2, 5, 8(wt. %)Sn were prepared. Pure magnesium (99.95 wt. %) and 2, 5, 8 (wt. %) pure tin (99.98 wt. %) were melted in a crucible under the protection of SF₆ gas at 800 °C. The melted mixture was stirred to ensure homogeneity. It was then held at 720 °C for 30 min and finally cast into a steel mould that was preheated to 250 °C. The cavity dimensions of the mould were 300 mm × 70 mm × 60 mm.

3.3 ECAE Process of Mg-2, 5, 8(wt. %)Sn alloys

3.3.1 ECAE die preparation and extrusion

ECAE was conducted using a die, which was a block with two intersecting channels of identical cross-section, with a 120° angled channel through the die via a B_C processing route. A B_C processing route means that the sample was removed from

the die, and then rotated by $+90^\circ$ in the same direction between each pass, while 4 passes equaled 1 cycle. The alloy samples were extruded through three stages: The 1, 2 and 4 passes (1 cycle) would extrude in the first stage of the experiments, and the samples would extrude for 2 more passes ($4 + 2 = 6$ passes) in the second stages of the experiments; further, using SHT + ECAE 4 passes two steps process extruded . All samples were extruded at a fixed temperature of 200°C with an extrusion rate of about 2 mm/min. The complete experimental conditions for ECAE were listed in Table 3-1.

3.3.2 Heating and temperature controlling

The die of ECAE was placed in the heating cover, which contained many heating coils; then the die of ECAE was increased the temperature to 200°C by heating cover, while these coils were heated by resistive heating.

ECAE temperature was controlled, and maintained by thermocouple and digital temperature controller. If the temperature changing was detected by thermocouple, the digital temperature controller could feedback, and immediately adjusted the ECAE temperature.

3.4 Mechanical properties test

3.4.1 Hardness test

This study used Vickers hardness (Akashi MVK-H21) to evaluate the micro hardness of Mg-Sn alloys. The load of hardness test was 200 g, and the holding time of test was 30 sec. The test points of test selected 10 points, which were randomly selected; then average micro hardness was calculated from the values of these 10 points.

3.4.2 Tensile test at room temperature

The tensile test was conducted using an Instron8500 at room temperature with a constant strain rate of $1 \times 10^{-3} \text{ s}^{-1}$. Specimens for the tensile test were cut from the ECAE processed samples via wire-electrode cutting, each with a gauge length of 6 mm [37].

The tensile fixture was designed by our self. The specimen was clamped by two wedge clips, while these wedge clips were held in the tensile fixture. The specimen could tightly clamp by tensile fixture when tensile test started.

3.4.3 Tensile test at high temperatures

3.4.3.1 Test for tensile strength

The tensile test was conducted using an Instron8500 at high temperatures 100 °C and 200 °C with a constant strain rate of $1 \times 10^{-3} \text{ s}^{-1}$. The tensile specimens were heated by tubular furnace, while this tubular furnace could open, and close during disassembly tensile specimens. Tensile temperatures were controlled, and maintained

by thermocouple and digital temperature controller. If the temperature changing was detected by thermocouple, the digital temperature controller could feedback, and immediately adjusted the tensile temperatures. The complete experimental conditions for tensile tests at this stage were listed in Table 3-1.

3.4.3.2 Test for superplasticity

In this stage of experiments, the tensile tests were conducted at higher temperatures 250 °C, 300 °C and 350 °C with different strain rates 1×10^{-2} , 1×10^{-3} and $1 \times 10^{-4} \text{ s}^{-1}$. The complete experimental conditions for tensile tests at this stage were listed in Table 3-1.

Table 3-1 The complete experimental conditions for ECAE and tensile tests.

Stages	ECAE process	Tensile tests
Stage 1	1, 2 and 4 ECAE passes at 200 °C	Strain rate = $1 \times 10^{-3} \text{ s}^{-1}$ Temperatures = RT, 100 °C and 200 °C
Stage 2	6 ECAE passes at 200 °C	Strain rates = $1 \times 10^{-2} \text{ s}^{-1}$, $1 \times 10^{-3} \text{ s}^{-1}$ and $1 \times 10^{-4} \text{ s}^{-1}$ Temperatures = 250 °C, 300 °C and 350 °C
Stage 3	SHT at 480 °C for 22 hours + 1, 2 and 4 ECAE passes at 200 °C	Strain rate = $1 \times 10^{-3} \text{ s}^{-1}$ Temperatures = RT, 100 °C and 200 °C

3.5 Characteristic analysis

3.5.1 X-Ray diffraction (XRD) analysis

X-ray diffraction analysis was a kind of non-destructure analytical technique, while it had many applications such as phase identification, crystal structure

identification, orientation of single crystal and preferring orientation. A collimating beam of XRD was incident on the specimen; then the beam of XRD could be diffracted by the crystalline phases of the specimen according to the Bragg's law ($n\lambda = 2d\sin\theta$) during XRD analysis. The diffraction pattern was used to identify the phase of specimen, and to measure the structure properties. In this study, the XRD was used to analysis, and identify the phase of Mg-2, 5, 8(wt. %)Sn alloys by using Bruker/D2 phase system (Cu $K\alpha$, $\lambda = 1.5418 \text{ \AA}$).

3.5.2 Energy Dispersive Spectroscopy (EDS) analysis

The energy dispersive spectroscopy was an instrument, which usually appended on the electron microscope. This device could be applied as accurate electron probe micro-analyzer, efficient and non-destructive elements analysis and investigating element distribution of micro areas in the specimen. This function was very powerful to find unknown elements like metal alloys, polymers and semiconductors. In this study, The EDS analysis would calculate, and confirm the composition ratio of Mg-2, 5, 8(wt. %)Sn alloys and Mg_2Sn phase by using Oxford system.

3.5.3 Optical Microscope (OM) observation

The optical microscope was a very useful instrument to observe the metallographic of metal alloys. Researchers could investigate the size of grains, the

shape of grains and some small cracks of specimen. In this study, the metallographic of Mg-2, 5, 8(wt. %)Sn alloys were be observed by using Olympus BH2-MJLT.

The specimens of metallographic were produced as fowling procedure:

The samples were divided at the same place in each cast and ECAE processed sample; then they were polished by the sandpaper from #100 to #1000, while these specimens were etched with a solution of 5 vol. % nitric acid and ethyl alcohol after polishing.

3.5.4 Scanning Electron Microscope (SEM) observation

There existed that secondary electrons, backscattered electrons, transmitted electrons characteristic X-ray and so forth were emitted from the specimen when the electron probe illuminated the specimen. The SEM was a useful instrument to obtain high resolution image. The surface or cross-section image of specimen could observe by using the second electron detector of SEM. In this study, the morphologies of Mg₂Sn precipitates would be investigated by using SEM (JEOL JSM-6500).

3.5.5 Calculation average grain size distribution

The image software was common in the material science field such as area calculation, pores distribution, precipitates ratio, as well as grain size distribution. Therefore, the average grain size of Mg-2, 5, 8(wt. %)Sn alloys was measured by using the linear intercept method, and the grain size distribution was further calculated by using an imaging software (Image Pro5.0) in this study.

CHAPTER 4 MECHANICAL PROPERTIES

AT ROOM TEMPERATURE

4.1 Motivation

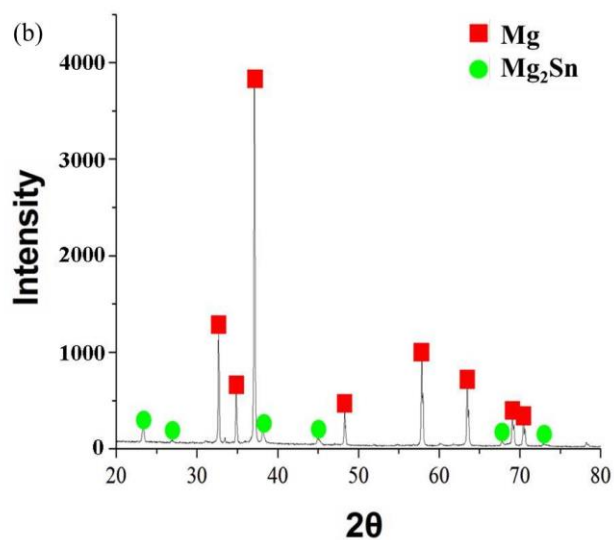
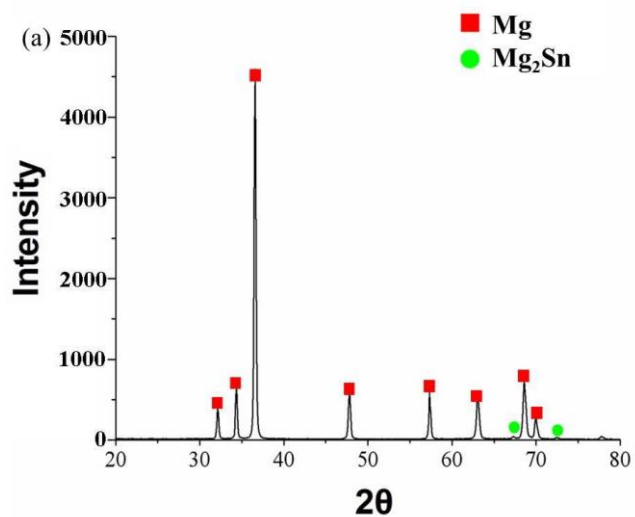
Most conventional Magnesium alloys were based on the Mg–Al alloy system. However, the main β ($\text{Mg}_{17}\text{Al}_{12}$) phase usually precipitated at grain boundary, and obviously showed the shape as continuous and laminar, while this type of precipitates was not conducive tensile properties at room temperature. By contrast, the Mg-Sn alloy system was selected by researchers because Mg-Sn system not only precipitated the α -Mg + Mg_2Sn continuous and laminar phase in the grain boundary, but also directly formed the small Mg_2Sn particles in the α -Mg matrix. Moreover, these continuous and laminar α -Mg + Mg_2Sn phase could break down by subsequent ECAE process. Therefore, this stage would expect that broken and Mg_2Sn particles could enhance the tensile properties at room temperature.

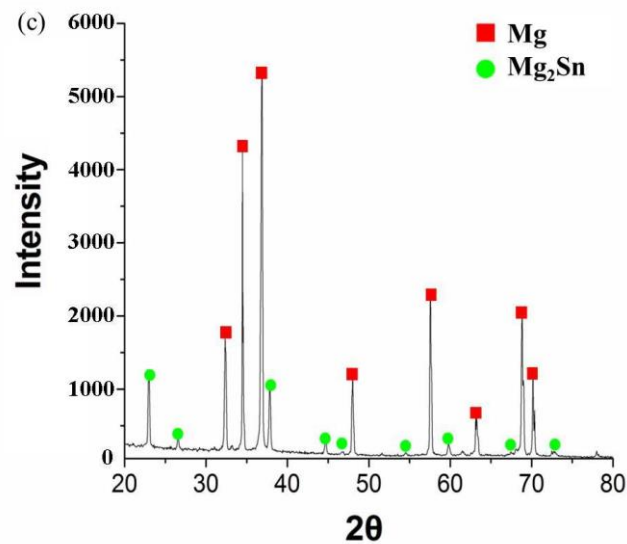
4.2 EDS and XRD analysis

The as-cast Mg-2, 5, 8(wt. %)Sn alloys were examined by EDS analysis as shown in Table 4-1. The results showed all the known elements within the configuration. Figs. 4-1(a)-(c) exhibited the results of XRD, which the phase of α -Mg and Mg_2Sn could clearly be distinguished. It shows that the Mg_2Sn phase diffraction peak intensity increased with increasing tin content.

Table 4-1 EDS composition analysis table.

wt. %	Mg	2 Sn	5 Sn	8 Sn
	Bal.	2.19	5.92	8.84





Figs. 4-1 XRD analysis results: (a) Mg-2(wt. %)Sn, (b) Mg-5(wt. %)Sn and (c) Mg-8(wt. %)Sn.



4.3 Microstructure observation and grain size distribution

4.3.1 In as-cast state

The grain boundary was very clean in the optical micrograph of as-cast Mg-2(wt. %)Sn alloy as shown in Fig. 4-2(a). By contrast, the eutectic α -Mg + Mg₂Sn continuous layered precipitation could be found in the grain boundary of Mg-(wt. %)Sn alloy; then the segregation (core structure) could be observed, while this segregation phenomenon formed during solidification; thus, it caused the dark area near grain boundary as shown in Fig. 4-2(b). The Mg-8(wt. %)Sn alloy as shown in Fig. 4-2(c); it was very obviously that the eutectic α -Mg + Mg₂Sn precipitation

increased with increasing tin content, while the coarsening degree of eutectic α -Mg + Mg₂Sn phase was more obvious than that of Mg-2 and 5(wt. %)Sn alloys.

Liu et al. have found a similar result; the authors observed that the Mg-10Sn alloy demonstrated the most coarsening α -Mg + Mg₂Sn phase in the Mg-(1-10)Sn alloys [39].

The SEM micrographs of Mg-2, 5, 8(wt. %)Sn alloys showed a large amount of ultra-fine particles in the matrix of which were between 80nm to 120nm in length as shown in Figs. 4-3(a)-(c). These ultra-fine particles of as-cast Mg-2, 5, 8(wt. %)Sn alloys were identified by EDS as shown in Table 4-2; this analysis found that Mg : Sn = 1 : 2; thus, this result confirmed that the particles were indeed Mg₂Sn.

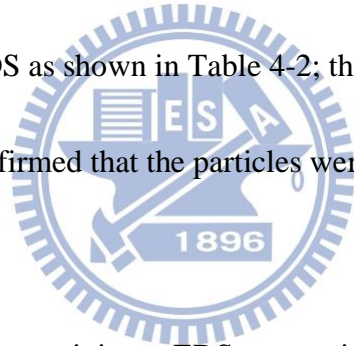
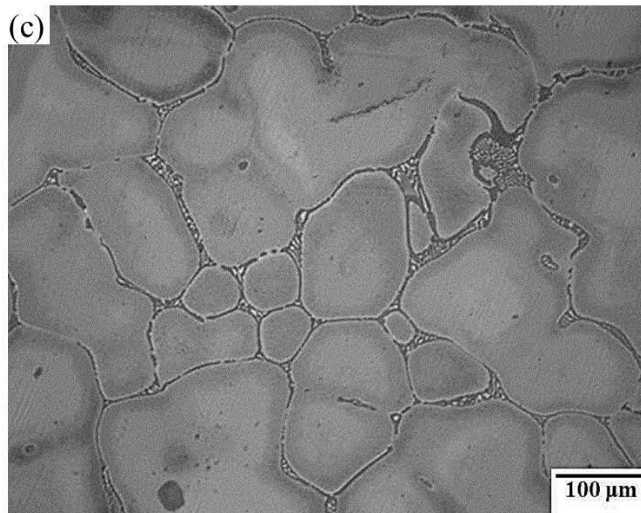
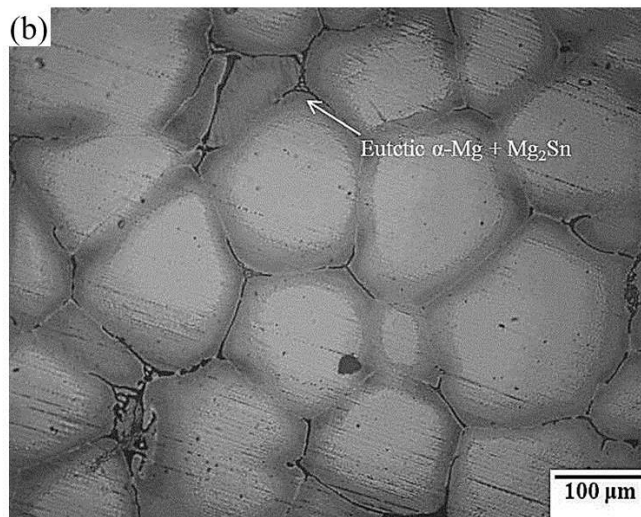
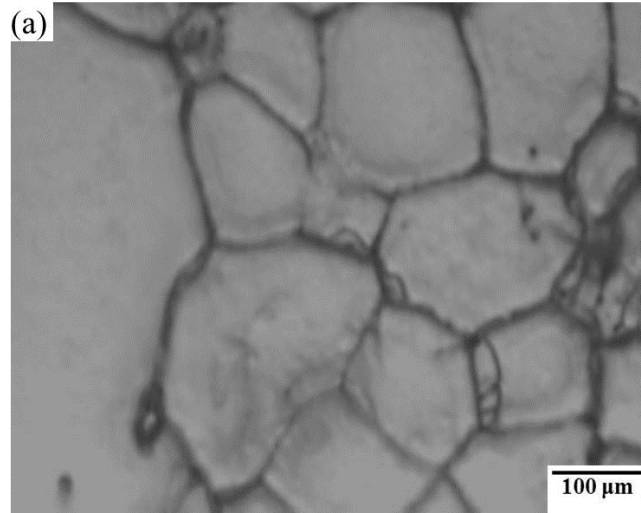
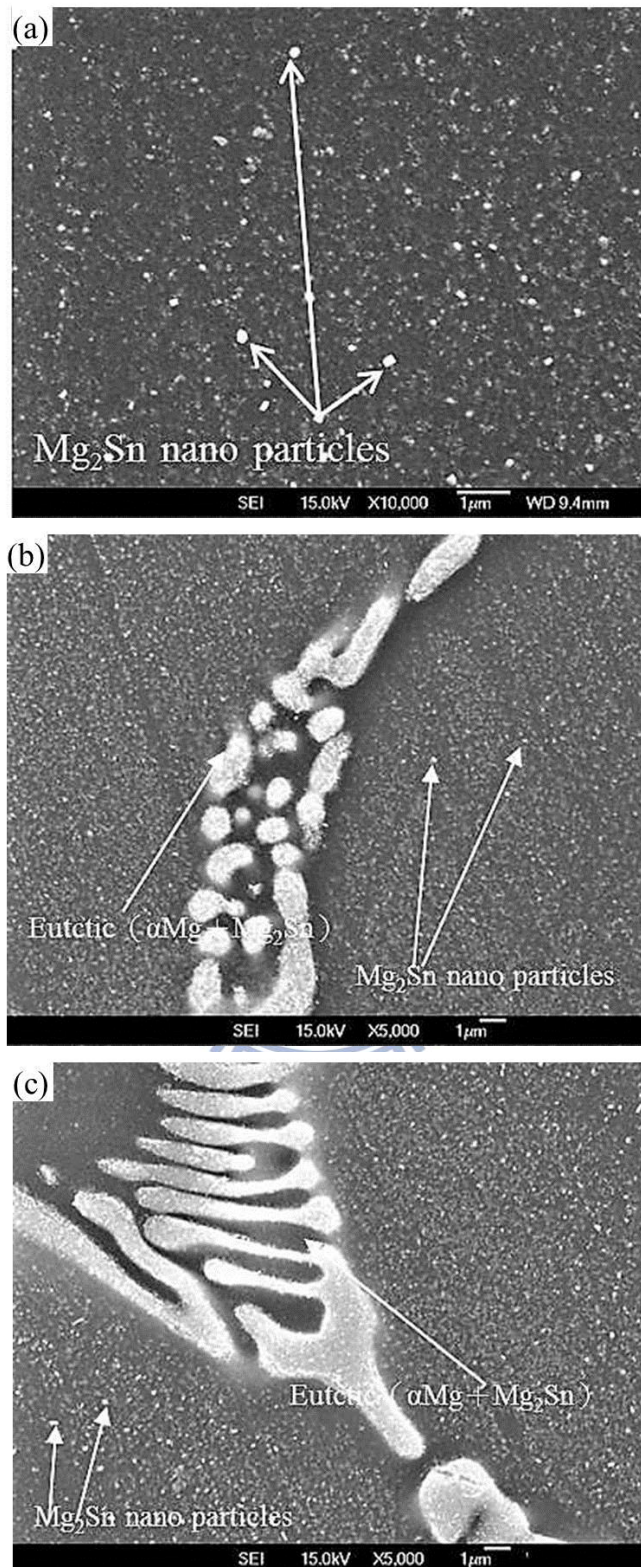


Table 4-2 Mg₂Sn precipitates EDS composition analysis table.

Element (at. %)	Mg-2%Sn	Mg-5%Sn	Mg-8%Sn
Mg K	36.02	34.17	36.09
Sn L	63.17	64.88	65.91



Figs. 4-2 OM images of as-cast state: (a) Mg-2(wt. %)Sn, (b) Mg-5(wt. %)Sn and
(c) Mg-8(wt. %)Sn.



Figs. 4-3 SEM images of as-cast state: (a) Mg-2(wt. %)Sn, (b) Mg-5(wt. %)Sn and (c) Mg-8(wt. %)Sn.

Comparing three components in the as-cast state Mg-2, 5, 8(wt. %)Sn alloys; then the average grain size was calculated, while the average grain size of Mg-2(wt. %)Sn alloy (296 μm) was larger than that of Mg-5(wt. %)Sn (147 μm) and Mg-8(wt. %)Sn alloy (106 μm) . These results were estimated from the Growth Restriction Factor (GRF) as shown in following equation (4-1) [78]:

$$\text{GRF} = mc_0 (k - 1) \quad (4-1)$$

where m was liquidus slope of binary phase diagram; c_0 was tin content, and k was solute partition coefficient.

From the literature [79], $m(k-1) = 1.47$ was grain refining effect of tin element, substituting the tin content into c_0 could be got different GRF values as shown in Table 4-3, which showed that GRF values were positive. This result proved that tin content could produce different degrees of grain refinement.

Table 4-3 Mg-X(wt. %)Sn Growth Restriction Factor (GRF) table.

Composition	Sn wt. %	GRF
Mg-2% Sn	$c_0 = 0.02$	0.0249
Mg-5% Sn	$c_0 = 0.05$	0.0735
Mg-8% Sn	$c_0 = 0.08$	0.1176

4.3.2 After ECAE four passes

ECAE process was a type of thermo-mechanical treatment; the thermo energy and shear strain energy could be produced at the same time during extrusion process.

Additionally, the magnesium alloys were HCP structure, which only had three sliding

systems at room temperature. Therefore, grain refining in magnesium alloys will

nucleation along the preexisting grain boundaries at 200 °C during ECAE process,

while this nucleate was attributed to the development of stress concentrations at the

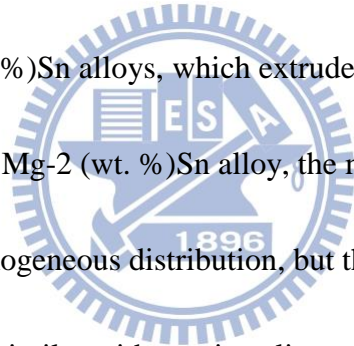
boundaries and the subsequent activation process of both basal and non-basal slip [80].

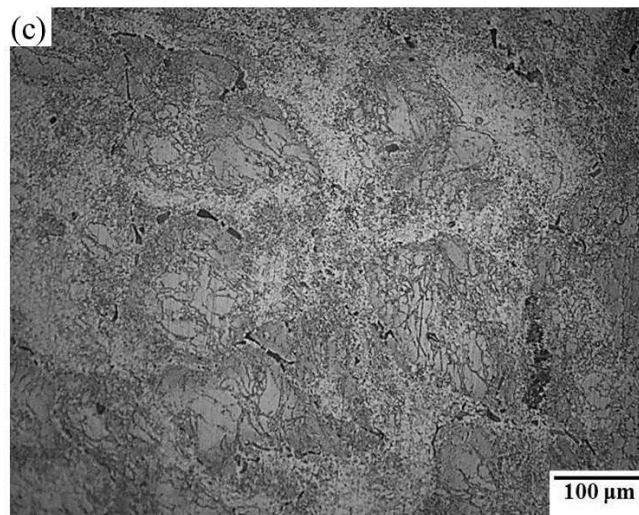
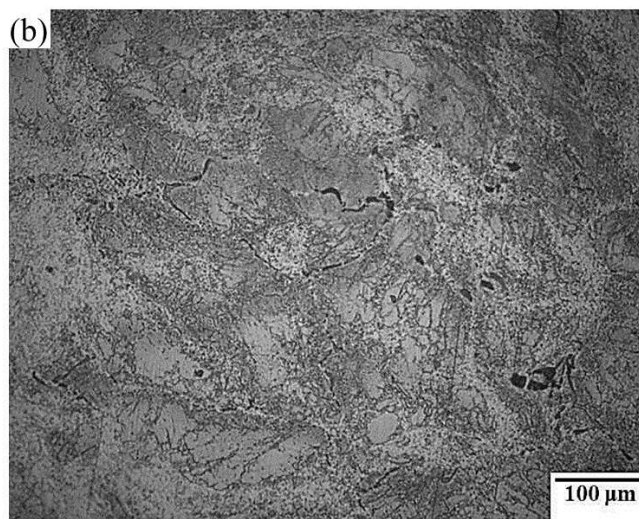
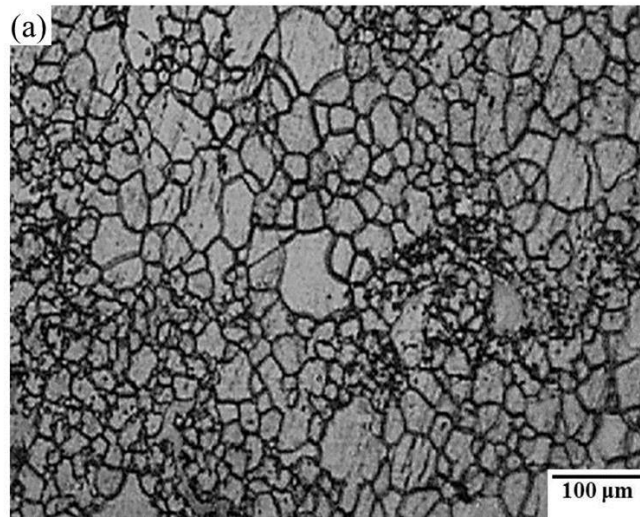
The result of Mg-2, 5, 8(wt. %)Sn alloys, which extruded four passes, was shown in

Figs. 4-4(a)-(c). Besides the Mg-2 (wt. %)Sn alloy, the microstructures of Mg-5 and

8(wt. %)Sn alloys were homogeneous distribution, but there also existed some large

grains. This result was very similar with previous literature [81, 82].

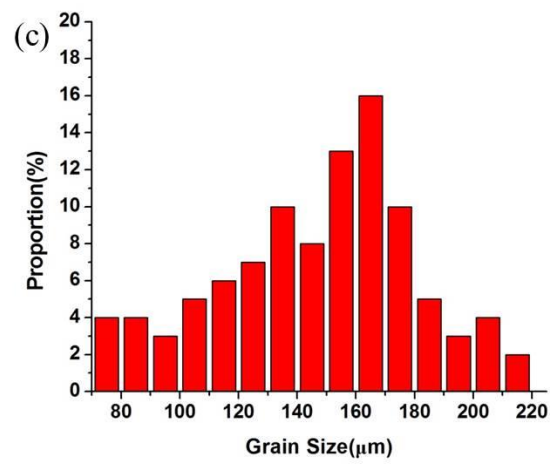
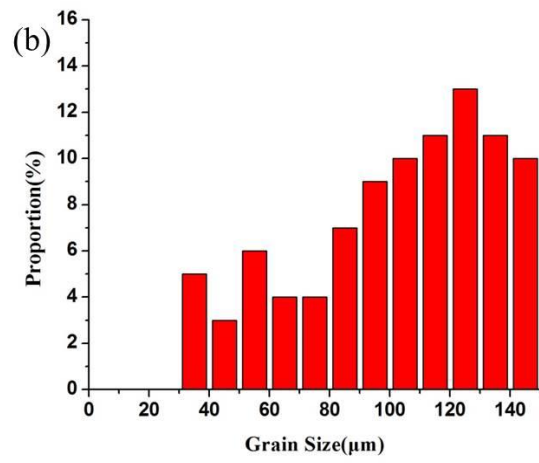
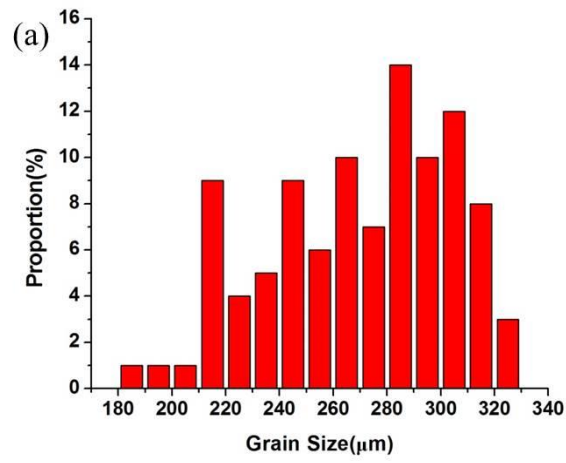


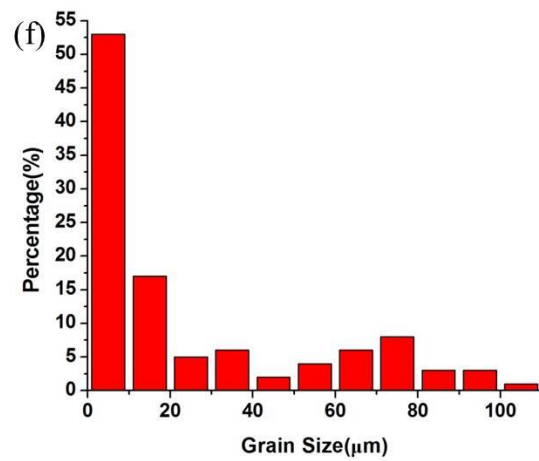
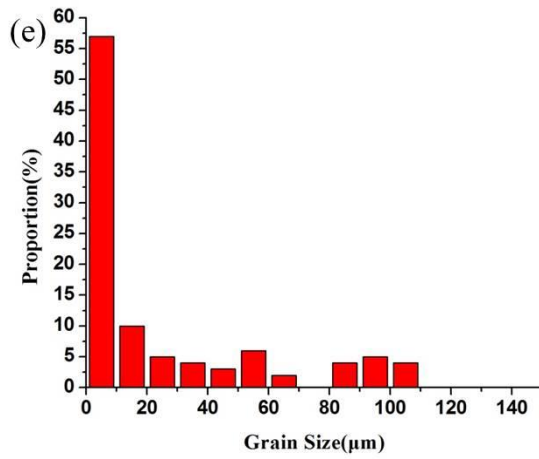
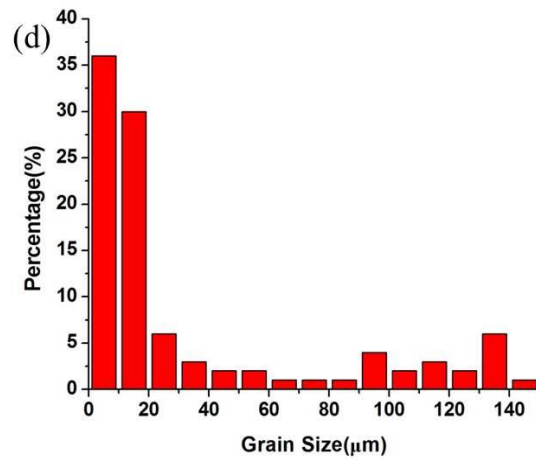


Figs. 4-4 OM images of ECAE four passes: (a) Mg-2(wt. %)Sn, (b) Mg-5(wt. %)Sn
and (c) Mg-8(wt. %)Sn.

The grain size distributions with different tin content of Mg-2, 5, 8(wt. %)Sn alloys were shown in Figs. 4-5(a)-(f). Comparing the percentage of average grain size (0-10 μm) for Mg-2(wt. %)Sn alloy could reach from 0 % to 37 %, while the percentage of Mg-5 and 8(wt. %)Sn alloys respectively reached from 0 % to 54 % and 58 %.

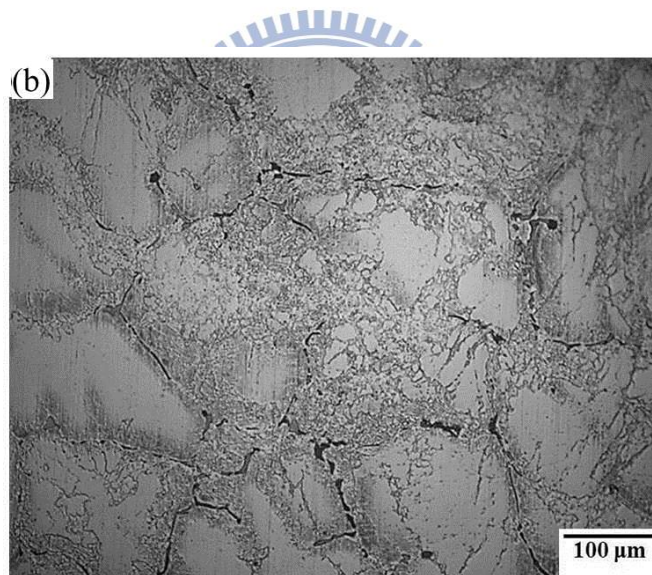
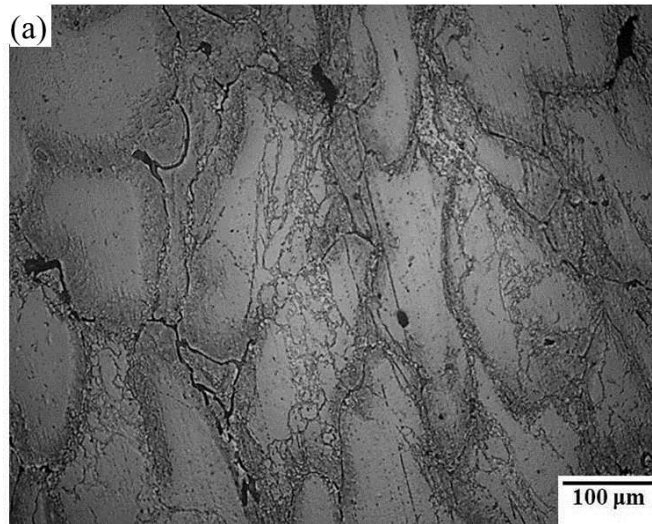


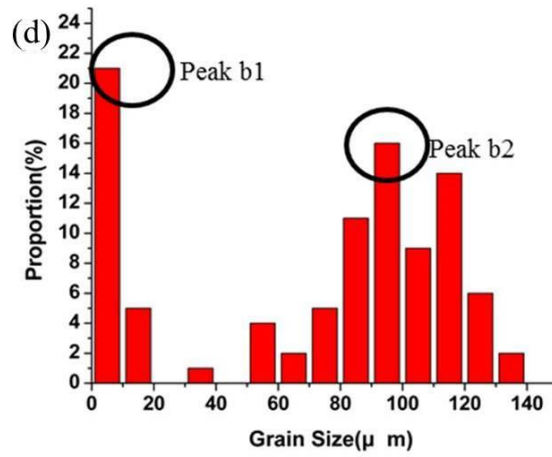
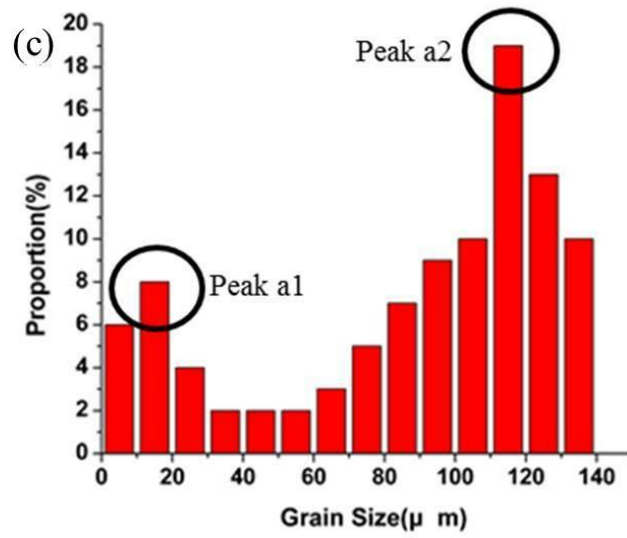




Figs. 4-5 Grain size distribution maps: (a) as-cast Mg-2(wt. %)Sn , (b) as-cast Mg-5(wt. %)Sn, (c) as-cast Mg-8(wt. %)Sn, (d) Mg-2(wt. %)Sn N = 4, (e) Mg-5(wt. %)Sn N = 4 and (f) Mg-8(wt. %)Sn N = 4.

It was worth noting that the microstructures of Mg-2, 5, 8(wt. %)Sn alloys after ECAE one and two passes showed the bi-model distribution. For example, the OM images of Mg-5(wt. %)Sn alloy after ECAE one and two passes were exhibited as shown in Figs. 4-6(a) and (b), while the grain size distribution of were respectively drew the grain size distribution maps, as shown in Figs. 4-6(c) and (d). The grain size distribution maps could explain that the microstructures of Mg-5(wt. %)Sn alloy evaluate from the bi-model distribution to the homogeneous distribution by DRX. Fig. 4-6(c) was a grain size distribution map of ECAE one pass; the map showed dual peaks at right side (peak a1) and left side (peak a2) on the map; it was very obviously to index that the fine grain area and coarse grain area independently distributed; thus, the microstructure of Mg-5(wt. %)Sn alloy formed the bi-model distribution after ECAE one pass. Likewise, it was very significantly to index dual peaks on the map after ECAE two passes, as shown in Fig. 4-6(d); however, the peak b1 was higher than that of peak b2; it means that the DRX was very helpful to produce fine grains during ECAE process; thus, inducing the fine grain area increased with increasing ECAE passes. Finally, the dual peak model changed to the single peak model; the percentage of average grain size (0-10 μm) for Mg-5(wt. %)Sn alloy reached 54%.





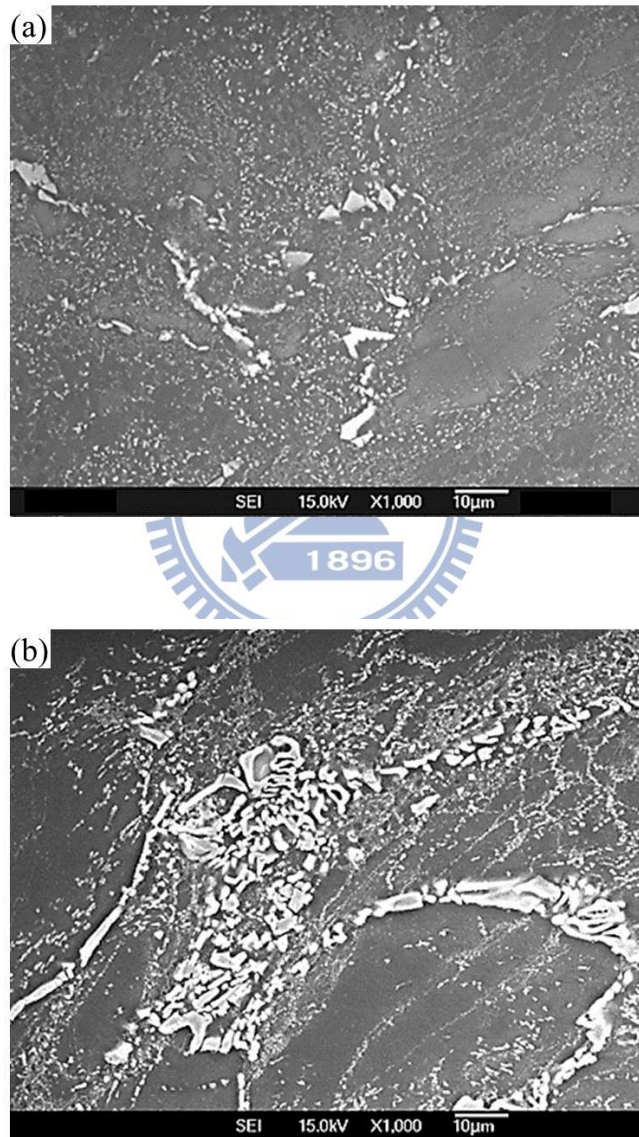
Figs. 4-6 (a) OM image of Mg-5(wt. %)Sn N = 1, (b) OM image of Mg-5(wt. %)Sn N = 2, (c) grain size distribution map of Mg-5(wt. %)Sn N = 1 and (d) grain size distribution map of Mg-5(wt. %)Sn N = 2.

Further, the average grain size of Mg-2, 5, 8(wt. %)Sn alloys after ECAE four passes was calculated as shown in Table 4-4; the trend of these results matched with the grain size distribution of Mg-2, 5, 8(wt. %)Sn alloys. For example, the average grain size of Mg-5(wt. %)Sn alloy increased from 147 μ m (as-cast) to 28 μ m after ECAE four passes; it means that the thermo energy and shear strain energy were significantly helpful to induce grain refining, while the mechanism of grain refinement was dynamic recrystallization (DRX) during ECAE process.

On the other hand, The Mg-5 and 8(wt. %)Sn alloys formed the continuous eutectic α -Mg + Mg₂Sn precipitates in the grain boundary before ECAE. However, after ECAE four passes, the continuous eutectic α -Mg + Mg₂Sn was broken, and formed discontinuous precipitation of Mg₂Sn particles as shown in Fig.4-7(a); then these Mg₂Sn particles could distribute more uniform after ECAE four passes than that of as-cast Mg-5(wt. %)Sn alloy. The result of Mg-8(wt. %)Sn alloy was similar to that of Mg-5(wt. %)Sn alloy after ECAE four passes as shown in Fig. 4-7(b). However, the Mg-8(wt. %)Sn alloy had higher tin content, which induced more volume fraction of continuous eutectic α -Mg + Mg₂Sn precipitates; then it leads that the shearing effect on ECAE was not better than that of Mg-5(wt. %)Sn alloy. It could be obviously seen that the eutectic α -Mg + Mg₂Sn precipitates were maintained geometric shape before ECAE four passes.

Table 4-4 Average grain size of Mg-2, 5, 8(wt. %)Sn alloys.

ECAE passes	N = 0 (as-cast)	N = 1	N = 2	N = 4
Mg-2(wt. %)Sn	213.0 μm	125.7 μm	87.0 μm	43.6 μm
Mg-5(wt. %)Sn	147.0 μm	87.5 μm	69.7 μm	28.0 μm
Mg-8(wt. %)Sn	106.0 μm	77.1 μm	51.4 μm	22.3 μm



Figs. 4-7 SEM images: (a) Mg-5(wt. %)Sn N = 4 and (b) Mg-8(wt. %)Sn N = 4.

4.4 Vickers hardness test

Table 4-5 showed the Vickers hardness test results; the hardness increased with increasing tin content, while the Mg-8(wt. %)Sn alloy had the highest hardness after ECAE four passes (HV = 59.9) . The main reason for this result was effect of grain refining; when micro-indentation imposed deformation to the Mg-8(wt. %)Sn alloy, the grain boundaries could resist dislocations migration. Moreover, the high-density Mg₂Sn ultra-fine particles, which distributed in the α -Mg matrix, also had obvious contribution; it could form stress field to further resist dislocations migration. Therefore, the factors of both grain boundaries and Mg₂Sn ultra-fine particles significantly produced Mg-8(wt. %)Sn alloy to reach the highest hardness.

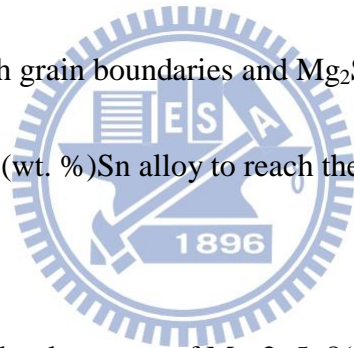


Table 4-5 HV hardness test of Mg-2, 5, 8(wt. %)Sn alloys.

HV (100gf)	Mg-2(wt. %)Sn	Mg-5(wt. %)Sn	Mg-8(wt. %)Sn
As-cast	35.9	46.4	49.9
N = 1	41.8	50.9	56.1
N = 2	43.0	51.3	55.0
N = 4	42.8	55.8	59.9

4.5 Tensile test at room temperature

Both Yield Strength (YS) and Ultimate Tensile Strength (UTS) of Mg-2, 5, 8(wt. %)Sn alloys could increase with increasing ECAE passes at room temperature as shown in Figs. 4-8(a)-(c); the detail values of tensile properties were listed in the Table 4-6.

Especially the Mg-5(wt. %)Sn alloy, the YS significantly increased from 104 MPa to 270 MPa at room temperature, while this result was also consistent with Hall-Petch Equation's prediction, which the alloy strength was inversely with average grain size. The UTS of Mg-2, 5, 8(wt. %)Sn alloys had a similar trend with YS. The UTS of Mg-5(wt. %)Sn alloy obviously increased from 126 MPa to 327 MPa at room temperature.

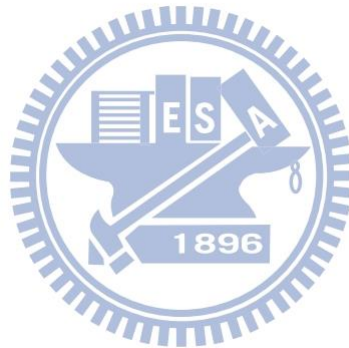
Additionally, the elongations of Mg-2, 5, 8(wt. %)Sn alloys were shown in Figs. 4-9(a)-(c); the elongation slightly increased from 7.9 % to 9.5 % at room temperature for Mg-5(wt. %)Sn alloy after ECAE four passes, while this result might cause by Mg₂Sn particles resisting because these Mg₂Sn particles could pin grain boundary sliding during tensile test at room temperature.

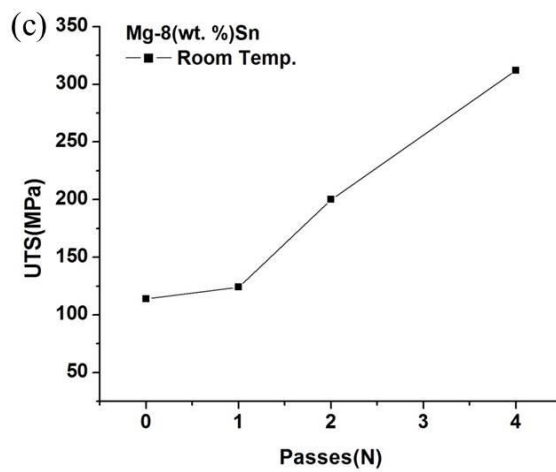
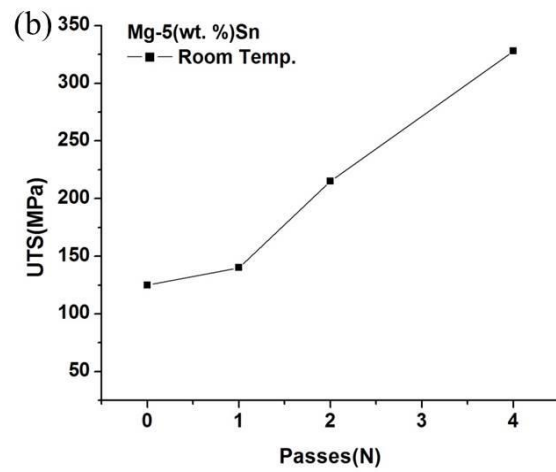
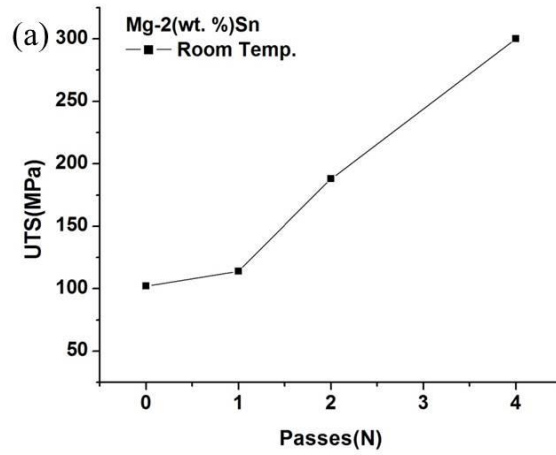
Although the Mg-8(wt. %)Sn alloy had the highest hardness, but the YS and UTS of this alloy were lower than that of Mg-5(wt. %)Sn alloy; there existed a key reason to explain this phenomenon. The Mg-8(wt. %)Sn alloy contained the highest

density of continuous eutectic α -Mg + Mg₂Sn precipitates, which had very hard and brittle phase (HV = 121); thus, the cracks initiation would have more opportunities to form between the interface of α -Mg matrix and Mg₂Sn precipitates.

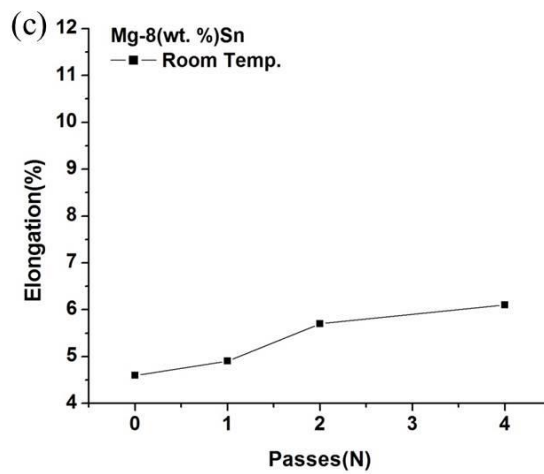
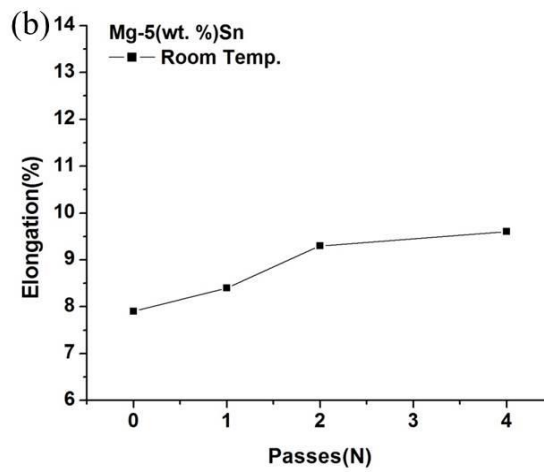
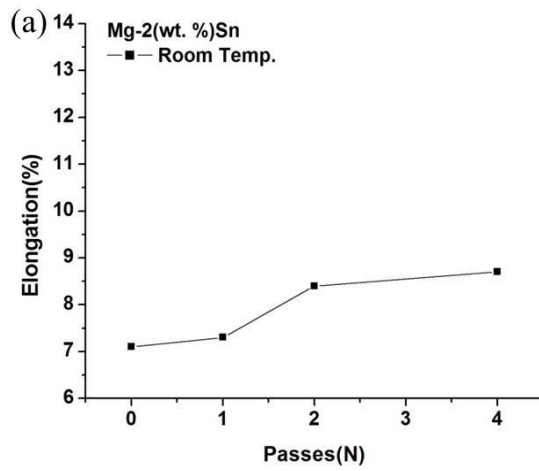
Table 4-6 Tensile properties of Mg-2, 5, 8(wt. %)Sn alloys after ECAE process.

ECAE passes	YS (MPa) & UTS (MPa)						Elongations (%)		
	Mg-2Sn		Mg-5Sn		Mg-8Sn		Mg-2Sn	Mg-5Sn	Mg-8Sn
N = 0	81	101	104	126	99	120	7.1	7.9	4.6
N = 1	99	125	113	137	105	127	7.4	8.4	4.9
N = 2	146	180	186	225	167	202	8.5	9.2	5.8
N = 4	249	299	270	327	253	320	8.9	9.5	6.2





Figs. 4-8 Tensile strength with different ECAE passes: (a) Mg-2(wt. %)Sn, (b) Mg-5(wt. %)Sn and (c) Mg-8(wt. %)Sn.

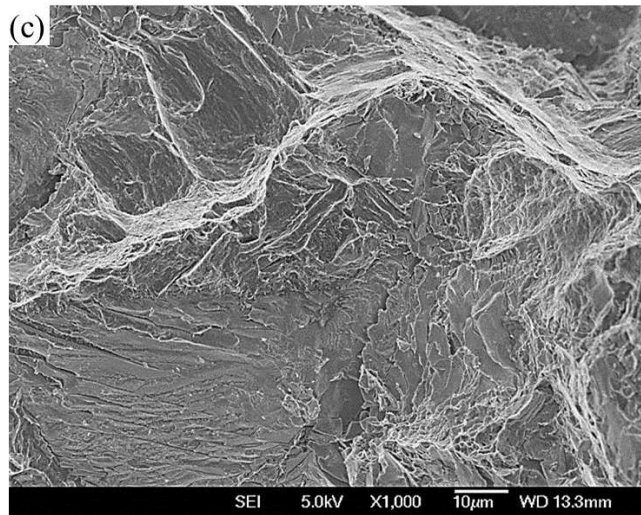
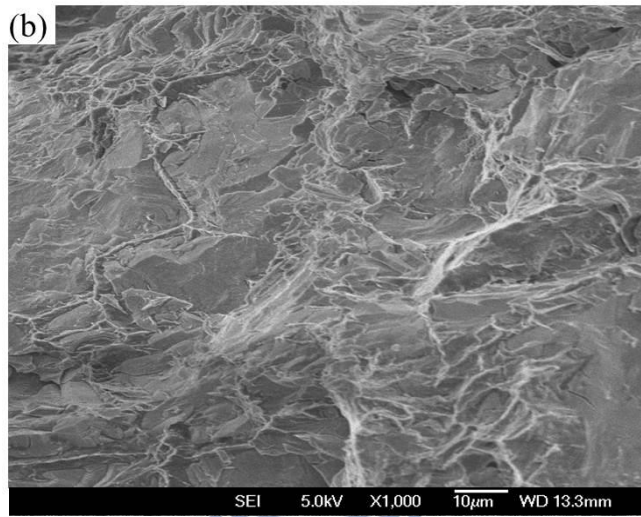
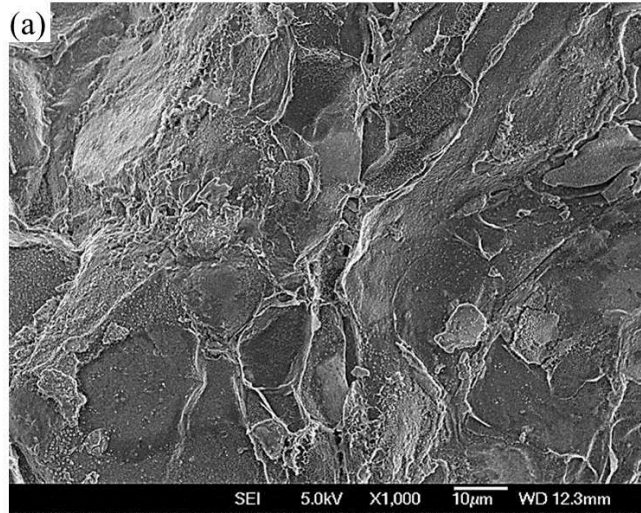


Figs. 4-9 Elongations with different ECAE passes: (a) Mg-2(wt. %)Sn, (b) Mg-5(wt. %)Sn and (c) Mg-8(wt. %)Sn.

4.6 Fracture surface observation

The failure of magnesium alloy was brittle through cleavage or quasi-cleavage with a H.C.P structure at room temperature [83]. Figs. 4-10(a)-(c) was the fracture surface of Mg-2, 5, 8(wt. %)Sn alloys after ECAE four passes, which conducted tensile test at room temperature with a fixed strain rate $1 \times 10^{-3} \text{ s}^{-1}$. The figures exhibited that all fracture surface was composed of cleavage at room temperature, while a number of cleavages and steps were presented. This result indicated that the major fracture mode of Mg-2, 5, 8(wt. %)Sn alloys after tensile test at room temperature was brittle fracture; thus, many cleavages formed during tensile test.





Figs. 4-10 Fracture surface after tensile test with a fixed strain rate $1 \times 10^{-3} \text{ s}^{-1}$: (a)

Mg-2(wt. %)Sn, (b) Mg-5(wt. %)Sn and (c) Mg-8(wt. %)Sn.

4.7 Summary

From above all, the Mg-2, 5, 8(wt. %)Sn alloys have been detail investigated in the chapter 4. Adding tin in the magnesium alloy was helpful for grain refinement of as-cast Mg-2, 5, 8(wt. %)Sn alloys, while the average grain size of these alloys respectively reached as Mg-2(wt. %)Sn (213 μm), Mg-5(wt. %)Sn (147 μm) and Mg-8(wt. %)Sn (106 μm); the effect of grain fining was very obvious by tin increasing. Moreover, the continuous eutectic $\alpha\text{-Mg} + \text{Mg}_2\text{Sn}$ phase of Mg-2 and 8(wt. %)Sn alloys could be observed, while the these precipitates increased with increasing tin content. Furthermore, the Mg-2, 5, 8(wt. %)Sn alloys produced large amounts of fine grains, and the minimal percentage of average grain size (0-10 μm) was more than 35 % after ECAE four passes. Especially, the Mg-5(wt. %)Sn alloy had the best tensile properties after ECAE four passes; the YS and UTS had a similar trend, while the UTS reached 328 MPa at room temperature, and the elongation still retained about 9.6 %. The fracture surface of Mg-5(wt. %)Sn alloy after tensile test at room temperature was cleavage; it means that the main fracture mode was still the brittle after ECAE four passes.

CHAPTER 5 MECHANICAL PROPERTIES

AT HIGH TEMPERATURES

5.1 Motivation

Although the tensile strength at room temperature have been successfully improved in the chapter 4 by using an ECAE process, the applications of Mg-Sn alloys at high temperatures were a very critical issue. The Mg_2Sn particles, which have existed in the α -Mg matrix or been broken down by ECAE process, played a key role to enhance the tensile properties at high temperatures because the Mg_2Sn particles owned a higher melting point (770 °C) than that of 462 °C for β phase $-Mg_{17}Al_{12}$. It means that the Mg-Sn alloys might have an opportunity to further promote the tensile strength of Mg-Sn alloys at high temperatures. Therefore, this chapter expected to improve the tensile strength at high temperatures 100 °C and 200 °C by using ECAE four passes extrusion. In addition, this chapter would further evaluate the superplastic ability. Although the commercial magnesium alloys (AZ31 or ZK60) have applied the superplastic deformation on the 3C or mobile fields, the applications at high temperatures seemed not good enough. Therefore, this chapter chosen the Mg-5(wt. %)Sn alloy to evaluate the superplastic ability at higher temperatures 250 °C to 350 °C, while the Mg-5(wt. %)Sn alloy possessed the best

tensile strength and elongations between Mg-2, 5, 8(wt. %)Sn alloys at room temperature.

5.2 Tensile strength at high temperatures

5.2.1 YS and UTS

The Yield Strength (YS) and Ultimate Tensile Strength (UTS) of Mg-2, 5, 8(wt. %)Sn alloys significantly increased at high temperatures 100 °C and 200 °C after ECAE four passes as shown in Figs. 5-1(a)-(c), while the tensile strength of these alloys increased with increasing ECAE passes. All the tensile properties were showed in the Table 5-1; the Mg-5(wt. %)Sn alloy still had the best performance at high temperatures; the YS respectively increased from 74 MPa to 176 MPa at 100 °C ,and from 40 MPa to 108 MPa at 200 °C. It means that these results were stilly consistent with Hall-Petch Equation's prediction at high temperatures, while the alloy strength was inversely with grain size. The UTS of Mg-2, 5, 8(wt. %)Sn alloys has a similar trend with YS. The UTS of the Mg-5(wt. %)Sn alloy obviously enhanced from 103 MPa to 248 MPa at 100 °C, as well as from 67 MPa to 179 MPa at 200 °C. In addition, the elongations of Mg-2, 5, 8(wt. %)Sn alloys were shown in Figs. 5-2(a)-(c); while the elongations of Mg-2, 5, 8(wt. %)Sn alloys exhibited a similar trend after tensile test at high temperatures. The elongations of the Mg-5(wt. %)Sn alloy demonstrated the largest deformation at high temperatures, while the elongations of

this alloy evidently increased from 9.7 % to 14.5 % at 100 °C, and from 10.6 % to 18.9 % at 200 °C after ECAE four passes.

At high temperature conditions, even though the Mg-8(wt. %)Sn alloy had the highest tin content, the YS and UTS of this alloy at high temperatures 100 °C and 200 °C were still lower than that of Mg-5(wt. %)Sn alloy. This result seemed very similar with room temperature condition; it could be explained that the high density continuous eutectic α -Mg + Mg₂Sn precipitates were very stable even at high temperatures; thus, these thermo stable precipitates still became the sites of cracks initiation during tensile test at high temperatures.

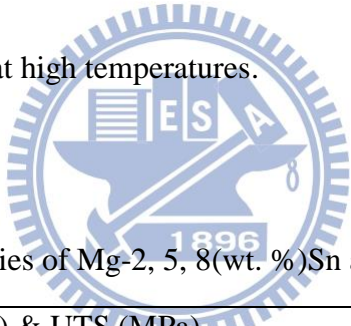
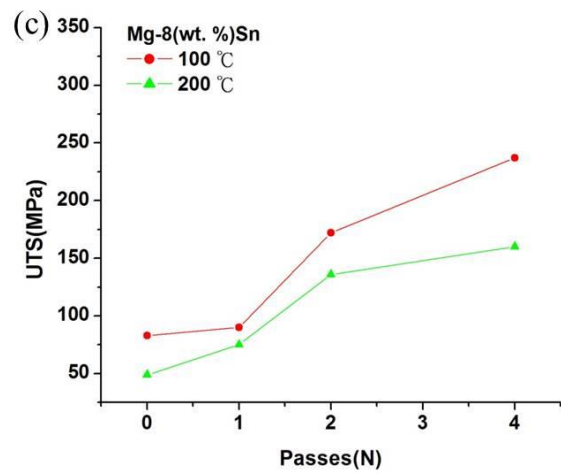
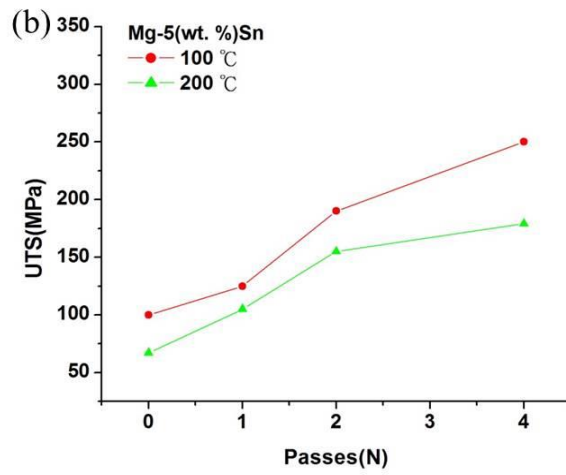
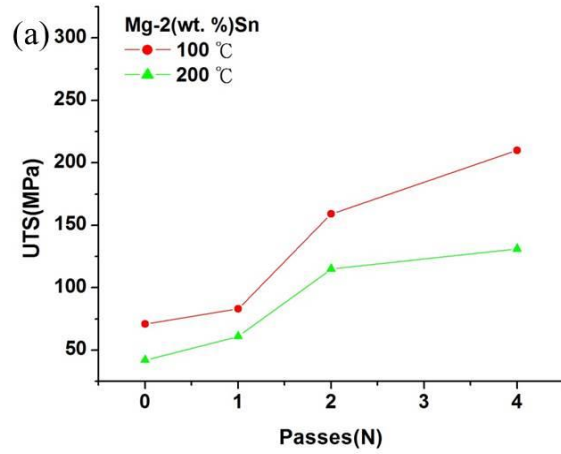


Table 5-1 Tensile properties of Mg-2, 5, 8(wt. %)Sn alloys after ECAE process.

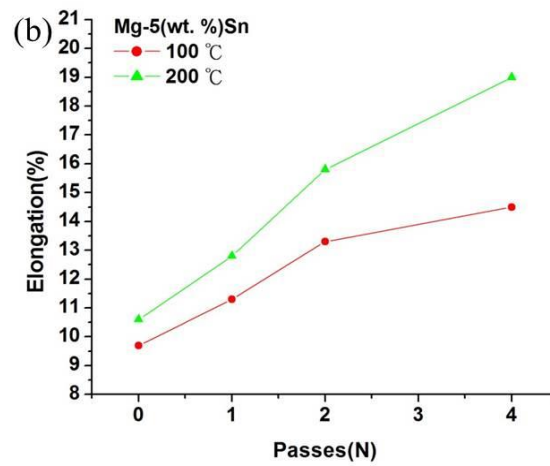
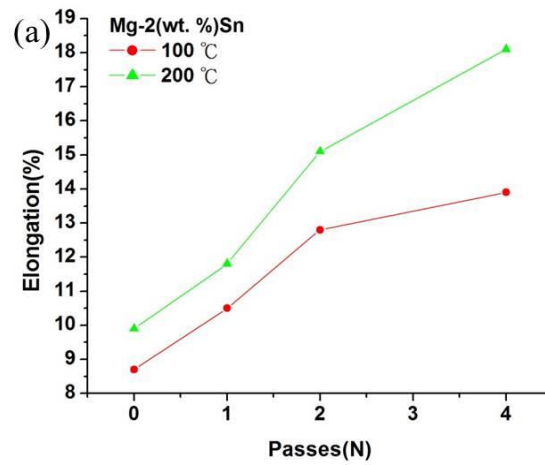
ECAE passes	YS (MPa) & UTS (MPa)												Elongations (%)					
	Mg-2Sn		Mg-5Sn				Mg-8Sn						Mg-2Sn		Mg-5Sn		Mg-8Sn	
	100°C	200°C	100°C	200°C	100°C	200°C	100°C	200°C	100°C	200°C	100°C	200°C	100°C	200°C	100°C	200°C		
N = 0	51	74	31	48	74	103	40	67	62	77	34	51	7.2	9.9	9.7	10.6	6.0	7.2
N = 1	56	81	39	60	90	125	62	104	68	85	49	76	10.5	11.8	11.2	12.6	7.8	9.0
N = 2	110	165	80	123	136	188	91	151	119	175	82	140	12.6	14.9	13.4	15.5	9.4	11.8
N = 4	149	220	86	131	176	248	108	179	161	230	96	152	13.7	18.1	14.5	18.9	10.5	15.5

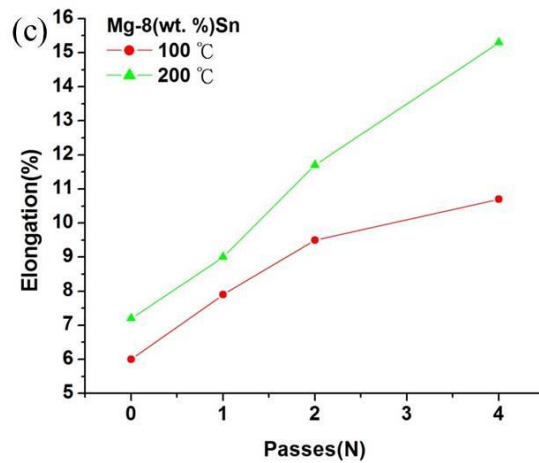


Figs. 5-1 Tensile strength at high temperatures 100 °C and 200 °C with different

ECAE passes: (a) Mg-2(wt. %)Sn, (b) Mg-5(wt. %)Sn and (c) Mg-8(wt.

%)Sn.



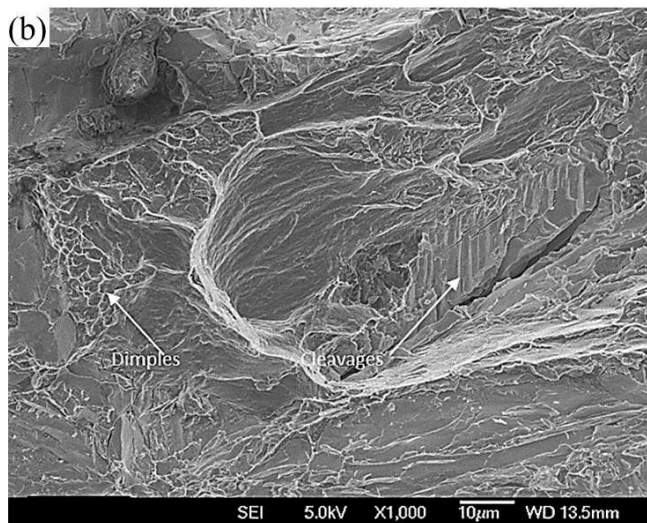
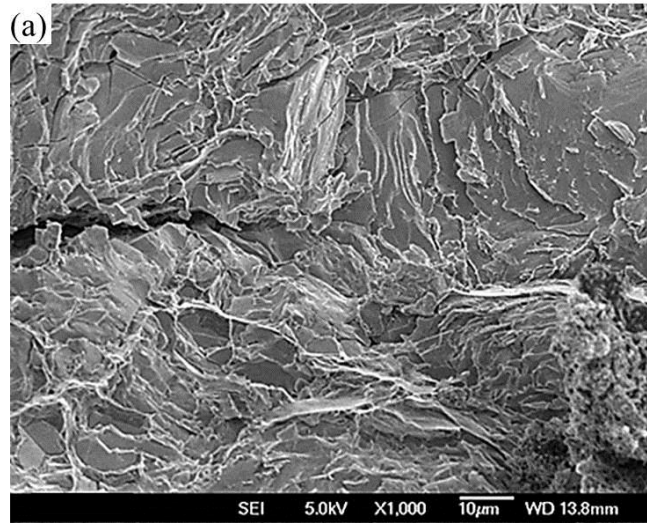


Figs. 5-2 Elongations at high temperatures 100 °C and 200 °C with different ECAE

passes: (a) Mg-2(wt. %)Sn, (b) Mg-5(wt. %)Sn and (c) Mg-8(wt. %)Sn.

5.2.2 Fracture surface observation

Figs. 5-3 exhibited the fracture surface of Mg-5(wt. %)Sn alloy after tensile test at high temperatures 100 °C and 200 °C. Fig. 5-3(a) showed the result at 100 °C, while this result was very similar to the room temperature; it means that the cleavage was still a major fracture mode. Fig. 5-3(b) demonstrated that the specimen was broken at 200 °C; by contrast, the result showed that the fracture surface has consisted of a few dimples and a large number of cleavages. It could be explained that the fracture mode of Mg-5(wt. %)Sn alloy during tensile test at high temperatures 100 °C and 200 °C was gradually transformed from the brittle mode to the plastic mode through thermal activation.



Figs. 5-3 Fracture surface of Mg-5(wt. %)Sn alloy after tensile test with a fixed strain rate $1 \times 10^{-3} \text{ s}^{-1}$: (a) test at 100 °C and (b) test at 200 °C.

5.3 Superplastic behavior evaluation

5.3.1 Microstructure observation and grain size distribution

Figs. 5-4(a) and (b) respectively exhibited the OM and SEM microstructures of the Mg-5(wt. %)Sn alloy after ECAE six passes. In Fig. 5-4(a) all the coarsening grains have been replaced by fine grains. The average grain size of the Mg-5(wt. %)Sn alloy the average grain size was further reduced from 147 μm (as-cast) to 10 μm after ECAE six passes. It means that more two ECAE passes at 200 °C contributed DRX production, while the DRX then produces equiaxed grains with a high concentration of high angle grain boundaries. This phenomenon was similar as Somjeet et al. report [84].

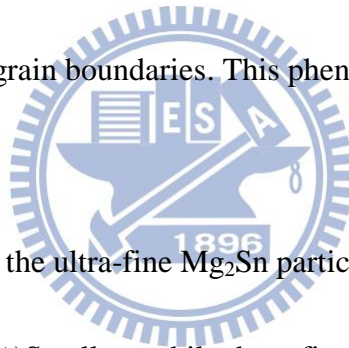
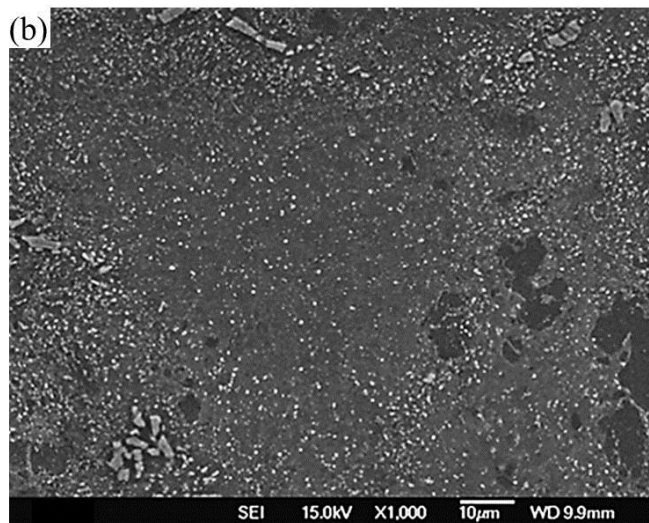
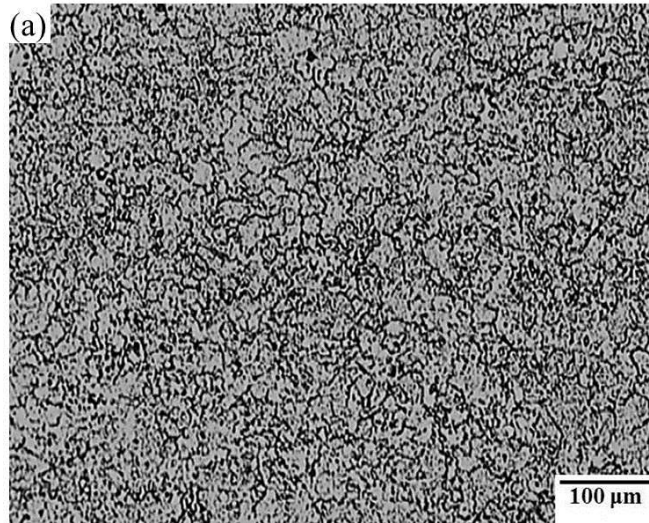


Fig. 5-4(b) showed that the ultra-fine Mg_2Sn particles were very uniformly distributed in the Mg-5(wt. %)Sn alloy, while these fine Mg_2Sn particles were formed by two reasons:

First of all, the continuous $\alpha\text{-Mg} + \text{Mg}_2\text{Sn}$ precipitates were completely broken down by ECAE six passes, while it could be distributed more uniform in the $\alpha\text{-Mg}$ matrix.

Secondly, the ultra-fine Mg_2Sn particles were directly produced by dynamic precipitation during the ECAE six passes.



Figs. 5-4 The microstructures of Mg-5(wt. %)Sn alloy after ECAE six passes: (a) OM image and (b) SEM image.

These Mg_2Sn particles were very helpful in restricting grain growth after ECAE six passes at 200 °C with a low extrusion rate (2 mm/min). Wei et al., Matsubara et al. and Miyahara et al. have reported similar results in their earlier studies [76, 84, 85]; the authors discovered that a large number of fine $Mg_{17}Al_{12}$ particles were directly formed via dynamic precipitation during extrusion, while these ultra-fine particles could inhibit grain boundary migration.

Fig. 5-5 showed a grain size distribution map of the Mg-5(wt. %)Sn alloy after ECAE six passes; the percentage of grains with an average size of 0-10 μm obviously risen from 57 % (four passes) to 83 % (six passes). This means that the microstructure of the Mg-5(wt. %)Sn alloy became a more homogeneous distribution.

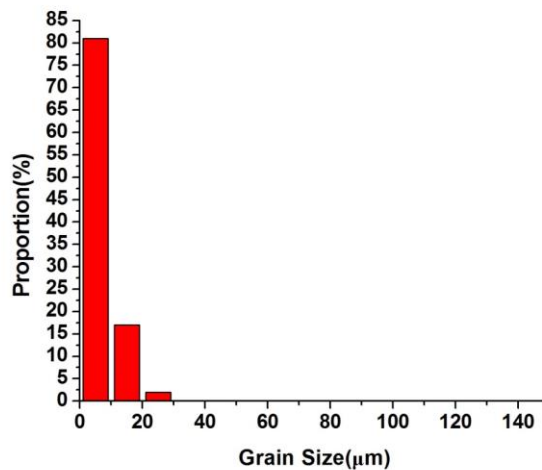


Fig. 5-5 Grain size distribution map of Mg-5(wt. %)Sn alloy after ECAE six passes.

5.3.2 Deformation at high temperatures

All the tensile elongations of the Mg-5(wt. %)Sn alloy that were subject to ECAE six passes as shown in Fig. 5-6(a). The results showed that superplasticity was achieved with the lowest strain rate ($1 \times 10^{-4} \text{ s}^{-1}$) at 250 °C, 300 °C and 350 °C.

The un-deformed and broken specimens were shown in Figs. 5-6(b)-(d). The maximum elongation reaches 550 % at 350 °C with a constant strain rate of $1 \times 10^{-3} \text{ s}^{-1}$; then the necking phenomenon could be observed in the Fig. 5-6(d). This phenomenon was very similar to the previous studies of Mg-based alloys [76, 86]; Matsubara et al. and Lin et al. observed that the necking was occurred when the tensile strain rates range from $1 \times 10^{-2} \text{ s}^{-1}$ to $1 \times 10^{-4} \text{ s}^{-1}$.

However, Fig. 5-6(a) showed that the elongation of 238 % at 350 °C with a strain rate of $1 \times 10^{-2} \text{ s}^{-1}$ was much lower than that of 550 % with a strain rate of $1 \times 10^{-3} \text{ s}^{-1}$ at the same temperature; this result could be explained that the grain boundary diffusion requires more time to cause an exchange between atoms and vacancies; thus the elongation of 238 % with the highest strain rate of $1 \times 10^{-2} \text{ s}^{-1}$ did not have enough time to allow for diffusion in the grain boundary. In contrast, the elongation of 365 %, which was observed at the lowest strain rate of $1 \times 10^{-4} \text{ s}^{-1}$ at the same temperature of 350 °C, was much lower than that of 550 % seen with a strain rate of $1 \times 10^{-3} \text{ s}^{-1}$ at 350 °C. As shown in Table 5-2, the average grain size

markedly increased from 10 μm to 42 μm after the tensile test with the strain rate of $1 \times 10^{-4} \text{ s}^{-1}$ at 350 $^{\circ}\text{C}$; it means that the opportunity for grain boundary sliding decreased with increasing average grain size during the tensile test; this phenomenon could explain that the elongation of 365 % was much lower than that of 550 % at the same temperature 350 $^{\circ}\text{C}$. In addition to the strain rates of $1 \times 10^{-2} \text{ s}^{-1}$ and $1 \times 10^{-3} \text{ s}^{-1}$, which decreased the opportunity for grain growth, the Mg_2Sn precipitates also played an important role in resisting grain growth during the tensile test. Therefore, the stability of grains was maintained up to 300 $^{\circ}\text{C}$ during the tensile tests. However, the Mg_2Sn precipitates were no longer able to restrain grain boundary migration at 350 $^{\circ}\text{C}$ with the lowest strain rate of $1 \times 10^{-4} \text{ s}^{-1}$.

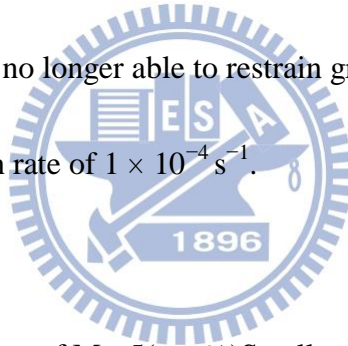
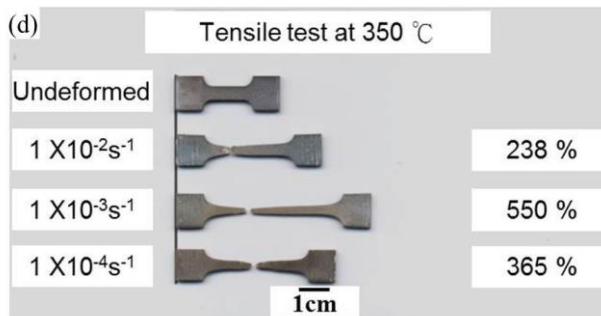
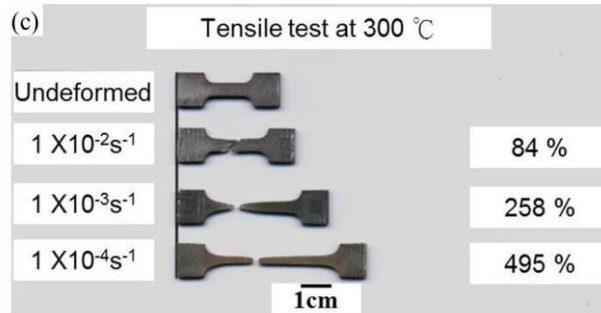
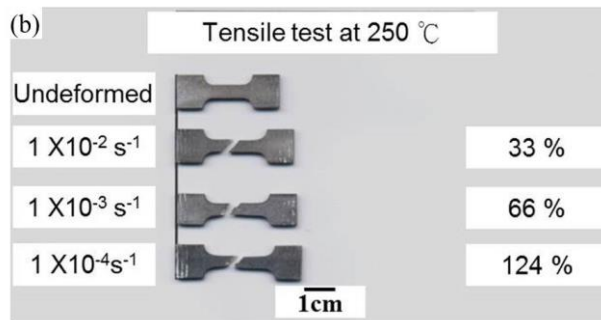
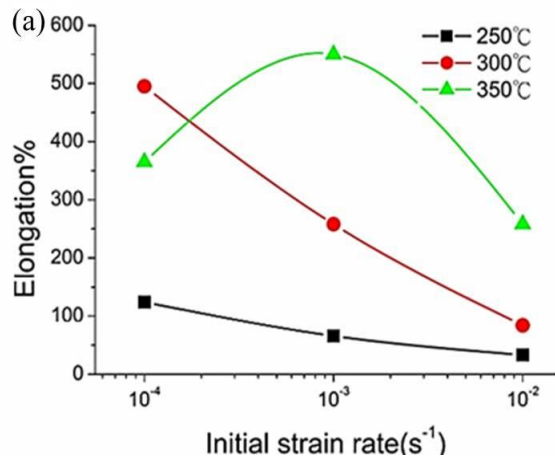


Table 5-2 Average grain size of Mg-5(wt. %)Sn alloy before & after tensile test at different temperatures and strain rates.

Before tensile test (6 ECAE passes)	Tensile test temperatures	Tensile test strain rates		
		$1 \times 10^{-2} \text{ s}^{-1}$	$1 \times 10^{-3} \text{ s}^{-1}$	$1 \times 10^{-4} \text{ s}^{-1}$
10.0 μm	250 $^{\circ}\text{C}$	10.6 μm	11.2 μm	12.6 μm
	300 $^{\circ}\text{C}$	11.5 μm	12.8 μm	17.8 μm
	350 $^{\circ}\text{C}$	13.0 μm	14.3 μm	42.0 μm



Figs. 5-6 Tensile results of Mg-5(wt. %)Sn alloy: (a) elongation obtained at different strain rates and temperatures, (b) test specimens at 250 °C, (c) test specimens at 300 °C and (d) test specimens at 350 °C.

5.3.3 Deformation mechanism

Fig. 5-7(a) showed the flow stress versus strain rate curve at different temperatures obtained from the strain rate step tests. To understand the mechanism during the superplastic process, the activation energy (Q) was calculated at constant strain rate by using the following equation as shown in (5-1) [87]:

$$Q = nR [\partial (\ln \sigma) / \partial (1/T)] \quad (5-1)$$

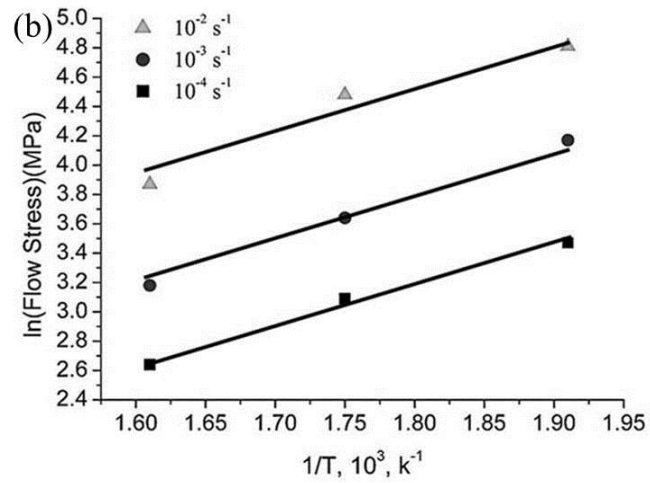
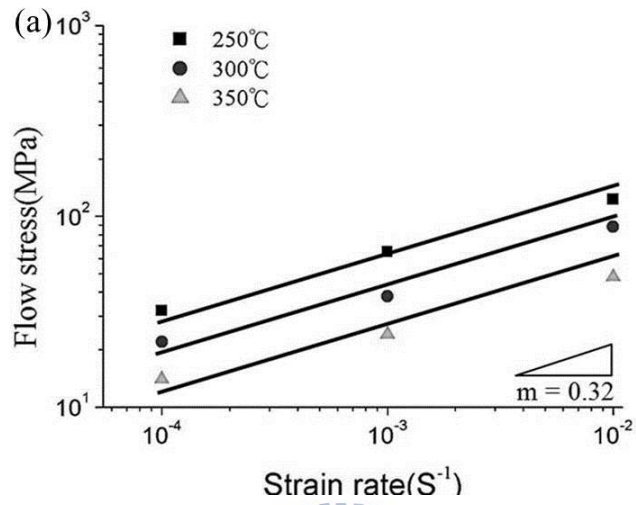
where σ was the flow stress; n was the stress exponent ($n = 1/m$); R and T were respectively the gas constant and temperature.

The mean strain rate sensitivity (m value) of 0.32 was obtained from the slope of the curve in Fig. 5-7(a); then $\partial (\ln \sigma) / \partial (1/T)$ was estimated from the slope of the curve in Fig. 5-7(b); thus, the activation energy was determined to be 98.7 kJ mol⁻¹.

Noteworthy, Park et al. investigated that the m value at low strain rate range of Mg-8Sn-1Al-1Zn alloy was 0.37; then the superplastic deformation mechanism of this alloy was controlled by Grain Boundary Sliding (GBS) and Grain Matrix Slip deformation (GMD) [35]. The m value (0.32) of this section was so close to the m value (0.37) of Park et al. reporting, that the mechanism of superplasticity in this section was mainly controlled by the GBS + GMD at 250 °C, 300 °C. By contrast, the major deformation mechanism at 350 °C may transfer gradually from GBS + GMD ($1 \times 10^{-2} \text{ s}^{-1}$ and $1 \times 10^{-3} \text{ s}^{-1}$) to GMD ($1 \times 10^{-4} \text{ s}^{-1}$). Table 5-2 showed that the average

grain size obviously grew from 10 μm to 42 μm at high temperature 350 $^{\circ}\text{C}$ with a fixed strain rate $1 \times 10^{-4} \text{ s}^{-1}$. It was well known that grain refinement and resisting grain growth was beneficial for high temperature plasticity, which was due to the activation of GBS; however, grain coarsening was performed by high temperatures or low strain rates [88]. Furthermore, the deformation mechanism of GBS and GMD competed against each other at high temperatures [35]. Therefore, grain coarsening could reduce the opportunity of GBS; thus, the GMD became a key role to control the deformation mechanism during tensile test at high temperature 350 $^{\circ}\text{C}$ with the lowest strain rate $1 \times 10^{-4} \text{ s}^{-1}$.

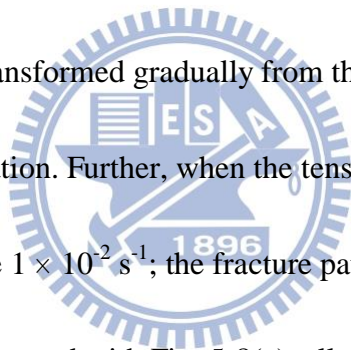
Further, the active energy (Q) of 98.7 kJ mol^{-1} was calculated in this section; this value was higher than grain boundary diffusion (95 kJ mol^{-1}), but much lower than lattice self-diffusion (135 kJ mol^{-1}) of magnesium alloy [89, 90]. It means that the grain boundary diffusion may dominate the superplastic deformation mechanism during whole tensile test at high temperatures.

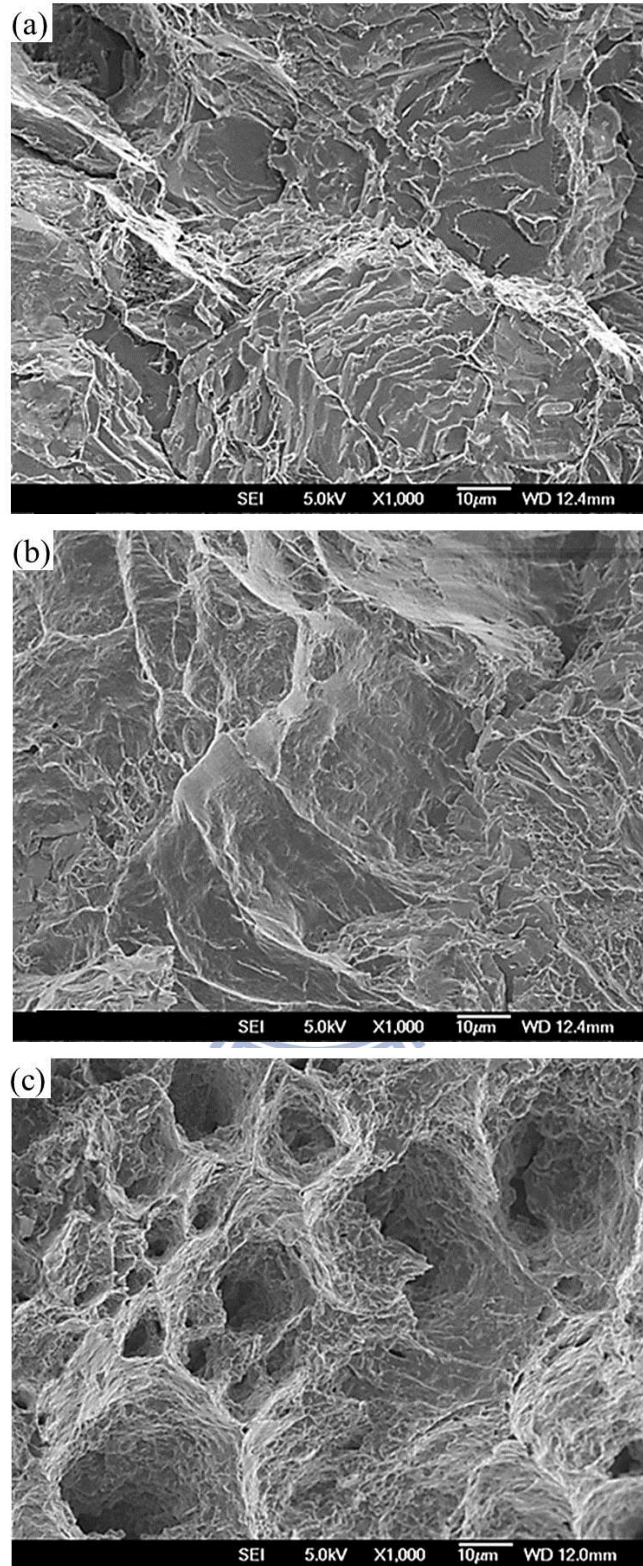


Figs. 5-7 (a) the m value of different temperatures and (b) flow stress versus different temperatures curves.

5.3.4 Fracture surface observation

The failure of magnesium alloy was usually brittle through cleavage with a H.C.P structure [83]. Figs. 5-8 showed SEM image of the tensile fracture surface. Fig. 5-8(a) was a fracture surface of specimen after ECAE six passes, which conduct tensile test with strain rate $1 \times 10^{-2} \text{ s}^{-1}$ at 250 °C; the result showed that the major fracture surface was composed of cleavage. Fig. 5-8(b) showed that the specimen was broken at 300 °C with the same strain rate; the result showed that the main fracture surface consisted dimples and cleavages, while this means that the deformation of Mg-5(wt. %)Sn alloy was transformed gradually from the brittle mode to the plastic mode through thermal activation. Further, when the tensile test temperature increased to the 350 °C with strain rate $1 \times 10^{-2} \text{ s}^{-1}$; the fracture pattern changed to the dimples as shown in Fig. 5-8(c). Compared with Fig. 5-8(a), all the cleavages disappeared very obviously, and the major patterns were replaced by dimples.





Figs. 5-8 SEM images of fracture surface after tensile test with strain rate 1×10^{-2} s^{-1} at different temperatures (a) 250 °C, (b) 300 °C and (c) 350 °C.

5.4 Summary

This chapter detail investigated the high temperature tensile properties including high temperature strength and superplastic deformation of Mg-5(wt. %)Sn alloy. In high temperature strength after ECAE four passes, the YS and UTS had a similar trend; the UTS increased from 67 MPa to 179 MPa at 200 °C, and the elongation increased from 10.6 % to 18.9 % at 200 °C. The fracture surface was cleavage at 100°C with a fixed strain rate $1 \times 10^{-3} \text{ s}^{-1}$, and the fracture surface found the few dimples at 200 °C.

On the other hand, the grain size of Mg-5(wt. %)Sn alloy was successfully reduced from 147 μm (as-cast) to 10 μm by ECAE six passes, while the microstructure of this alloy after ECAE six passes was homogeneous fine grains and Mg_2Sn precipitates. There was no obvious grain growth at 350 °C after tensile tests with strain rates 1×10^{-2} and 10^{-3} s^{-1} ; however, the grain growth could be found at 350 °C with a strain rate $1 \times 10^{-3} \text{ s}^{-1}$, while the average grain size increases from 10 μm to 42 μm . The maximum elongation was conducted at 350 °C with a strain rate of $1 \times 10^{-3} \text{ s}^{-1}$; the elongation could reach 550 %. Then the superplastic behavior of Mg-5(wt. %)Sn alloy was mainly controlled by GBS + GMD. However, the deformation mechanism at 350 °C with the lowest strain rate $1 \times 10^{-4} \text{ s}^{-1}$ could change to the GMD.

Further, the activation energy (Q) was calculated to be 98.7 kJ mol^{-1} , while the grain boundary diffusion might dominate the superplastic deformation mechanism during whole tensile test. The fracture surface was cleavage at $250 \text{ }^\circ\text{C}$ with strain rate $1 \times 10^{-2} \text{ s}^{-1}$ and the fracture surface replaced by the dimples was transformed gradually from the brittleness to the plasticity at $350 \text{ }^\circ\text{C}$.



CHAPTER 6 SHT + ECAE PROCESS ENHANCING

MECHANICAL PROPERTIES AT HIGH TEMPERATURES

6.1 Motivation

The Mg-5(wt. %)Sn alloy has been proved that the alloy had the best tensile strength at room and high temperatures. However, the Mg₂Sn particles, which have been broken down by ECAE process, were stillly observed some coarsening Mg₂Sn particles after ECAE four passes, while these coarsening Mg₂Sn particles might be an not completely breaking α -Mg + Mg₂Sn continuous precipitates. By contrast, Solution Heat Treatment (SHT) + aging treatment were an effect method to refine and redistribute precipitates. Therefore, this chapter would use the SHT + ECAE two steps process to refine the Mg₂Sn particles; then expecting the tensile strength of Mg-Sn alloys could further promote by these refining Mg₂Sn particles.

6.2 Microstructure observation and grain size distribution

6.2.1 States after SHT

The microstructure of Mg-5(wt. %)Sn alloy after an SHT process at 480 °C for 22 hours was shown in Fig. 6-1. The grain boundary was clean; it means that the segregation and the continuous eutectic α -Mg + Mg₂Sn precipitates were dissolved in the α -Mg matrix after SHT and water quenching.

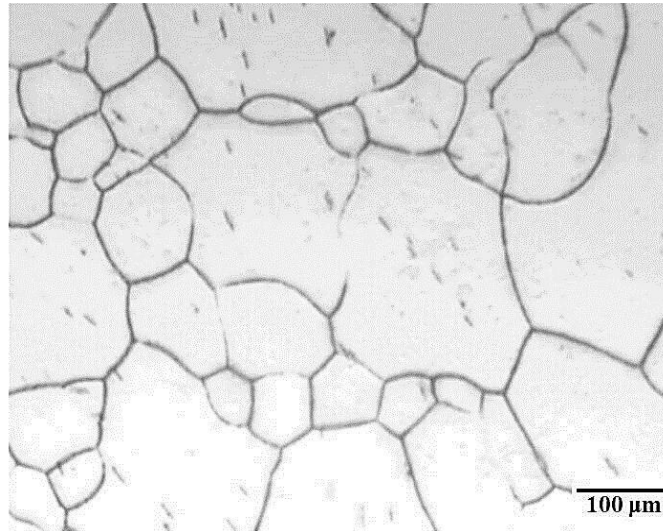


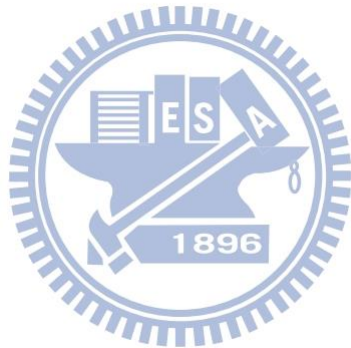
Fig. 6-1 OM image of Mg-5(wt. %)Sn alloy after SHT at 480 °C for 22 hours.

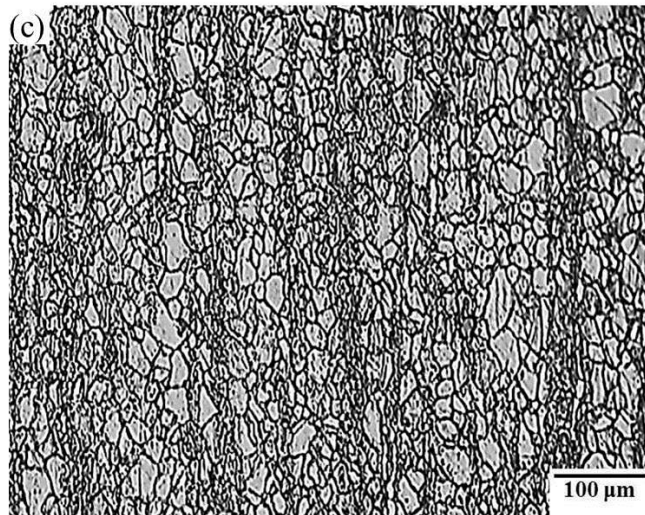
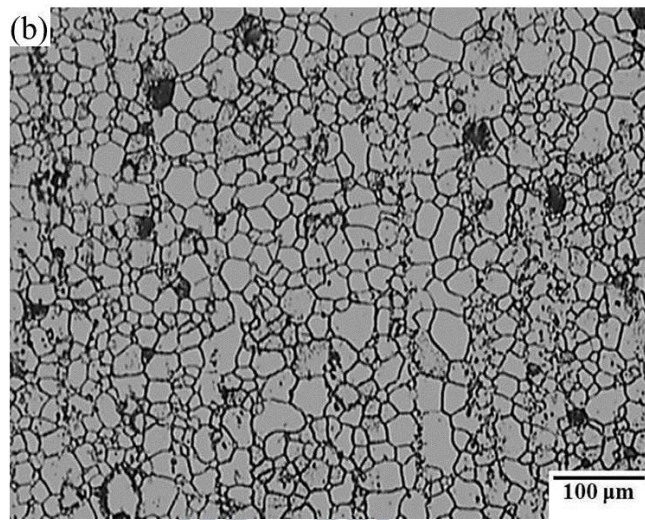
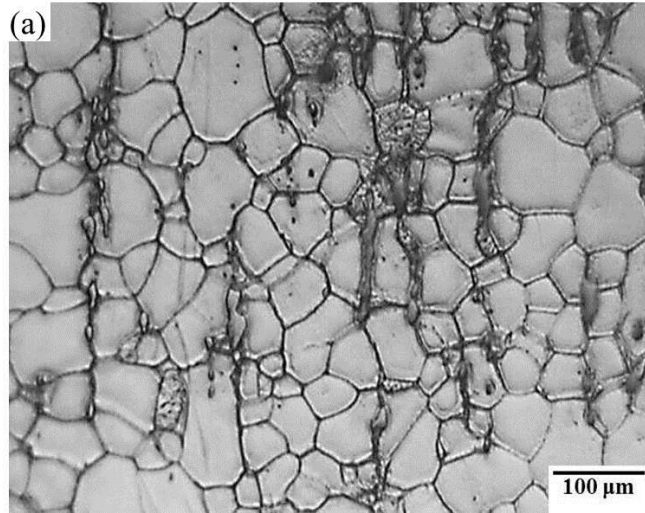
6.2.2 Microstructures after ECAE process state

Figs. 6-2(a)-(c) demonstrated the OM images of the Mg-5(wt. %)Sn alloy after SHT + ECAE one, two and four passes. The microstructures distribution were homogeneous; the average grain size decreased with increasing ECAE passes from 147 μm (as-cast) to 16 μm (SHT + ECAE four passes).

Figs. 6-3(a)-(c) showed the SEM images of the alloy after SHT + ECAE one, two and four passes. Fig. 6-3(a) exhibited that the fine and discontinuous Mg₂Sn particles were precipitated through the dynamic precipitation during ECAE one pass. Further, the fine Mg₂Sn particles, which distributed more uniformly, were observed after ECAE two and four passes, as shown in Figs. 6-3(b) and (c). These results mean that the coarsening α-Mg + Mg₂Sn precipitates were significantly dissolved in the

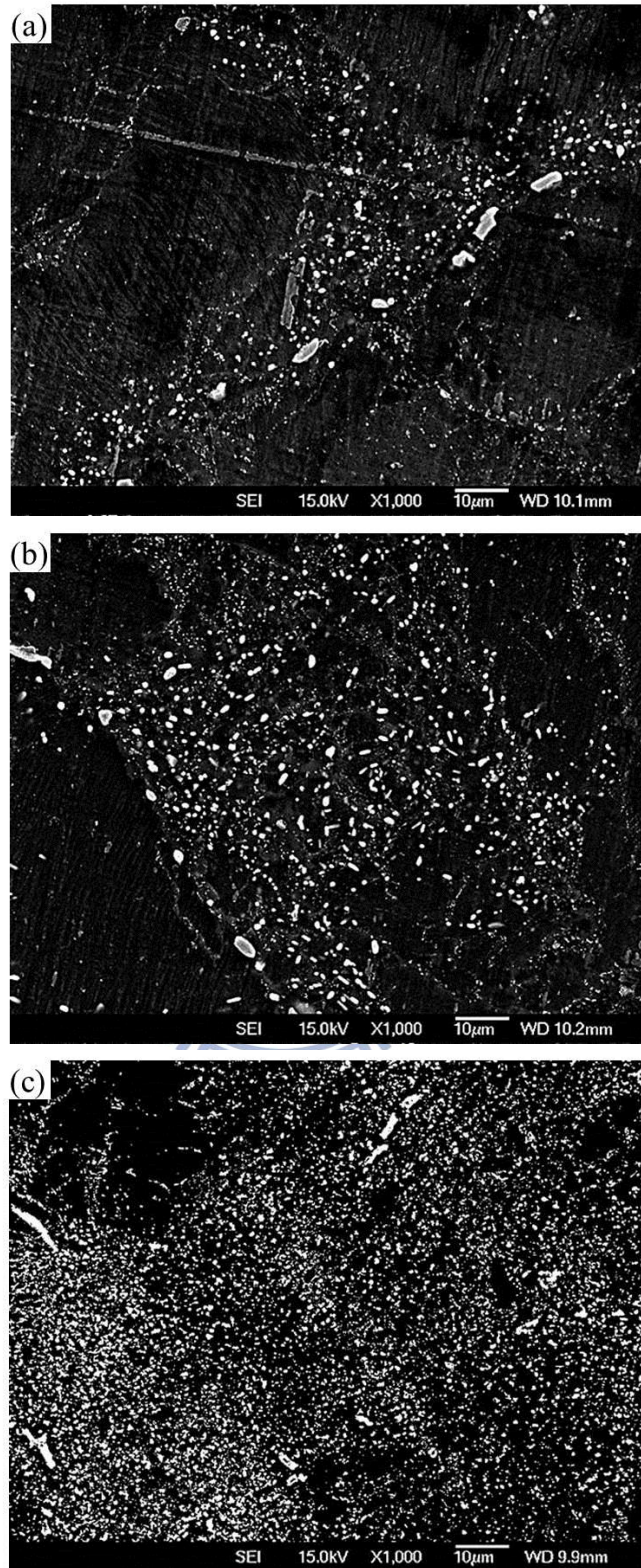
α -Mg matrix after an SHT process; then these fine and uniform Mg_2Sn particles were redistributed by dynamic precipitating during ECAE process at 200 °C. Further comparing the results of ECAE four passes none SHT in the chapter 4, those results showed that the Mg_2Sn particles still maintained some coarsening shape. Therefore, the Mg_2Sn particles, which produced by SHT + ECAE two steps process were smaller than that produced by breaking coarsening α -Mg + Mg_2Sn precipitates none SHT.





Figs. 6-2 OM images of Mg-5(wt. %)Sn alloy after SHT + ECAE process:

(a) N = 1, (b) N = 2 and (c) N = 4.



Figs. 6-3 SEM images of Mg-5(wt. %)Sn alloy after SHT + ECAE process:

(a) N = 1, (b) N = 2 and (c) N = 4.

6.2.3 Grain size distribution

Table 6-1 showed the average grain size of the Mg-5(wt. %)Sn alloy with or none SHT after ECAE one, two and four passes. It was clear that the average grain size of the alloy decreased with increasing ECAE passes. There were two reasons for the decreasing in the average grain size.

First of all, the thermal energy and shear strain energy were helpful for the dynamic recrystallization (DRX); therefore, the DRX led to the production of fine grains. Secondly, the as-SHT Mg-5(wt. %)Sn alloy could dynamically precipitate a large number of Mg₂Sn particles in the grain boundaries during the ECAE process at high temperature 200 °C; then these particles could retard grain boundary migration. Therefore, the average grain size of the Mg-5(wt. %)Sn alloy with SHT was smaller than that of the same alloy none SHT.

Similarly, Park et al. reported in their early study [35]; the authors indicated that the thermally stable uniform precipitates at the grain boundaries inhibited grain growth during high temperature deformation.

Table 6-1 Average grain size of Mg-5(wt. %)Sn alloy.

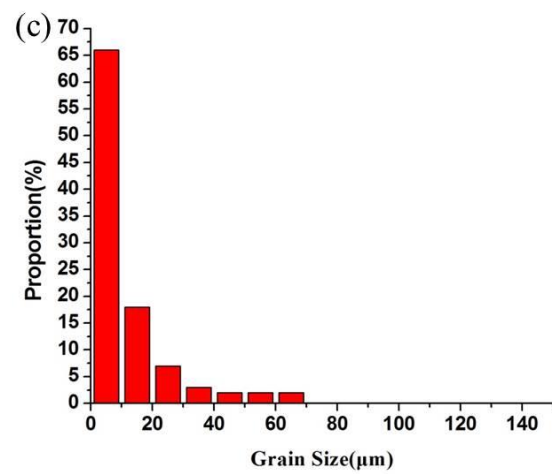
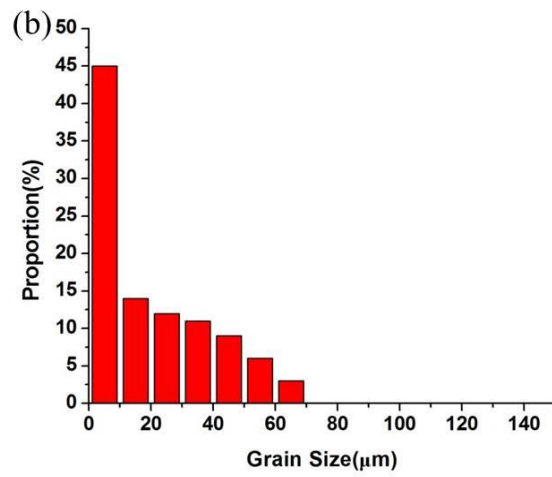
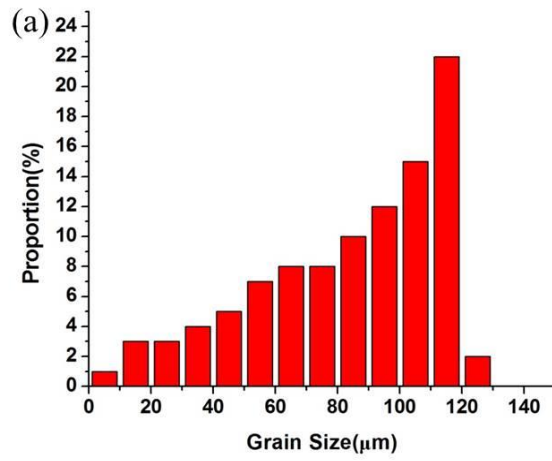
As-cast	ECAE passes	ECAE none SHTed	ECAE after SHTed
147.0 μm	N = 1	87.5 μm	48.4 μm
	N = 2	69.7 μm	20.3 μm
	N = 4	28.0 μm	16.0 μm

Figs. 6-4(a)-(c) demonstrated the maps of grain size distribution, while these maps were the Mg-5(wt. %)Sn alloy after ECAE one, two and four passes with SHT. These maps showed that the percentage of average grain size (0-10 μm) reached from 3 % to 66 %, while this value was obviously higher than the value 54 % of Mg-5(wt. %)Sn alloy non SHT. These results further proved that the fine and uniform distribution Mg_2Sn particles, which were formed by SHT + ECAE two-step process, could obviously promote the effect of grain refining.

Comparing section 4.3.2, the Mg-5(wt. %)Sn alloy none SHT after ECAE one and two passes were obviously found dual-peaks in the maps; however, this section has not found any bi-modal distribution in the microstructure of the Mg-5(wt. %)Sn alloy with SHT after ECAE one and two passes; this result might cause by fowling reason:

The SHT process produced a non-stable state structure, which contained a huge amount of solution tin atoms, while these atoms further induced many micro stress fields in the structure. Therefore, the new grains would uniformly form in these pre-existing micro stress fields during ECAE process at high temperature 200 $^{\circ}\text{C}$.

Park et al. have observed a similar result in their early reports [41].



Figs. 6-4 Grain size distribution maps (a) N =1 after SHT, (b) N =2 after SHT and (c) N = 4 after SHT.

6.3 Tensile test at room and high temperatures

Table 6-2 detail showed the tensile test results of the Mg-5(wt. %)Sn alloy including as-cast, ECAE four passes none SHT, as-SHT and ECAE four passes after SHT. The YS and UTS of as-SHT condition were better than that of as-cast, but much poorer than that of SHT + ECAE four passes and ECAE four passes none SHT conditions. Although the strength of the alloy slightly increased by solid solution strengthening, the gains still maintained coarsening after SHT, while the average grain size after SHT was 161 μm .

Further, all the YS and UTS values increased after ECAE four passes at room temperature and high temperatures (100 °C and 200 °C). However, all the YS and UTS values of the Mg-5(wt. %)Sn alloy after SHT + ECAE four passes were larger than these of the alloy after ECAE four passes none SHT. For example, The UTS of the alloy after SHT + ECAE four passes significantly increased from 126 MPa to 360 MPa at room temperature, but the UTS of the alloy after ECAE four passes none SHT increased from 126 MPa to 327 MPa at room temperature. There were two reasons induced this phenomenon.

First of all, the average grain size of the alloy after SHT + ECAE four passes were smaller than that of the alloy after ECAE four passes none SHT as shown in Table 6-1.

Secondly, more fine and uniform Mg₂Sn particles were redistributed by SHT + ECAE two-step process as shown in Fig. 6-3(c).

Moreover, the elongations of the Mg-5(wt. %)Sn alloy including as-cast, ECAE four passes none SHT, as-SHT and ECAE four passes after SHT were also shown in Table 6-2. All the elongations of the alloy after SHT + ECAE four passes, and after ECAE four passes none SHT displayed a similar trend. However, all the elongations of the alloy after SHT + ECAE four passes were larger than those of the alloy after ECAE four passes none SHT. For example, the elongation of the alloy after ECAE four passes none SHT only increased from 7.9 % to 9.5 % at room temperature, but the elongation of the alloy after SHT + ECAE four passes obviously increased from 7.9 % to 11.3 % at room temperature. Table 6-1 showed the evidence to support these results; the average grain size of the alloy after SHT + ECAE four passes (16 μm) was smaller than that of the alloy after ECAE four passes none SHT (28 μm); it means that more high degree of grain refining still played an important role to enhance the elongations of the alloy after SHT + ECAE four passes at room and high temperatures (100 °C and 200 °C).

From the above, only SHT process could increase in limit the YS and UTS at room and high temperatures (100 °C and 200 °C), but it was not enough to effectively promote the YS, UTS and elongations at the same time. By contrast, the SHT +

ECAE two-step process were very helpful to enhance the strength and elongation of Mg-5(wt. %)Sn alloy at room and high temperatures (100 °C and 200 °C) because the ECAE process still played a key factor to obviously increase the strength and elongations by grain refining and precipitates uniformly distribution.

Table 6-2 Tensile properties of Mg-5(wt. %)Sn alloy after four ECAE passes.

Samples	YS (MPa)	UTS (MPa)	Elongations (%)
as-cast			
R.T	104	126	7.9
100°C	74	103	9.7
200°C	40	67	10.6
as-SHT			
R.T	142	175	4.3
100°C	106	134	6.2
200°C	76	99	7.1
N=4 none SHTed			
R.T	270	327	9.5
100°C	176	248	14.5
200°C	108	179	18.9
N=4 after SHTed			
R.T	302	360	11.3
100°C	232	281	16.8
200°C	173	209	22.1

6.4 Fracture surface observation

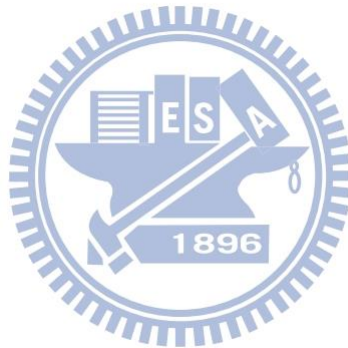
It was well known that a magnesium alloy failed in a brittle mode through cleavage or quasi-cleavage with an HCP structure at room temperature [83].

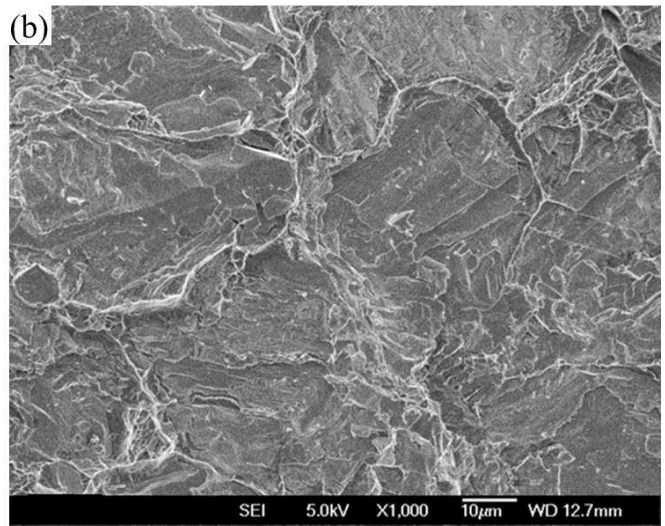
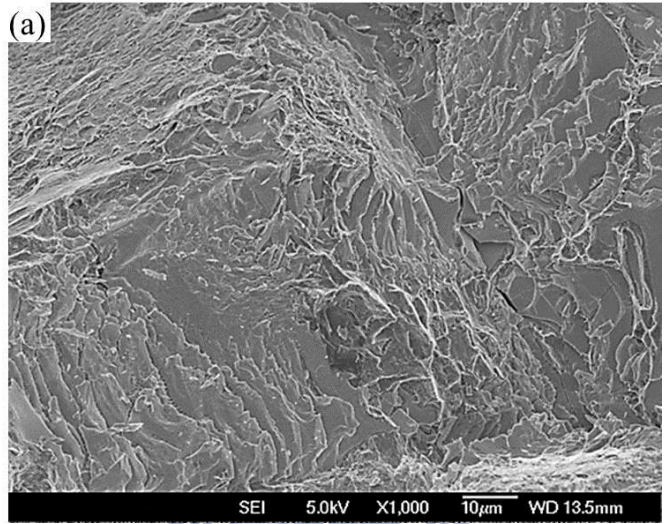
Figs. 6-5(a)-(c) were the fracture surfaces of Mg-5(wt. %)Sn alloy samples after SHT + ECAE four passes. Fig. 6-5(a) showed that the fractures were due to the cleavage at room temperature, and that several cleavages were presented. Fig. 6-5(b) exhibited the result at 100 °C, which was similar to that at room temperature; the cleavage was the major fracture mode. Fig. 6-5(c) demonstrated that the specimen broken at 200 °C.

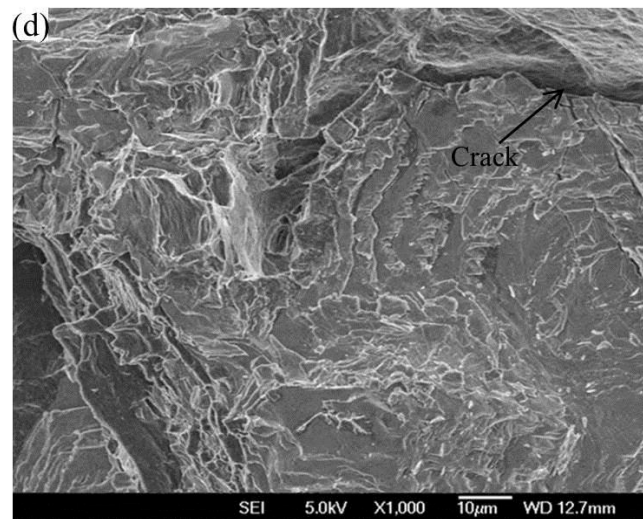
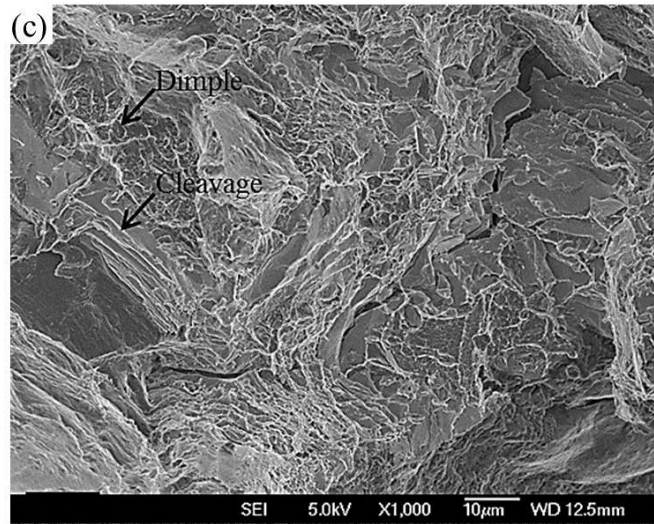
The result showed that the fracture surface consisted of dimples and cleavages; it means that the process of SHT + ECAE four passes could improve the plastic deformation of the Mg-5(wt. %)Sn alloy; thus, the fracture mode of the alloy gradually transformed from the brittle to the ductile through thermal thermo activation.

This section further compared the fracture surface, which broken at high temperature 200 °C between as-cast and SHT + ECAE four passes conditions of Mg-5(wt. %)Sn alloy. Fig. 6-5(d) showed the fracture surface of as-cast condition, while the major fracture mode was cleavage, and a huge crack was observed. By contrast, although a small crack was observed in the fracture surface of SHT + ECAE four passes condition as shown in Fig. 6-5(c), this crack was very smaller than that of

as-cast condition; This means that the coarse eutectic α -Mg + Mg₂Sn precipitates obviously induced the crack initializing and growing; then using SHT + ECAE two-step process could reduce this phenomenon by redistributing fine Mg₂Sn particles. Feng et al. have reported a similar result [91]; the authors found that the cracks of AZ91D magnesium alloy were increased by coarse eutectic Mg₁₇Al₁₂ phase during tensile test; then using Friction Stir Process (FSP) + aging treatment two-step method could decrease the cracks by dissolving and refining the coarse eutectic Mg₁₇Al₁₂ phase.







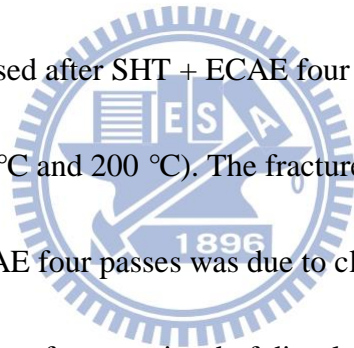
Figs. 6-5 Fracture surface after tensile test with a constant strain rate $1 \times 10^{-3} \text{ s}^{-1}$

(a) $N = 4$ after SHT broken at RT, (b) $N = 4$ after SHT broken at $100 \text{ }^\circ\text{C}$,

(c) $N = 4$ after SHT broken at $200 \text{ }^\circ\text{C}$ and (d) as-cast broken at $200 \text{ }^\circ\text{C}$.

6.5 Summary

From above all of chapter 6, the continuous eutectic α -Mg + Mg₂Sn precipitates were not observed in the Mg-5(wt. %)Sn alloy, while the grain boundary was clean after SHT. Moreover, the ECAE process was helpful for grain refining; then the average grain size decreased with increasing ECAE passes from 147 μ m (as-cast) to 16 μ m (SHT + ECAE four passes). Beside grain refinement, the fine and uniform Mg₂Sn particles of the as-SHT Mg-5(wt. %)Sn alloy were produced by dynamic precipitation during ECAE process. On the other hand, the YS and UTS of the Mg-5(wt. %)Sn alloy increased after SHT + ECAE four passes at room temperature and high temperatures (100 °C and 200 °C). The fracture surface of the Mg-5(wt. %)Sn alloy after SHT + ECAE four passes was due to cleavage at room temperature and 100 °C, and the fracture surface consisted of dimples and cleavages at 200 °C.



CHAPTER 7 CONCLUSIONS

7.1 Microstructures of Mg-Sn alloys

1. Adding tin in the Magnesium alloy was helpful for grain refinement; the average grain size decreased from 296 μm (Mg-2 wt. %Sn) to 147 μm (Mg-5 wt. %Sn); finally, the average grain size obviously decreased to 106 μm (Mg-8 wt. %Sn).
2. The continuous eutectic $\alpha\text{-Mg} + \text{Mg}_2\text{Sn}$ precipitates increased with increasing tin content.
3. The Mg-2, 5, 8(wt. %)Sn alloys produced large amounts of fine grains after ECAE four passes, while the minimal percentage of average grain size (0-10 μm) was more than 35 %.
4. The microstructures distribution of Mg-2, 5, 8(wt. %)Sn alloys were a bi-modal distribution after ECAE one and two passes. However, this phenomenon could not be observed after SHT + ECAE two steps process.
5. The grain size of Mg-5(wt. %)Sn alloy was reduced from 147 μm (as-cast) to about 10 μm by ECAE six passes.
6. The microstructure of Mg-5(wt. %)Sn alloy after ECAE six passes was homogeneous fine grains and ultra-fine Mg_2Sn precipitates.

7. There was no obvious grain growth at 350 °C after tensile test with strain rate 1×10^{-2} and 10^{-3} s^{-1} . However, the grain growth could be found at 350 °C with strain rate $1 \times 10^{-4} \text{ s}^{-1}$, the average grain size increases from 10 μm to 42 μm .
8. The continuous eutectic $\alpha\text{-Mg} + \text{Mg}_2\text{Sn}$ precipitates of Mg-5(wt. %)Sn alloy were dissolved in the $\alpha\text{-Mg}$ matrix after SHT, while the grain boundary was clean.
9. The ECAE process was helpful for grain refining; the average grain size decreased with increasing ECAE passes from 147 μm (as-cast) to 16 μm (SHT + ECAE four passes).
10. The ultra-fine and uniform Mg_2Sn particles of the as-SHT Mg-5(wt. %)Sn alloy were produced by dynamic precipitation during ECAE process.

7.2 Tensile properties of Mg-Sn alloys

1. Mg-5(wt. %)Sn alloy had the best tensile properties after ECAE four passes. The YS and UTS had a similar trend; the UTS reached 328 MPa at room temperature, and the elongation still retained about 9.6 %. Moreover, the UTS increased from 67 MPa to 179 MPa at 200 °C, as well as the elongation increased from 10.6 % to 18.9 % at 200 °C.
2. The maximum elongation of Mg-5(wt. %)Sn alloy was conducted at 350 °C with a strain rate of $1 \times 10^{-3} \text{ s}^{-1}$; the elongation could reach 550 %.

3. The superplastic behavior of Mg-5(wt. %)Sn alloy was mainly controlled by GBS + GMD. However, the deformation mechanism at 350 °C with the lowest strain rate $1 \times 10^{-4} \text{ s}^{-1}$ could change to the GMD.
4. The activation energy (Q) was calculated to be 98.7 kJ mol⁻¹. The grain boundary diffusion dominated the superplastic deformation mechanism during tensile test
5. The YS and UTS of the Mg-5(wt. %)Sn alloy obviously increased after SHT + ECAE four passes at room temperature and high temperatures 100 °C and 200 °C.

7.3 Fracture surface of Mg-Sn alloys

1. The fracture surface of Mg-5(wt. %)Sn alloy, which processed by ECAE four passes, was cleavage at RT and 100 °C with strain rate of $1 \times 10^{-3} \text{ s}^{-1}$, but the fracture surface found the few dimples at 200 °C.
2. The fracture surface of Mg-5(wt. %)Sn alloy, which processed by ECAE six passes, was cleavage at 250 °C with strain rate of $1 \times 10^{-2} \text{ s}^{-1}$. However, the fracture surface replaced by the dimples was transformed gradually from the brittleness to the plasticity at 350 °C.
3. The fracture surface of the Mg-5(wt. %)Sn alloy after SHT + ECAE four passes was due to cleavage at room temperature and high temperature 100 °C, while the fracture surface consisted of dimples and cleavages at high temperature 200 °C.

CHAPTER 8 FUTURE WORK

The present study successfully enhanced the tensile properties of Mg-Sn alloys at room and high temperatures by using ECAE or SHT + EACE two steps process, and carefully investigated the relationship between microstructures and tensile properties. However, there were some works should be studied in the future.

First of all, although the crystal structures of as-cast Mg-Sn alloys were investigated by using TEM analysis from early reports, there were too many crystal structures of wrought Mg-Sn alloys to study by authors. Therefore, this direction of research still has prodigious potential in the future works.

Secondly, the texture evolution of Mg-Sn alloys between ECAE pass and pass was very important. However, these studies seemed very rare in the Mg-Sn alloys domain; therefore, this field may become a critical work in the future.

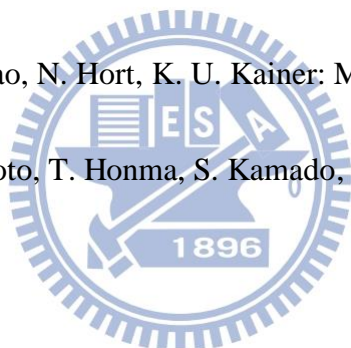
Thirdly, although this study evaluated the superplastic forming of Mg-5(wt. %)Sn alloy by using ECAE six passes, as well as enhanced the tensile strength of this alloy at high temperatures by using SHT + ECAE two steps process. However, the superplastic forming of Mg-5(wt. %)Sn alloy by using SHT + ECAE process was not studied in this work. Therefore, this issue may have an opportunity to perform better superplastic deformation of Mg-5(wt. %)Sn alloy in the future.

REFERENCE

1. Y. Kojima: Mater. Trans. **42**, 1154 (2001).
2. S. E. Ion, F. J. Humphreys, S. H. White: Acta Metall. **30**, 1909 (1982).
3. S. R. Agnew, J. A. Horton, T. M. Lillo, D. W. Brown: Scripta Mater. **50**, 377 (2004).
4. C. J. Neil, S. R. Agnew: Int. J. Plasticity **25**, 379 (2009).
5. T. Hama, H. Takuda: Int. J. Plasticity **27**, 1072 (2011).
6. T. Mayama, M. Noda, R. Chiba, M. Kuroda: Int. J. Plasticity **27**, 1916 (2011).
7. G. Proust, C. N. Tomé, A. Jain, S. R. Agnew: Int. J. Plasticity **25**, 861 (2009).
8. O. Muránsky, D. G. Carr, P. Šittner, E. C. Oliver: Int. J. Plasticity **25**, 1107 (2009).
9. M. Li, X. Y. Lou, J. H. Kim, R. H. Wagoner: Int. J. Plasticity **26**, 820 (2010).
10. Q. Ma, H. E. Kadiri, A. L. Oppedal, J. C. Baird, B. Li: Int. J. Plasticity **29**, 60 (2012).
11. A. L. Oppedal, H. E. Kadiri, C. N. Tomé, G. C. Kaschner, S. C. Vogel, J. C. Baird, , M. F. Horstemeyer: Int. J. Plasticity **30-31**, 41 (2012).
12. K. Piao, J. K. Lee, J. H. Kim, H. Y. Kim, K. Chung, F. Barlat, R. H. Wagoner: Int. J. Plasticity **38**, 27 (2012).
13. J. Lévesque, K. Inal, K. W. Neale, R. K. Mishra: Int. J. Plasticity **26**, 65 (2010).
14. A. S. Khan, C. S. Meredith: Int. J. Plasticity **26**, 189 (2010).

15. A. S. Khan, A. Pandey, T. G. Herold, R. K. Mishra: *Int. J. Plasticity* **27**, 688 (2011).
16. A. Fernández, M. T. P. Prado, Y. Wei, A. Jérusalem: *Int. J. Plasticity* **27**, 1739 (2011).
17. S. Seipp, M. F. X. Wagner, K. Hockauf, I. Schneider, L. W. Meyer, M. Hockauf: *Int. J. Plasticity* **35**, 155 (2012).
18. M. G. Lee, R. H. Wagoner, J. K. Lee, K. Chung, H. Y. Kim: *Int. J. Plasticity* **24**, 545 (2008).
19. M. G. Lee, S. J. Kim, R. H. Wagoner, K. Chung, H. Y. Kim: *Int. J. Plasticity* **25**, 70 (2009).
20. B. Shi, J. Mosler: *Int. J. Plasticity* **44**, 1 (2013).
21. L. Bian, F. Taheri, Y. Lu: *Int. J. Plasticity* **24**, 302 (2008).
22. R. H. Wagoner, H. Lim, M. G. Lee: *Int. J. Plasticity* **45**, 3 (2013).
23. B. L. Mordike, T. Ebert: *Mater. Sci. Eng. A* **302**, 37 (2001).
24. M. Vogel, O. Kraft, E. Arzt: *Scripta Mater.* **48**, 985 (2003).
25. J. Grobner, R. S. Fetzner: *J. Alloy. Compd.* **320**, 296 (2001).
26. Y. Wang, S. Guan, X. Zeng, W. Ding: *Mater. Sci. Eng. A* **416**, 109 (2006).
27. W. Blum, P. Zhang, B. Watzinger, B. V. Grossmann, H. G. Haldenwanger: *Mater. Sci. Eng. A* **319-321**, 735 (2001).

28. M. Bamberger: J. Mater. Sci. **41**, 2821 (2006).
29. D. H. Kang, S. S. Park, Y. S. Oh, N. J. Kim: Mater. Sci. Eng. A **449-451**, 318 (2007).
30. C. L. Mendis, C. J. Bettles, M. A. Gibson, C. R. Hutchinson: Mater. Sci. Eng. A **435-436**, 163(2006)
31. T. T. Sasaki, J. D. Ju, K. Hono, K. S. Shin: Scripta Mater. **61**, 80 (2009).
32. S. Wei, Y. Chen, Y. Tang, H. Liub, S. Xiao, G. Niu, X. Zhang, Y. Zhao: Mater. Sci. Eng. A **492**, 20 (2008).
33. V. R. K. Prasad, K. P. Rao, N. Hort, K. U. Kainer: Mater. Lett. **62**, 4207 (2008).
34. T. T. Sasaki, K. Yamamoto, T. Honma, S. Kamado, K. Hono: Scripta Mater. **59**, 1111 (2008).
35. S. S. Park, B. S. You: Scripta Mater. **65**, 202 (2011).
36. H. J. Tsai, C. G. Kuo, C. G. Chao, T. F. Liu: Adv. Sci. Lett. **8**, 599 (2012).
37. H. J. Tsai, C. G. Kuo, C. G. Chao, T. F. Liu: Metall. Mater. Trans. **54A**, 1423 (2013).
38. A. A. N. Hashemi, J. B. Clark: Bulletin of Alloy Phase Diagrams **5**, 466 (1984).
39. H. Liu, Y. Chena, Y. Tang, S. Wei, G. Niu: J. Alloy Compd. **440**, 122 (2007).
40. V. M. Segal: Patent of the USSR, **No. 575892** (1977).



41. S. S. Park, Y. J. Kim, W. L. Cheng, Y. M. Kim, B. S. You :Phil. Mag. Lett. **91**, 35 (2011).
42. M. Zhang, W. Z. Zhang, G. Z. Zhu: Scripta Mater. **59**, 866 (2008).
43. A. Kozlov, M. Ohno, R. Arroyave , Z.K. Liu, R. S. Fetzter: Intermetallics **16**, 299 (2008).
44. A. Kozlov, M. Ohno, T. A. Leil, N. Hort, K. U. Kainer, R. S. Fetzter: Intermetallics **16**, 316 (2008).
45. E. Doernberg, A. Kozlov, R. S. Fetzter: J. Phase Equilib. Diff. **28**, 6 (2007).
46. T. A. leil, N. Hort, W. Dietzel, C. Blawert, Y. Huang, K. U. Kainer, K. P. Rao: Trans. Nonferrous Met. Soc. China **19**, 40 (2009).
47. M. Bamberger: J. Mater. Sci. **41**, 2821(2006).
48. F. Pan, M. Yanga: Mater. Sci. Eng. A **528**, 4973 (2011).
49. M. A. Kearns, P. S. Cooper: Mater. Sci. Technol. **13**, 650 (1997).
50. D. Apelian, G. K. Sigworth, K. R. Whaler: AFS Trans. **92**, 297 (1984).
51. Radhakrishna, Seshan, M. R. Seshadri: Trans. Indian Inst. Met. **34**, 169 (1981).
52. A. M. Samuel, F. H. Samuel: J. Mater. Sci. **30**, 1698 (1995).
53. W. R. O. Rio, P. R. Goulart, G. A. Santos, C. M. Neto, A. Garcia: Metall. Mater. Trans. **37A**, 1221 (2006).

54. B. H. Kim, J. J. Jeon, K. C. Park, B. G. Park, Y. H. Park, I. M. Park: Archives Mater. Sci. Eng. **30**, 93 (2008).
55. M. Zhang, W. Z. Zhang, G. Z. Zhu, Y. Kun: Trans. Nonferrous Met. Soc. China **7**, 428 (2007).
56. H. Liu, Y. Chen, Y. Tang, S. Wei, G. Niu: Mater. Sci. Eng. A **464**, 124 (2007).
57. S. Wei, Y. Chen, Y. Tang, X. Zhang, M. Liu, S. Xiao, Y. Zhao: Mater. Sci. Eng. A **508**, 59 (2009).
58. T. Sakai, J. J. Jonas: Acta Metall. **32**, 189 (1984).
59. L. Nakashima, Z. Horita, M. Nemoto, T. G. Langdon :Acta Mater. Mater. **46**, 1589 (1998).
60. V. M. Segal, K. T. Hartwig, R. E. Goforth: Mater. Sci. Eng. A **224**, 107 (1997).
61. V. M. Segal,: Mater. Sci. Eng. A **197**, 157 (1995).
62. V. M. Segal,: Mater. Sci. Eng. A **386**, 269 (2004).
63. Y. Iwahashi, J. Wang, Z. Horita, M. Nemoto, T. G. Langdon: Scripta Mater. **35**, 143 (1996).
64. K. Nakashima, Z. Horita, M. Nemoto, T. G. Langdon: Acta Mater. **46**, 1589 (1998).
65. Y. Iwahashi, Z. Horita, M. Nemoto, T. G. Langdon: Acta Mater. **45**, 4733 (1997).

66. S. D. Terhune, D. L. Swisher, K. O. Ishi, Z. Horita, T. G. Langdon, T. R. M. Nelley: *Metall. Mater. Trans.* **33A**, 2173 (2002).
67. C. P. Chang, P. L. Sun, P. W. Kao: *Acta Mater.* **48**, 3377 (2000).
68. Y. Iwahashi, Z. Horita, M. Nemoto, T. G. Langdon: *Acta Mater.* **46**, 3317 (1998).
69. P. L. Sun, P. W. Kao, C. P. Chang: *Metall. Mater. Trans.* **35A**, 1359 (2004).
70. V. M. Segal: *Mater. Sci. Eng. A* **271**, 322 (1999).
71. S. L. Semiatin, V. M. Segal, R. E. Goforth, N. D. Frey, D. P. Delo: *Metall. Mater. Trans.* **30A**, 1425 (1999).
72. A. Yamashita, D. Yamaguchi, Z. Horita, T. G. Langdon: *Mater. Sci. Eng. A* **287**, 100 (2001).
73. Y. C. Chen, Y. Y. Huang, C. P. Chang, P. W. Kao: *Acta Mater.* **51**, 2005 (2003).
74. Y. Y. Wang, P. L. Sun, P. W. Kao, C. P. Chang: *Scripta Mater.* **50**, 613 (2004).
75. W. J. Kim, H. T. Jeong: *Metall. Mater. Trans.* **46A**, 251 (2005).
76. K. Matsubara, Y. Miyihara, Z. Horita, T. G. Langdon: *Acta Mater.* **51**, 3073 (2003).
77. K. Matsubara, Y. Miyihara, Z. Horita, T. G. Langdon: *Metall. Mater. Trans.* **35A**, 1735 (2004).
78. T. Chandrashekar, M. K. Muralidhara, K. T. Kashyap, P. R. Rao: *Int. J. Adv. Manuf. Technol.* **40**, 234 (2009).

79. T. L. Liu: Mater. Sci. Eng. A **22**, 146 (2004).
80. A. Galiyev, R. Kaibyshev, G. Gottstein: Acta Mater. **49**,1199 (2001).
81. R. B. Figueiredo, T. G. Langdon: Mater. Sci. Eng A **501**, 105 (2009).
82. H. K. Lin, J. C. Huang, T. G. Langdon: Mater. Sci. Eng. A **402**, 250 (2005).
83. Y. Lu, Q. Wang, X. Zeng, W. Ding, C. Zhai, Y. Zhu: Mater. Sci. Eng. A **278**, 66 (2000).
84. B. Somjeet, S. D. Satyaveer, S. Satyam: Microstructure and texture in steels **part VI**, 465 (2009).
84. Y. H. Wei, Q. D. Wang, Y. P. Zhu, H. T. Zhou, W. J. Ding, Y. Chino, M. Mabuchi: Mater. Sci. Eng. A **360**, 107 (2003).
85. Y. Miyahara, K. Matsubara, Z. Horita, T. G. Langdon: Metall. Mater. Trans. **36A**, 1705 (2005).
86. H. K. Lin, J. C. Huang, T.G. Langdon: Mater. Sci. Eng. A **402**, 250 (2005).
- 87.X. Wu, Y. Liu: Scripta Mater. **46**, 269 (2002).
88. O. D. Sherby, J. Wadsworth: Prog. Mater. Sci. **33**,169 (1989).
89. H. Somekawa, K. Hirai, H. Watanabe, Y. Takigawa, K. Higashi: Mater. Sci. Eng. A **407**,53 (2005).
90. H.J. Frost, M.F. Ashby: *Deformation–Mechanism Maps*, Pergamon Press (1982).
91. A. H. Feng, Z. Y. Ma: Scripta Mater. **56**, 297 (2007).

PUBLICATION LIST

SCI Journal Papers:

1. **Hao-Jan Tsai**, Chin-Guo Kuo, Chuen-Guang Chao, Tzeng-Feng Liu, " Investigation of the Microstructures and Mechanical Properties of the Mg-(2, 5, 8) wt.% Sn Alloys at high temperatures after an ECAE Process ", Advanced Science Letters, 2012, 8, 599-604. (IF = 1.3)
2. **Hao-Jan Tsai**, Chin-Guo Kuo, Chuen-Guang Chao, Tzeng-Feng Liu, " Effect of ECAE on Microstructures and Mechanical Properties of Solution Heat Treated Mg-5(mass%) Sn Alloy", Materials Transactions, 2013, 54, 1423-1428. (IF = 0.6)
3. **Hao-Jan Tsai**, Chin-Guo Kuo, Chuen-Guang Chao, Tzeng-Feng Liu, " Investigating Microstructures and High Temperature Superplasticity Behavior of Mg-5(mass%) Sn Alloy by using Equal Channel Angular Extrusion ", Journal of Marine Science and Technology, Accept 2013 December. (IF = 0.5)
4. Che-Yi Lin, **Hao-Jan Tsai**, Chuen-Guang Chao, Tzeng-Feng Liu, "Effects of ECAE Process on Microstructures and High Temperature Properties of ZA85 Magnesium Alloy", Journal of Alloys and Compounds, 2012, 530, 48-55. (IF = 2.4)

Conference papers:

1. **Hao-Jan Tsai**, Chin-Guo Kuo, Chuen-Guang Chao, Tzeng-Feng Liu, "Superplastic Behavior of Mg-5(wt.%)Sn Alloy after Equal Channel Angular Extrusion", Proceeding of Word Congress on Engineering and Technology (CET), No. 24282, Shanghai, China (2011).
2. **Hao-Jan Tsai**, Chin-Guo Kuo, Chuen-Guang Chao, Tzeng-Feng Liu, " Investigation of the Microstructures and Mechanical Properties of the Mg-(2, 5, 8) wt. % Sn Alloys at high temperatures after an ECAE Process", Proceedings of the First International Conference on Engineering and Technology Innovation (ICETI), No. A1095, Kenting, Taiwan (2011).
3. Che-Yi Lin, **Hao-Jan Tsai**, Chuen-Guang Chao, Tzeng-Feng Liu, "Effects of ECAE process on microstructures and high temperature properties of za85 magnesium alloy", China Materials Science Annual Meeting, No. 075, Taipei, Taiwan (2008).
4. Siang-Yi Su, Da-Wei Yang, **Hao-Jan Tsai**, Jung-Hsuan Chen, "Manufacturing thermoelectric ternary alloy nano-wires using vacuum casting method", China Materials Science Annual Meeting, No. 0305, Hualien, Taiwan (2009).

中文期刊：

- 1、蔡浩然、郭金國、朝春光、劉增豐：Mg-(2, 5, 8) wt.% Sn 合金經 ECAE 熱機處理後其顯微組織與高溫機械性質研究，金屬熱處理期刊，(2012) **115**，32-40。
- 2、郭金國、蔡浩然、劉岳函、曾冠捷、朱晟華：AZ91D 鎂合金時效處理之顯微組織分析，鑄造科技，(2013) **281**，16-20。
- 3、郭金國、蔡浩然、高福辰、余修毅：AZ61 鎂合金時效處理之研究，鑄造工程學刊，(2009) **35**，37-42。

